# Detailed Characterization of Jets in Heavy Ion Collisions Using Jet Fragmentation Functions

by

Frank Teng Ma

Submitted to the Department of Physics
in partial fulfillment of the requirements for the degree of

Doctor of Philosophy

at the

MASSACHUSETTS INSTITUTE OF TECHNOLOGY

June 2013





Author .....
Department of Physics
May 18, 2013

Certified by .....
Boleslaw Wyslouch
Professor of Physics
Thesis Supervisor

Accepted by .....
John Belcher
Associate Department Head

# Detailed Characterization of Jets in Heavy Ion Collisions Using Jet Fragmentation Functions

by

Frank Teng Ma

Submitted to the Department of Physics
on May 18, 2013, in partial fulfillment of the
requirements for the degree of
Doctor of Philosophy

## Abstract

In this thesis the jet fragmentation function of inclusive jets with transverse momentum $p_{\mathrm{T}} > 100$ GeV/c in PbPb collisions is measured for reconstructed charged particles with $p_{\mathrm{T}} > 1$ GeV/c within the jet cone. A data sample of PbPb collisions collected in 2011 at a center-of-mass energy of $\sqrt{s_{NN}} = 2.76$ TeV corresponding to an integrated luminosity of 150 $\mu\mathrm{b}^{-1}$ is used. The results for PbPb collisions as a function of collision centrality are compared to reference distributions based on pp data collected at the same collision energy. A centrality-dependent modification of the fragmentation function is revealed. For the most central collisions a significant enhancement is observed in the PbPb/pp fragmentation function ratio for the charged particles with $p_{\mathrm{T}}$ less than 3 GeV/c.

Thesis Supervisor: Boleslaw Wyslouch
Title: Professor of Physics

# Acknowledgments

Seven years have passed since I first began as a graduate student in the summer of 2006. I am grateful Lord Jesus, for sustaining me from being consumed in so many times over these years when my faith was faltering. Thank you for teaching me what true faith is really about, this was your good plan all along. And this thesis is evidence for God's great love for sinners like me, his heart for redeeming them from the pit, showing them their invaluable worth in his eyes, and his unwillingness to give up on those who are undeserving of his love. Solely by his grace that he has brought me thus far. He has humbled me, carrying me so much farther than what I could have ever possibly imagined. And so this thesis is to you, for you, and it was by you, Lord Jesus, who was with me wherever I had been — it has always been, and always will be.

Thank you Wit, Gunther, Bolek, George, Christof. You have been my teachers and advisors. It was a privilege. You have shown me what it means to become a mature scientist — the insistence on facts and not personal opinions; that attention to details matters; time is of the essence; focus on the important things; when to give up; and finally, when not to give up.

Thank you Bolek, you have been a great mentor. I am glad you accepted to be my mentor seven years ago.

Yetkin, Yenjie, Andre, Yongsun, guys, we made a good team. We saw the best of times and we saw the worst of times. It was not always easy, but I am glad we went through it together. It was seriously from you guys that I learned the skills in being a graduate student.

Wei, Ed, Siarhei, Burak, you not only taught me physics but also encouraged me when I was down. Those encouragements were invaluable. Ed, Wei, you were really cool postdocs, thank you for all your help.

Dragos, Doga, Mukund, Alex, Alekey, it had been fun, we should hang out again.

Anna, you kept the group together, thank you for being such a great and caring administrator.

Colleagues at CMS heavy ion, you have been not only my colleagues but also friends. I am glad to have been a part of this community. Krisztian, thanks for the Plato.

Naoto, best friend at MIT.

Mom, dad, I love you. It had been a great blessing to see you changing and growing in faith these past seven years. I am amazed of the good work God has been doing in you, and I am so glad.

Apollo, Victoria, Ken, Christina, Jacky, Linpeng, Simon, Hannah, David, Maureen, and all my family in Christ at CBCG, you gave me a home in Geneva. You have been a part of this thesis, and I am thankful to God for you. I miss you.

Jacky, Linpeng, my saving prayer partners. Bio, thanks for all the dinners.

Ken, Christina, Guojin, Zhenzhen, LinNa, LvMing, Jiajia, Chenxi, Guoguo, Yaru, and all at Timonthy Fellowship, I thank God that he brought me to this fellowship right when I went to Geneva. I've grown a lot in this fellowship, and got better in Chinese. It had been a blessing to study the Bible with you and to watch you change.

Jacky, Dan, Jessie, Andrew, all, we were the coolest fellowship at CERN. I will bring chocolates next time.

Dave, Janet, Guorui, Caleb, Guanting, May, Rutendo, Bo, you have been awesome housies, father, mother, brothers, sisters. You have been my biggest blessing in Boston.

John, Yukari, Shanshan, Forrest, Revanth, Matthew, Clare, Ben, all, my best small group ever!

Stuart, Hsuan, Pat, and all my family at PSIF, thank you for all the support, encouragements, faith and love ... PSIF love.

Sonny, I'm glad we both made it.

# Contents

# Chapter 1

# Introduction

What is our world made of and what govern these constituents? These questions represent mankind's long and sustained desire to understand the world we live in. Modern physical science has since then come quite far in answering those questions. We now know that remarkably our world is composed of a handful of elementary particles, namely quarks and leptons, governed by four fundamental forces of nature, namely, gravity, electromagnetism, the weak, and the strong interaction.

Amongst the four fundamental forces of nature, the most powerful, yet in many aspects least understood, is the interaction that governs nuclear matter, the strong interaction.

## 1.1 Quantum Chromodynamics

The theory that describes the strong interaction is now known as Quantum Chromodynamics (QCD). QCD has gluons as spin 1 gauge bosons that mediate the force between quarks. It is modeled based on the simpler theory, Quantum Electrodynamics (QED), which describes electromagnetism.

QCD explains two important properties of the strong interaction (Sec. 2.1). At high energies, the interaction becomes weak, and quarks and gluons interact weakly (Asymptotic Freedom); at low energy the interaction becomes strong and leads to the confinement of color.

### 1.1.1 Quark Gluon Plasma

Because of Asymptotic Freedom, QCD expects that at high temperatures, for which the typical thermal energies of quarks and gluons are large and thus the interactions become weak, ordinary matter made of protons and neutrons undergoes a phase transition to a plasma of quarks and gluons, the quark-gluon plasma (QGP, Sec. 2.3.1).

## 1.2 High Energy Heavy Ion Collisions

QGP can be created under either high temperature or high density. As a result we expect QGP to be created in the early Universe, at the center of compact stars and in the initial stage of colliding heavy nuclei at high energies. The last possibility can be experimentally controlled and studied in heavy ion accelerators. High-energy collisions of heavy ions provide an invaluable tool to study puzzles of quark confinement and symmetry breaking in QCD.

## 1.3 Jet Quenching

Due to the complexity of the multi-body collision system, finding clean experimental signatures poses a challenge. In 1982, shortly before the start of Tevatron, Bjorken first conjectured that high transverse momentum partons produced by hard scatterings in heavy ion collisions can lose energy as they travel through the hot and dense medium created in these interactions [1]. Since then, a variety of experimental observations provided support for this effect, including the suppression of high-$p_{\mathrm{T}}$ particles (as first seen at RHIC [2, 3, 4, 5] and later at the LHC, eg [6, 7]). In addition, the first data at LHC revealed a new phenomenon providing more direct evidence of this energy loss using the difference in momentum between pairs of jets [8, 9] and also jets paired with photons [10]. Unbalanced di-jets and photon-jet pairs were found to be much more prevalent in the most central PbPb collisions[9, 10] compared to expectations in the absence of a strongly interacting medium. In further analysis of di-jet events, the fractional momentum difference was found to be independent of the

momentum of the higher-energy (leading) jet [11]. The projection of the momenta of tracks onto the jet direction demonstrated that the "lost" momentum resides in low-momentum particles emitted at large angles with respect to the jet [9].

### 1.3.1 Jet Fragmentation Function as a QGP Observable

These observations raised a key question related to the parton energy loss mechanism; do partons first lose energy in the nuclear medium and subsequently fragment as they would in vacuum or does the energy loss modify the fragmentation process itself. These experimental observations inspired theoretical models that aim to gain new insights into QCD by explaining the observed suppression of high-$p_{\mathrm{T}}$ particles in heavy-ion collisions using the assumptions of modified parton fragmentation in the presence of the strongly interacting medium [12, 13, 14]. For these reasons, direct measurements of jet fragmentation properties in heavy ion collisions are both interesting and important in the quest to understand QCD through medium induced parton energy loss.

Studies of the detailed properties of jet structure also have important practical consequences for other jet analyses and their connection to the partons that produce the jets. The longitudinal and transverse fragmentation properties of jets connect the perturbatively calculable production of high-$p_{\mathrm{T}}$ quarks and gluons with the hadronized final state particles. The study of jet production via final state particles relies on hadronization models to determine e.g. the non-perturbative hadronization corrections of the production cross section, and also the experimental jet energy scale. The study of fragmentation functions provides an important experimental check on the validity of the assumed jet fragmentation. These additional details of the jet properties can also be used to directly connect jet observables to measurements of high-$p_{\mathrm{T}}$ particle production.

## 1.4 Goal of this Thesis

The goal of this analysis is to measure the partitioning of the jet energy into particles (the fragmentation function) in heavy-ion collisions using fully reconstructed jets. As a first approach to addressing this issue, the higher-momentum ($p_{\mathrm{T}} > 4$ GeV/c) component of the fragmentation function was found to be qualitatively similar to that for jets in pp collisions, for which the medium is absent [15]. Taking advantage of data from the higher integrated luminosity heavy-ion run in 2011 ($150\,\mu\mathrm{b}^{-1}$ of PbPb collisions at a center-of-mass energy of 2.76 TeV), the analysis described in this paper expands on the previous result by measuring the fragmentation functions for tracks down to $p_{\mathrm{T}} > 1$ GeV/c and in more differential centrality bins.

In the thesis analysis, a clear centrality dependent modification of the inclusive jet fragmentation function in PbPb collisions is revealed. In the most central 0–10% collisions and for the lowest charged particle momenta studied, an excess is observed in the the PbPb/pp fragmentation function ratio, rising to $1.6 \pm 0.2(\mathrm{stat.}) \pm 0.3(\mathrm{syst.})$. The mid to high $p_{\mathrm{T}}$ part of the fragmentation function of these jets in the central PbPb events are found to be consistent with fragmentation function of quark jets in vacuum.

# Chapter 2

# Theory

## 2.1 QCD and Asymptotic Freedom

Modern physics describes the fundamental forces of nature in terms of fields, e.g. the electromagnetic field and the gravitational field. The spectacular success of Quantum Electrodynamics (QED) lead physicists to understand the importance of relativistic quantum field theory. In particular, it is realized that the fundamental forces seem to all belong to a special class of field theories, called "gauge" theories. The present belief is that QCD is also dictated by local gauge invariance. Starting from the mounting evidence for quarks and the color charge, the emergent quantum field theory description of the strong interaction is now know as Quantum Chromodynamics (QCD).

Because QCD drew its inspiration from QED, there are many similar aspects of QCD to QED. In QED the electromagnetic force acts on objects with electric charge. In QCD the strong interaction is made possible due to the presence of color charge. In QED, charged objects interact via the quanta of the electromagnetic field, the photons. Similarly, in QCD, colored objects interaction via quanta of the color field, the gluons. There is however one crucial difference between QCD and QED. In QCD, gluons themselves carry color charge, and thus can interact directly with other gluons. In QED, photons do not carry charge and so photons cannot directly interact with other photons. The direct coupling of gluons has dramatic implications, leading to

an important property of QCD called Asymptotic Freedom.

One reason that the existence of quarks and color took decades to be accepted is the fact that free quarks are never observed in nature. In all of our observations, quarks are only found confined within bound states called hadrons, such as protons and neutrons. What is the mechanism responsible for quark confinement? QCD has a possible explanation. The key idea is that the strength of the interaction between particles depends on the momentum or distance scale of the interaction. It is a general feature of quantum field theory that the interaction field can excite virtual particle-antiparticle pairs even in vacuum. The apparent violation of energy conservation is allowed by the energy-time version of the Heisenberg uncertainty principle. These particle-antiparticle pairs carry different charges, for example, electric charge if subject to QED or color charge if subject to QCD. As a result, the presence of such vacuum excitations of the field modifies the original field. In QED this implies that even in vacuum, a electric charge such as an electron is perpetually surrounded by a cloud of $e^+e^-$ pairs which are polarized by the electric field of the electron. The polarization is in such a fashion that the positive charges are closer to the electron. As a result, the negative charge of the electron is effectively reduced, as shown in Fig. 2-1. Consequently, the effective charge of the electron depends on the distance scale of the probe. By moving the test charge closer to the electron we penetrate through the electron-positron cloud that screens the electron's charge. Thus in QED, the vacuum acts as polarizable medium, and the measured effective charge of the electron grows larger the closer the interaction distance. In QCD the color field of the quark similarly excites the vacuum surround it, creating virtual quark-antiquark pairs.

However, in QCD because gluons themselves are color charged, gluons can couple to other gluons. Thus the color field can excite pairs of gluons as well as pairs of quarks as shown in Fig. 2-1. Now, since gluons carry color, the gluon cloud around the quark can carry away its color charge. This causes the color charge to be no longer localized at a definite place in space but diffusely spread out due to gluon emission and absorption. Consequently at a closer distance to the quark, it becomes

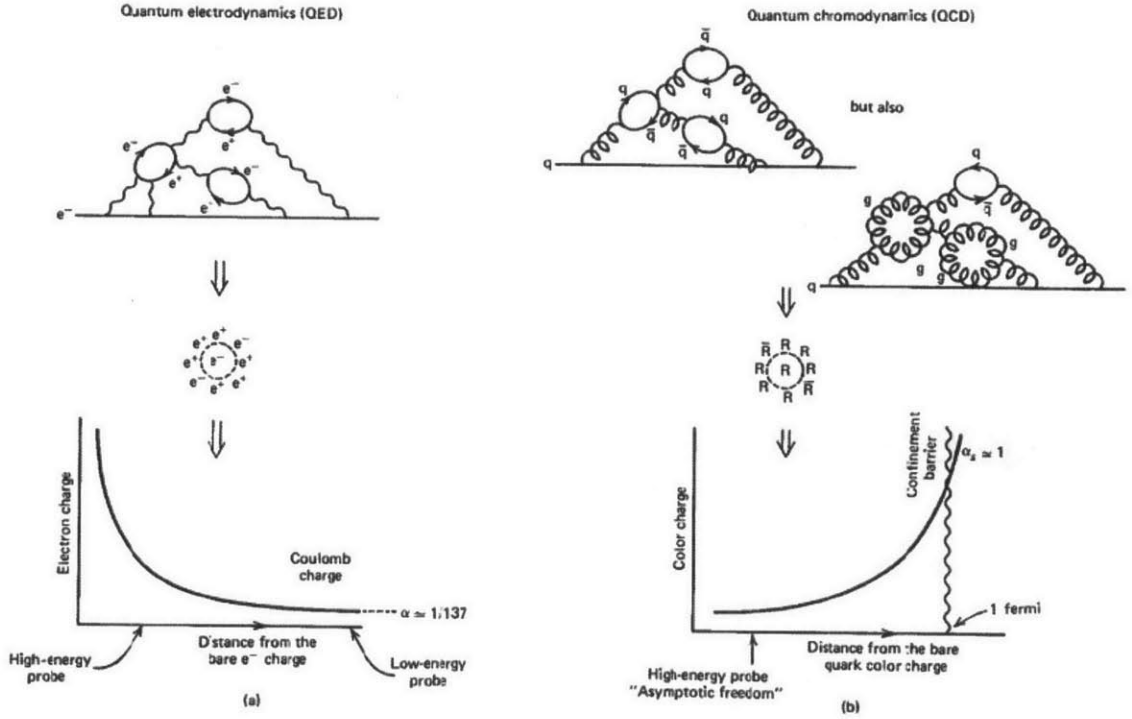


Figure 2-1: Screening of the electric charge (a) and color charge (b) in quantum field theory. (from Halzen Martin 1.3)

less likely to find the color charge of the quark. The color screening effect due to the polarized vacuum and the color diffusion effect due to the radiated gluons have opposite effects. If one computes all possible configurations, it turns out that the color diffusion effect is larger. (This is related to the fact that there are 8 gluons but only 3 quarks.) Therefore overall, the effective color charge of the quark appears smaller at shorter distance (bottom right, Fig. 2-1). This effect is called Asymptotic Freedom. The strong interaction is weak at small distances within the proton, yet it becomes strong if the quarks try to separate. A free quark is simply not a stable solution of the QCD Lagrangian. This provides the qualitative explanation of color confinement. Yet the skeptic may still question, are we only arguing for color confinement as an excuse for our failure to observe free quarks in nature? The answer is no. The picture provided by quarks and asymptotic freedom makes unique and dramatic prediction in the experimental signature of jets.

## 2.2 QCD Jet Physics

### 2.2.1 What is a Jet?

One extremely clean way to study quarks is by colliding electrons and positrons at high energies. Even though the electron and position do not carry color, they can produce hadrons via annihilation. Before data became available with high energy $e^+e^-$ colliders, some physicists believed that the hadronic final states in $e^+e^-$ annihilations would emerge as a uniform, isotropic distribution. In the QCD picture, the $e^+e^-$ annihilate to produce a virtual photon at rest which in turn decays into a $q\bar{q}$ pair, as shown in Fig. 2-2.

As the $q\bar{q}$ pair is produced at rest, the quark and antiquark should emerge in opposite directions to conserve momentum. When the pair separates by a distance of order 1 fm, $\alpha_s$ becomes truly strong, and the quarks can be thought to as violently decelerated. The decelerated quarks undergo final state radiation to form hadrons. The radiated hadrons (mostly pions) hit the detector as collimated sprays of particles.

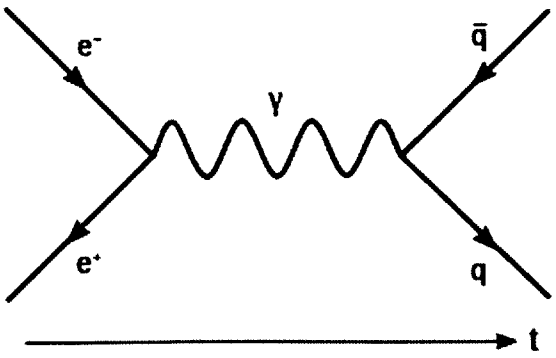


Figure 2-2: Electron positron annilation creating a quark-antiquark pair. (Image from Wikipedia)

These collimated sprays of particles are called jets. This is exactly what we see in particle accelerator experiments, starting from SPEAR at SLAC in 1972, and subsequently at DORIS at DESY in 1973, PEP at SLAC in 1980, TRISTAN at KEK in 1987, LEP at CERN in 1986, Tevatron at Fermilab in 1986, and finally LHC at CERN in 2009. Fig. 2-3 show such a di-jet final state event in pp collisions at CMS.

The fact that collimated sprays of particles hit the detector as jets and not the originally produced quarks themselves is a result of the asymptotic freedom property of QCD. The hadrons in a jet have small transverse momentum relative to their parent quark, and their longitudinal momenta roughly add up to the longitudinal momentum of the parent quark. The precise definition of a jet depends on the clustering algorithm used in the experiment. Yet jets are the real world manifestations of quarks and gluons. They are "as close as we can get experimentally to 'seeing' quarks and gluons".

### 2.2.2 Introduction to Jet Fragmentation Function

The bremsstrahlung products of a quark are detected by the experiment as a jet and never the original quark. This can be qualitatively understood through asymptotic freedom. When a quark and antiquark separate, their color interaction becomes stronger. This can seen as a result of the fact that the gluons carry color charge.

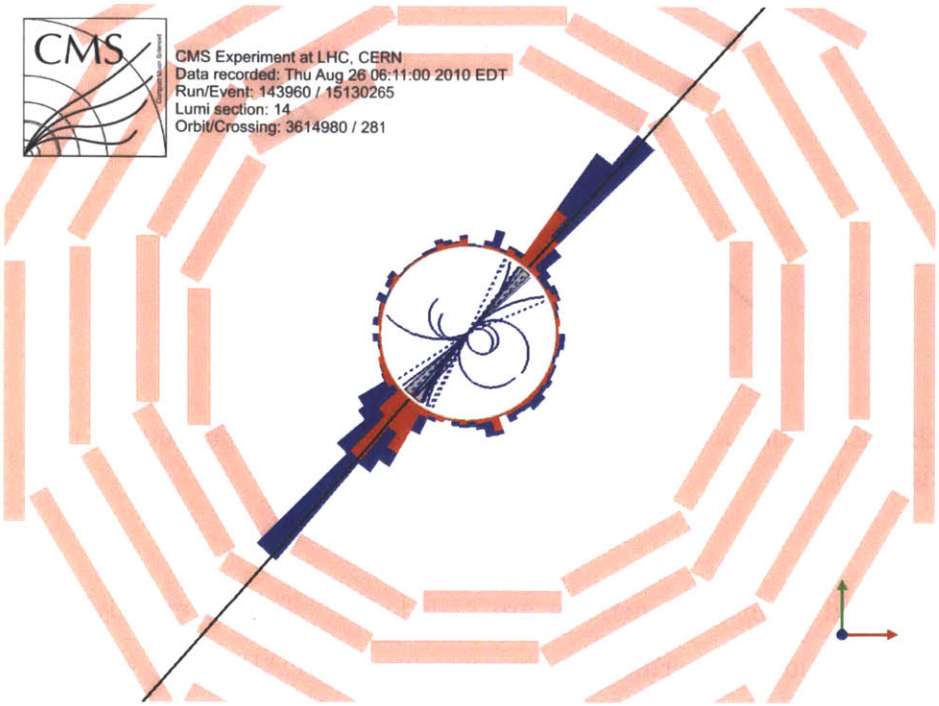


Figure 2-3: Di-Jet event within the CMS detector, as seen in looking down the beam-pipe in the transverse plane.

The gluon self interaction squeezes field lines of the gluon field into a tube-like region (Fig. 2-4a). If the color tube has constant energy density then this results in a linearly growing potential between the quarks. This behavior can be contrasted with QED, where the photons carry no electric charge. Thus the field lines of the photon field spread out according to $1/r^2$ because nothing keeps the field lines together (Fig. 2-4b).

This confining behavior of QCD is believed to be responsible for the total confinement of quarks to colorless hadrons. It is also why the original parton fragments into hadron jets. The $q\bar{q}$ pair separates due to the initial large amount of center-of-mass energy. As they separate the color lines are stretched with increasing potential energy, as shown in Fig. 2-5. The potential energy grows until it is sufficient to create another $q\bar{q}$ pair. The new $q\bar{q}$ pair serves as end points to the color lines and the original color line is broken up into two shorter color lines with lower potential energy at the cost of the extra $q\bar{q}$ pair mass. The outgoing quark and antiquark continue to separate with decreased momentum, further stretching the color lines. In this fashion

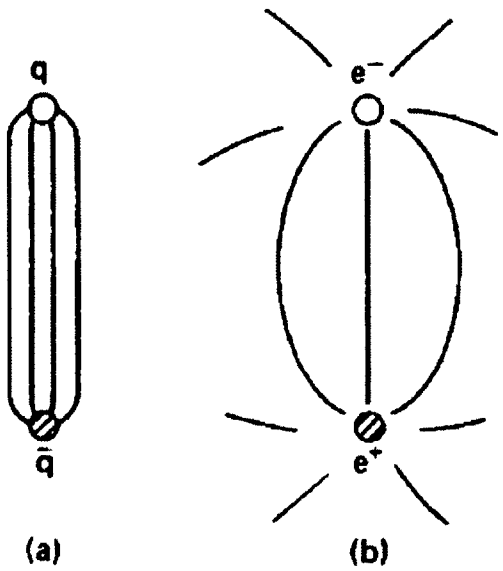


Figure 2-4: Color field lines are squeezed together in a $q\bar{q}$ pair, while they spread out for a $e^+e^-$ pair. (from Halzen Martin 1.5)

more $q\bar{q}$ pairs are created until all the initial kinetic energies of the outgoing quark and antiquark are used up. The end result is two jets of color neutral particles with total momentum roughly equal to the momentum of the original parent quarks. This describes the process of jet fragmentation.

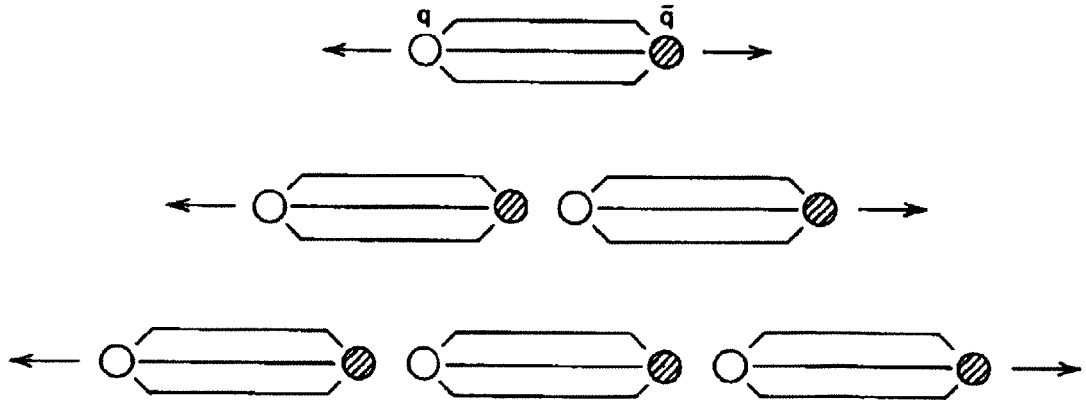


Figure 2-5: Jet fragmentation as a result of $q\bar{q}$ separating. (from Halzen Martin 1.5)

The differential cross section of the fragmentation of quarks and gluons in $e^+e^-$ collisions can be written as

$$\frac{d\sigma(e^-e^+ \to hX)}{dz} = \sum_q \sigma(e^-e^+ \to q\bar{q})[D_q^h(z) + D_{\bar{q}}^h(z)], \tag{2.1}$$

where $z$ is the fraction of the parent quark energy carried by the fragmented particle. That is,

$$z \equiv \frac{E_h}{E_q}. \tag{2.2}$$

The differential cross section 2.1 describes two sequential events: first the production of quarks from the initial hard scattering, followed by their fragmentation into hadrons. Since the quarks must fragment into hadrons with probability of unity, the $D$ functions thus represent the probability that the hadron $h$ fragments from the parent parton with fraction $z$ of its energy. $D(z)$ called the fragmentation function. The summation in Eq. 2.1 is carried over all quark flavors in recognition of the fact that the detector in unaware of the quantum numbers of the parent quark. This is schematically shown in Fig. 2-6.

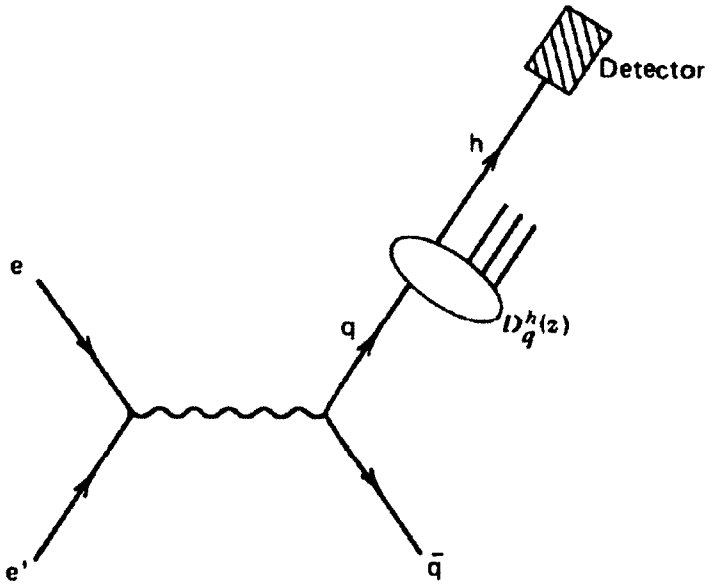


Figure 2-6: Fragmentation product $h$ is observed in the detector carrying fraction $z$ of the quark's energy. (from Halzen Martin 11.2)

Since the fragmentation functions are properties of partons, we expect they are

universal functions no matter how the partons are produced. Thus fragmentation functions serve as an important and useful tool to study physics phenomenon related to quarks and gluons. In practice the exact definition of $z$ can change from experiment to experiment. In this thesis we have adopted the CDF convention to define $z$ as the momentum fraction of the particle along the jet axis out of the total jet momentum.

### 2.2.3 Fragmentation Function in Vacuum

Before turning our attention to expectations of medium modification, let us first build some intuitions of fragmentation expectations in vacuum based on conventional perturbative QCD (pQCD).

#### Interaction Time Scales

We have been describing the jet fragmentation process as a parton, after being knocked out of a hadron (or the vacuum) from a hard process, being quickly decelerated due to the strong color field as the parton separates from the hadron (or antiquark). One basic question to ask in physics is, what time scales are involved in this process? At the very least, one time scale involved is when the color field becomes truly strong at the typical size of a hadron in the quark's reference frame. Since these are relativistic processes there is also a time dilation factor, $t = \gamma t'$. Thus in the rest frame we expect,

$$t^{hadr} \sim \gamma t'^{hadr} = \frac{E}{m} r, \tag{2.3}$$

where $r$ measures typical value of inter-quark distance in a hadron ( 1fm) and $m$ the quark's constituent mass in a hadron. For a light quark ($q = u, d, s$) $m_{constituent} \sim$ few hundred MeV. Thus for a quark with energy E $\sim$ 100 GeV, the hadronization time is $t^{hadr} \sim \frac{O(100\text{GeV})}{O(100\text{MeV})} \times 1\text{fm/c} \sim O(10^3)\text{fm/c}$. Compare this to the time scale of the hard interaction, $t^{hard} \sim 1/E = 1/100\text{GeV} \sim O(10^{-3})\text{fm/c}$, we see that $t^{hadr} >> t^{hard}$ by orders of magnitude. Thus the quark behaves approximately as a true color particle radiating gluons perturbatively without any knowledge of its future confinement.

### Perturbative QCD

Having justified the applicability of pQCD to parton fragmentation process, we may start to build our intuition on the QCD evolution of jet by taking advantage of the power of perturbation theory. In the perturbative regime where the strong interaction coupling constant, $\alpha_s$ is small, QCD is similar to QED (except for the extra possibility of gluon self couplings). One may write the matrix elements for various processes using the Feynman diagram technique. One basic QCD process involved in parton evolution is the parton splitting process. For example a quark radiating a gluon as shown in Fig. 2-7.

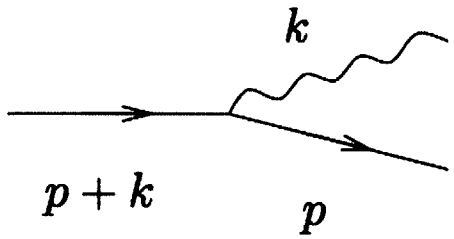


Figure 2-7: Kinematics of gluon emission. (from Dokshitzer 1.1.2)

Applying the Feynman rules almost identically as QED, one will arrive at the following differential spectrum

$$dw^{q\to qg} = \frac{\alpha_s(k_\perp^2)}{4\pi} 2C_F[1 + (1 - \frac{k}{E})^2]\frac{dk}{k}\frac{dk_\perp^2}{k_\perp^2}, \tag{2.4}$$

where $k_\mu$ is the 4-momentum of the gluon, $k$ is the energy of the gluon, $E$ is the energy of the parent quark, and $k_\perp$ is the transverse momentum of the gluon with respect to the parent quark.

Equ. 2.4 describes the probability of a quark with energy E splitting into a gluon with energy k and a quark with energy $E-k$. Because there is no gluon self coupling in the Feynman diagram Fig. 2-7, the differential spectrum is identical to the same process in QED ($e^- \to e^-\gamma$), except for the color factor $C_F$ and the coupling constant $\alpha_s = g_s^2/4\pi \to \alpha$. From this basic diagram we can see the origins of the infrared

divergence in the $1/k$ term, and the collinear divergence in the $1/k_\perp^2$ term. These divergences are of course not physical in nature, and in fact when we sum up other (loop) diagrams of the same order, we will see that the divergences will be canceled.

### QCD Color Coherence

We are now at a position to understand how the initial parent quark evolves into the multiplicity distribution of the final state hadrons. The parton radiates gluons as it decelerates, and the radiated gluons will in turn radiate either directly or by producing $q\bar{q}$ pairs that radiate. This results in a "shower" like cascade of parton emission, similar to the process of a QED shower (Fig.2-8):

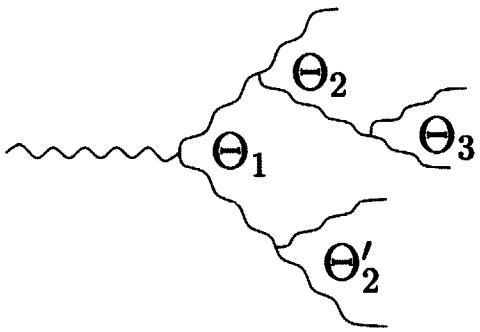


Figure 2-8: Illustration of QCD cascade and angular ordering (from Dokshitzer 4.1)

It is interesting to intuitively predict the expected features of the QCD cascade energy spectrum without explicit computation. First we expect the fragmentation spectrum to decrease at high momentum because the matrix element amplitude decreases as $\sim 1/q^2$ due to the propagator from the parton. This is the decreasing $p_{\mathrm{T}}$ spectrum that we typically see at a hadron collider. At the low momentum limit, one may think that the probability for soft emission increases at lower and lower $p_{\mathrm{T}}$ until some QCD cut-off at hadronization scale of a few hundred MeV. However, a remarkable prediction of pQCD is that soft emission from the radiating parton is suppressed. This is due to the effect of quantum coherence that is a common feature of all gauge theories. The physics explanation is that gluons of long wavelength cannot resolve

the branched parton from the parent parton. Thus the soft gluon (either at low $p_T$ or wide angle) is radiated coherently by the total color current of the jet, which is conserved when the partons split and is independent of the internal structure of the jet. The soft radiation then essentially depends on the total color charge of the initial parton and not on the multiplying cascade. As a result of this coherent radiation, it is not the softest partons but those with intermediate energies that multiply most effectively in QCD cascades. These expectations of pQCD are shown pictorially in Fig. 2-9.

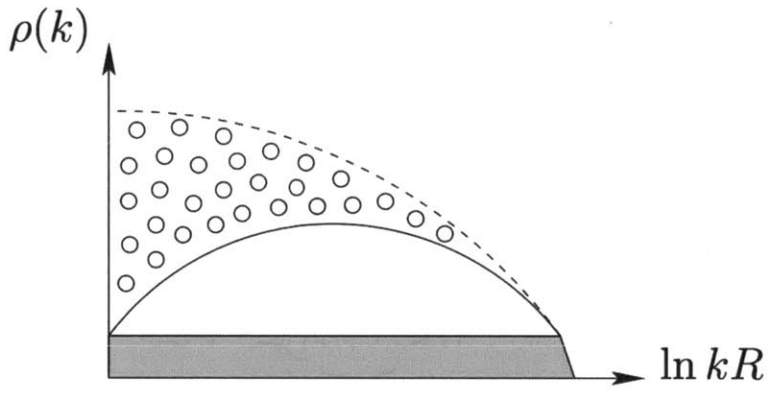


Figure 2-9: The effect of color coherence on particle energy spectrum $\rho(k) = dn/d\ln(k)$. R is a constant representing size of jet. Dotted area corresponds to the contribution which is removed when turning from the incoherent model (dashed) to the coherent one (solid). Shaded area shows the simple plateau without taking account of bremsstrahlung. (from Dokshitzer 4.3)

Fig. 2-9 shows the multiplicity of the jet fragmentation products as a function of the natural log of their energies, $k$. In the absence of perturbative gluon radiation, the resulting hadron spectrum would simply be independent of $ln(k)$ (due to the $1/k$ term in $dw^{q\to qg}/dk$, Eq. 2.4). This is shown in the shaded region of Fig. 2-9. This would be the result of the simple parton model as illustrated in Fig. 2-5 which has no gluon radiation. With the additional gluon cascade initiated multiplicity (dashed line in Fig. 2-9), the resulting particle multiplicity is much increased. This increase is partially due to the fact that gluons radiate gluons roughly a factor of 2 ($C_A/C_F$=9/4) more intensely than quarks radiate gluons. But the main cause of the

increase in multiplicity is the fact that particle production is now exponentiated due to the QCD shower which was not there in the simple quark model. Finally taking into account the coherent radiation (solid line in Fig. 2-9), the soft part of the energy spectrum is depleted, giving rise to a characteristic hump-back shape of the energy spectrum of jet fragmentation functions.

### Confirmation of pQCD Jet Fragmentation

The hump-back expectation of the pQCD jet fragmentation was one of the early successful tests of pQCD. These expectations are well confirmed in both $e^+e^-$ collisions (Fig. 2-10) and hadron colliders (Fig. 2-11).

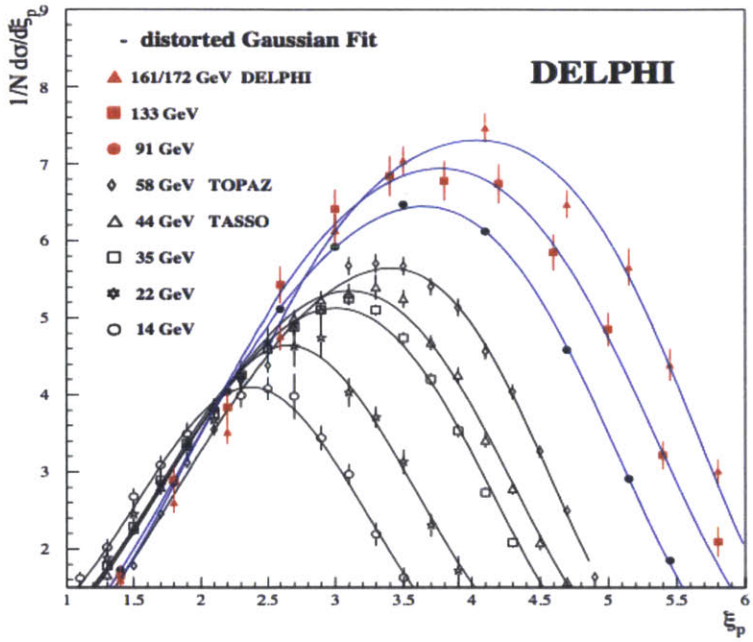


Figure 2-10: Jet fragmentation function in $e^+e^-$ annihilation. [16] Note that here, $\xi = \ln(1/z)$, $z = \frac{p_h}{E_j et}$

In Fig. 2-10 and Fig. 2-11, the data is compared to pQCD predictions, the Modified Leading Log Approximation (MLLA). It is an approximate solution to pQCD where the higher-order terms that are enhanced are taken into account. Enhanced higher-order terms are associated with kinematic configurations for which the relevant QCD matrix elements are large. In particular, recall from Eq. 2.4 that there are

enhancements when a soft gluon is emitted, or when a parton splits into two almost collinear partons. The leading contributions to these soft and collinear configurations can be identified and summed to all orders, thus improving the convergence of the perturbation series. The spectrum is approximately a gaussian in the logarithmic variable $\xi = \ln(1/x)$. Thus MLLA spectrum is sometimes parametrized as a distorted gaussian fit (as shown in Fig. 2-10), which uses the first four moments (mean, width, skewness, and kurtosis) of the MLLA distribution around its maximum.

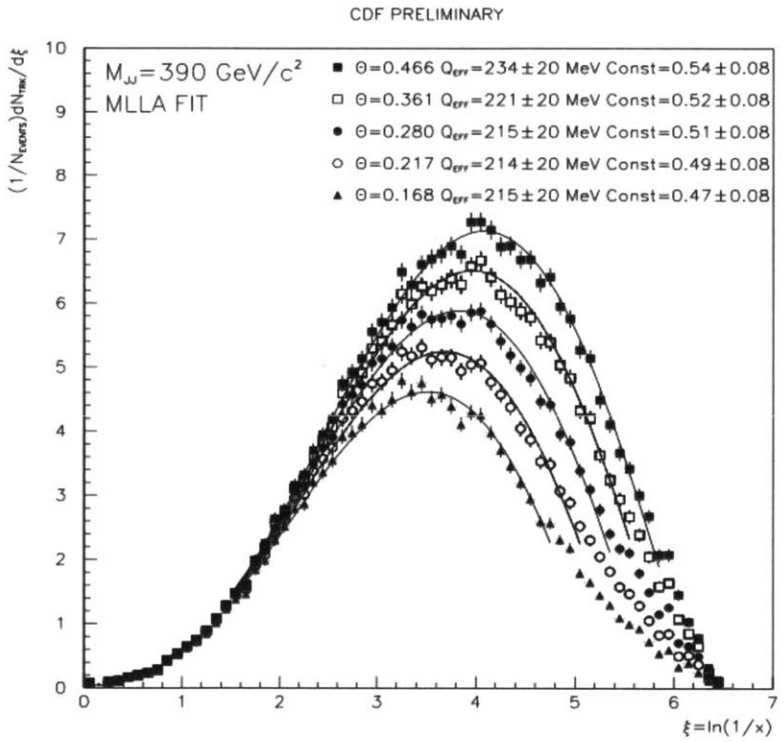


Figure 2-11: Jet fragmentation function of high $p_{\mathrm{T}}$ jets in $p\bar{p}$ collisions. [16] Note that here, $\xi = \ln(1/z)$, $z = \frac{p_h}{E_{jet}}$

## 2.3 Jet Fragmentation in QGP

### 2.3.1 What is QGP?

Due to asymptotic freedom in QCD (Sec. 2.1), we have said that quarks exist in ordinary matter always in bound state of color-neutral ("white") composite objects called hadrons. The situation changes as we increase the temperature of the quark system. As the temperature increases, the typical thermal energies of the quarks and gluons inside hadrons begin to increase as they come to equilibrium with the high temperature environment. This results in a weaker color coupling between the quarks and gluons due to asymptotic freedom. At the same time, more gluons and $q\bar{q}$ pairs are thermally excited from the vacuum. These thermally excited quarks and gluons create plasma screening of the the color fields. As a result, at high enough temperature, the hadronic system is expected to undergo a phase transition to behave as a de-confined, weakly interacting gas of quarks and gluons, the quark gluon plasma (QGP).

The typical QCD confinement scale, $\Lambda_{QCD}$ is $\sim$ 200 MeV, so for a phase transition to QGP we naively expect a temperature at least larger than O(200 MeV). Note that this temperature is an order of $\sim 10^5$ hotter than the center of the sun (which is around $1.5 \times 10^7 K = 1.3$ keV). Monte Carlo numerical solutions of QCD using a discretized lattice of space-time (Wilson's lattice gauge theory) also predicts a phase transition around this temperature (Fig. 2-12).

Fig. 2-12 shows the lattice calculation results of $\epsilon/T^4$ as a function of temperature. The ratio essentially reflects the number of degrees of freedom of the system, since in equilibrium all accessible states are occupied. At a critical temperature $T_c$ of around 160 MeV (the inflection point, see the zoomed-in inset of Fig. 2-12), the number of degrees of freedom changes very rapidly, possibly discontinuously. This indicates a phase transition from the hadron gas to the QGP. The arrow in the figure shows the Stefan-Boltzmann limit, $\epsilon_{SP}/T^4$, corresponding to the non-interacting gas of spin 1 bosons. The deviation from the arrow indicates that the gluons are interacting above $T_c$.

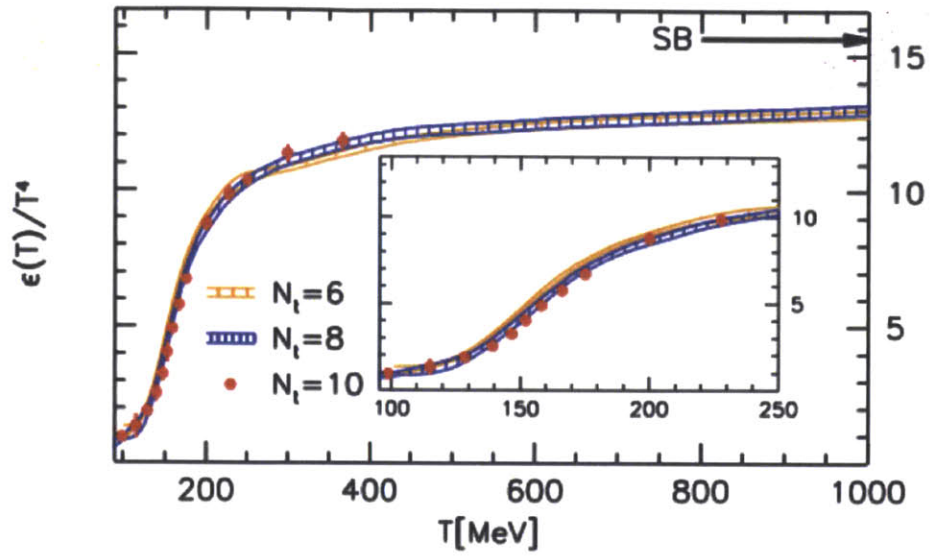


Figure 2-12: The energy density, $\epsilon$(T), normalized by $T^4$ as a function of the temperature, on with increasing finder lattice spacing, $N_t = 6$, 8 and 10 lattices. The Stefan-Boltzmann limit $\epsilon_{SP}(T) = 3p_{SB}(T) \approx 15.6T^4$ is indicated by an arrow. For the highest temperature T = 1000 MeV the pressure is almost 20% below this limit. Result from S. Borsanyi et al (2010) [17].

Based on Fig. 2-12, we can read off the corresponding energy density at the critical temperature to be $\epsilon \sim 5 \cdot (0.16 \text{ GeV})^4 \cdot (5.07 \text{ GeV/fm})^3 \approx 0.4 \text{ GeV/fm}^3$. Where can we find this kind of temperature environment in nature? The energy density inside a proton is $\epsilon_{proton} \sim 0.94 \text{ GeV}/\frac{4}{3}\pi(0.88 \text{ fm})^3 \sim 0.3 \text{ GeV/fm}^3$, has comparable energy density. But to achieve a stable QGP we need a system with temperature well above $T_C$. In addition the system needs to have macroscopic degrees of freedom to be described by thermal equilibrium. Two known places of such high energy density and macroscopic degrees of freedom exist in nature. One is in the early universe, about $10^{-5}$ seconds after the Big Bang. The second is in the system produced by heavy ion collisions at relativistic energies with particle accelerators. From Phobos whitepaper (2005) [5], we see that the energy density of the equilibrated system in heavy ion collisions at RHIC is conservatively estimated to have a lower bound of 3 GeV/fm$^3$. Thus we expect to gain experimental access to QGP at RHIC ($\sqrt{s_{NN}} = 200$ GeV) and much more at the O(10) higher energy heavy ion collisions at LHC ($\sqrt{s_{NN}} =$

2.76 TeV).

Data from RHIC indeed observed an equilibrated QCD medium created in these heavy nuclei collisions [2, 3, 4, 5]. However, unlike the naive expectation of a plasma of weakly interacting quarks and gluons, a strongly coupled system is found. Furthermore it was found that this system can be described by equations of ideal hydrodynamics, pointing to a very small viscosity of the system [18]. This was one of the most remarkable discoveries concerning QCD systems, and makes it all the more interesting to study the properties of this QCD medium in heavy nuclei collisions.

### 2.3.2 Studying QGP with Jets

How can we systematically study the properties of the QCD matter formed at RHIC and LHC? Various signatures have been proposed over the past decades. In this thesis, we will focus on the idea, first pointed out by Bjorken ([1]) in 1982, of using high momentum partons, i.e. jets as experimental signature and probe of QGP.

To explain how high momentum partons can be used as probes of the QGP, we will first continue the analogy between QED and QCD. (This is in fact an appropriate analogy since at high momentum, QCD becomes perturbative and thus similar to QED.) When a charged particle, such as an electron, passes through matter, it loses its kinetic energy due to electromagnetic interactions with the charged constituents of the material (electrons and nuclei). There are two main sources of energy loss: it can exchange energy with other charged particles by colliding inelastically with them, or it can exchange energy with the electromagnetic fields by radiation (Jackson, 1999). At low energies, collisional energy loss is dominant, while at high energies radiative energy loss becomes dominant. This is in fact the Bethe-Bloch formula (Fig. 2-13).

Similarly, let us consider now a color charged parton, created by a high momentum scattering in the initial stage of a nucleus-nucleus collision. As the parton traverses the quark and gluon medium formed by the nucleus-nucleus collision, it loses its kinetic energy due to strong interactions with the quark and gluons. Similar to the QED case, the parton can either exchange energy with other quarks and gluons by colliding inelastically with them, or the parton can change energy with the color fields

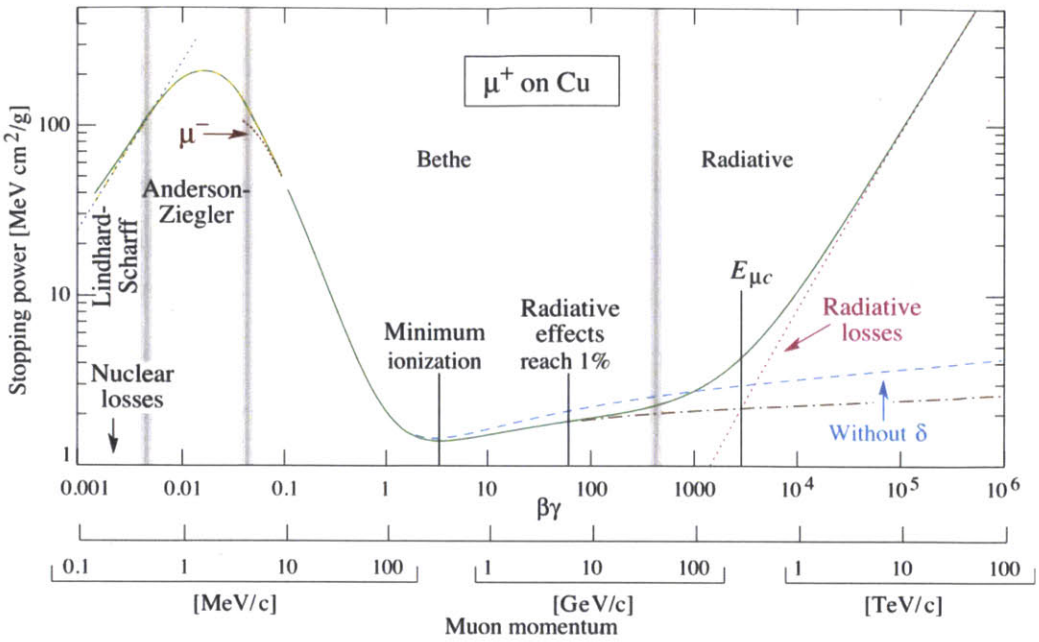


Figure 2-13: $\langle -dE/dx \rangle$ for positve muons in copper as a function of $\beta\gamma = p/Mc$. From http://pdg.lbl.gov/.

by radiation. These sources of energy loss are shown schematically in Fig. 2-14.

(a) In 1982 Bjorken [1] pointed out that high momentum partons created in the initial stage of the heavy ion collision can be affected by the collisions with soft particle (E $\sim$ T) in QGP. This can be calculated from the scattering processes shown in Fig. 2-14 (a).

(b) Later Gyulassy, Plumer, Thoma, and Wang [19, 20, 21] considered the radiative energy loss the parton undergoes in QGP, shown in Fig. 2-14 (b).

### Medium Modification of Jet Fragmentation Function

Interactions between the colored parton probe and the strong color field of the medium modify the way the parton evolves as described in Sec. 2.2.3. The QGP (Sec. 2.3.1) has a size and lifetime on the scale of O(10fm). Recall from Sec. 2.2.3 that the time scale of a hard scattering with $q \sim 100$ GeV is $t^{hard} \sim O(10^{-3}) fm/c$. Therefore, a large fraction if not all of the fragmentation process of hard partons should be

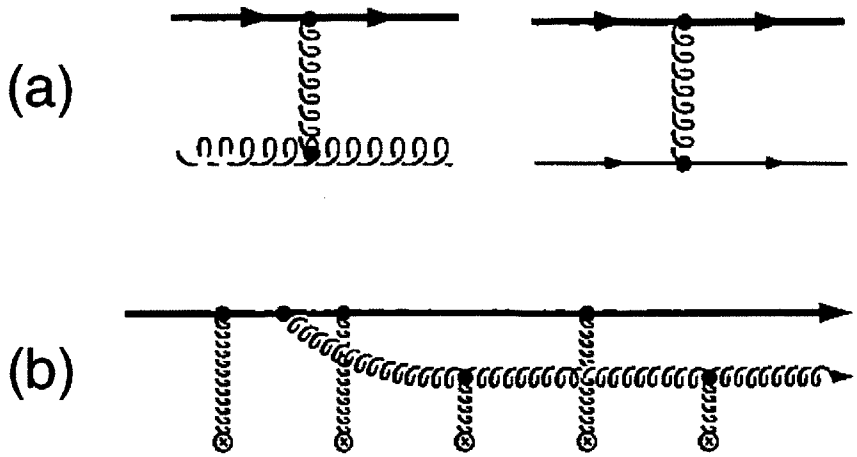


Figure 2-14: Processes of parton energy loss in QGP. Thick solid lines denote the high momentum quark traversing the QGP. (a) Typical diagrams for collisional energy exchange in QGP. The quark interacts with the thermal quarks and gluons in the plasma. (b) Radiative energy loss in QGP. The quark interacts with the randomly distributed color sources $\otimes$ and emits gluon radiations. Emitted gluons interact further with the color sources. (Taken from Yagi, Hatsuda, Miake 14.2)

affected by the presence of the dense QCD medium. This mechanism is believed to be responsible for the spectacular "jet quenching" phenomenon reported by the RHIC experiments, where a factor of 5 suppression of single inclusive hadron spectra at high $p_{\mathrm{T}}$ is observed in Au-Au collisions with respect to (properly scaled) p-p collisions. Thus a direct experiment measurement of the jet fragmentation function in heavy ion collisions with high momentum jets is interesting and important. To summarize, by measuring how QGP induce modifications to the jet fragmentation function, we may gain a better understanding of the in-medium parton energy loss mechanism, probe properties of the QCD medium, and finally hope to obtain better insights into the nature of the strong interaction.

### 2.3.3 In-Medium Jet Fragmentation Modification Models

To connect the basic ideas of QCD to experimental measurements in high energy heavy ion collisions, computations of concrete predictions of experimental observables are needed. Due to the non-abelian nature of QCD, full solutions of parton evolution in a multi-body system of quarks and gluons is still outside of theoretical reach today. However, the calculation problem can be simplified while still capturing the essential features of QCD by using first-principle inspired models. By making certain simplifying assumptions about the medium and the medium interaction processes, these models allow for direct comparisons of data to theory. A wealth of literature exists that review the topic of jet quenching models, and the few review papers that helped with the writing of this thesis are [22, 23, 24]. This section will present a few concrete and representative examples of models that aim to gain insight into properties of QCD based on predictions of in-medium modifications of jet fragmentation functions.

#### Energy Rescaling Models

The simplest approach to model medium modified jet fragmentation is to assume that the parton QCD evolution is not affected by the medium. The effect of energy loss is simply to rescale the initial parton energy, e.g from $E$ to $E - \epsilon$, after which the parton fragments as if in the vacuum. This is illustrated in Fig. 2-15.

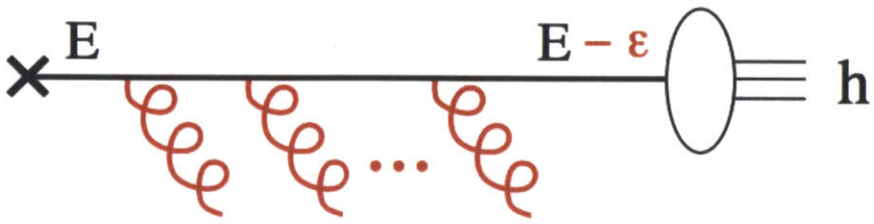


Figure 2-15: Schematic illustration of the energy loss process and the medium-modified jet fragmentation in the energy rescaling model. (taken from [22])

In Fig. 2-15, a parton (black line) from an initial hard scattering (black "x")

traverses through the QCD medium. As it passes through the QCD medium, it loses energy by radiation due to inelastic scatterings with the medium. The radiations are represented as the red gluons. Assuming hadronization does not occur inside the medium, the parton escapes the medium at the end of its path. It loses a total amount of energy, $\epsilon$. The escaped parton with energy $E - \epsilon$ then fragments into hadrons as represented by lines and the legend "h" in the figure.

Because fragmentation functions are steeply falling functions of $x$, even a small shift in the parton energy can introduce a significant suppression of hadron yield at high $p_{\mathrm{T}}$. This model and variants of it had been used successfully and widely to explain the high $p_{\mathrm{T}}$ hadron suppression observed at RHIC.

### Modified Splitting Function Models

A more realistic model than the rescaling model takes account of the re-scattering of the full parton shower in the medium. One class of models describes the energy loss process as a medium modified parton splitting function of the pQCD parton evolution described in Sec 2.2.3. For example in the approach of Borghini and Wiedemann [25], the gluon radiation induced by the medium modifies the divergent part of the the QCD splitting functions,

$$P_{qq}^{med}(z) = C_F[\frac{2(1+f_{med})}{(1-z)_+} - (1+z)], \tag{2.5}$$

where $f_{med}$ is a parameter controlling the amount of the medium induced gluon radiation. This approach is motivated by the more infrared singular behavior of the induced gluon spectrum compared to that in the vacuum. The medium-modified MLLA equation can then be solved similarly as done in vacuum. This yields the modified fragmentation function. This result taken from [25] is shown in Fig. 2-16.

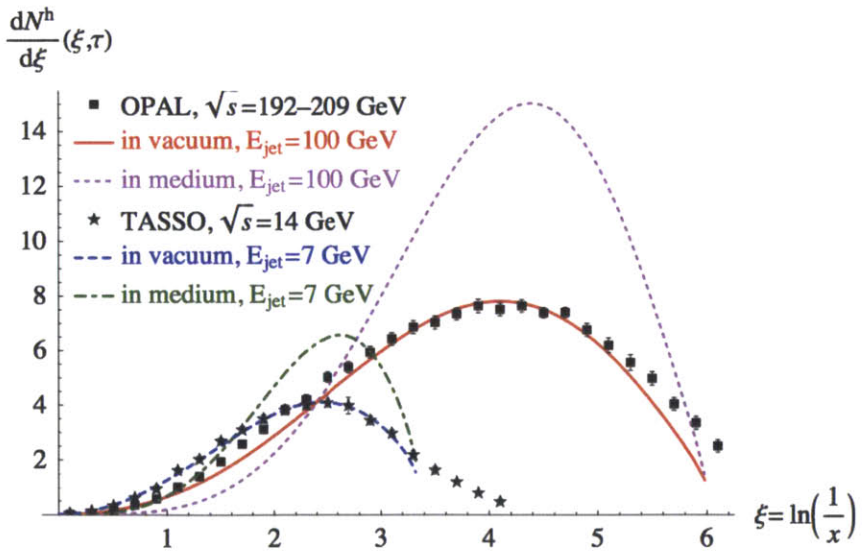


Figure 2-16: The single inclusive hadron distribution as a function of $\xi = ln[E_{jet}/p]$. Dashed and dash-dotted curves labeled "in-medium" are calculated with a medium-modification $f_{med} = 0.8$ of the LO splitting functions. (from [25])

### Modified Parton Shower MC

Another powerful way to understand parton evolution is by treating the parton branching as an iterative probabilistic process. This is the idea behind MC based parton shower techniques as employed in PYTHIA. The MC based parton shower allow for energy-momentum conservation throughout the full evolution, as opposed to analytic approximations in MLLA. Several parton shower MC that model the parton evolution in QCD medium have been developed. One example, called Q-PYTHIA, which stands for quenched PYTHIA, was developed from a modification of the PYTHIA shower algorithm (PYSHOW). The effect of parton energy loss is to increase the virtuality of the re-scattering partons by an amount $\Delta Q^2$. The increased virtuality effectively makes the partons radiate more. The amount of $\Delta Q^2$ directly depends on transport coefficient of the medium $\hat{q} = \hat{q}(x,t)$ given by a 3D hydrodynamic evolution. The resulting fragmentation function modification from Q-PYTHIA is shown in Fig. 2-17.

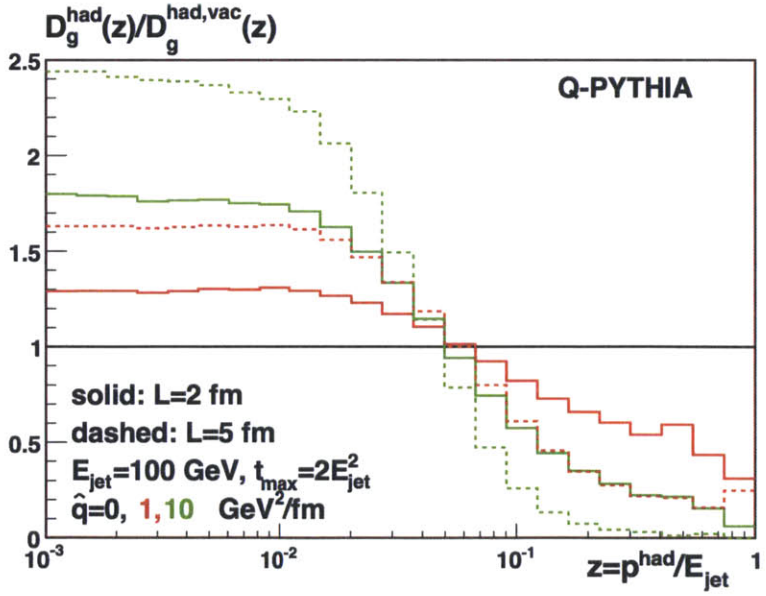


Figure 2-17: Q-Pythia. Ratio of medium to vacuum fragmentation functions for hadrons, for different gluon energies $E_{jet}$, medium lengths L, transport coefficients $\hat{q}$ and maximum virtualities $t_{max}$, refer to the legends on plot. (from [26])

Another example of MC based in-medium parton shower model is recently de-

veloped by Majumder [27]. In this model the in-medium shower is based on the higher-twist formalism of jet modification. Higher twist contributions involve correlations between quarks and gluons in QCD evolution process. Their result on the modified fragmentation function is shown in Fig. 2-18.

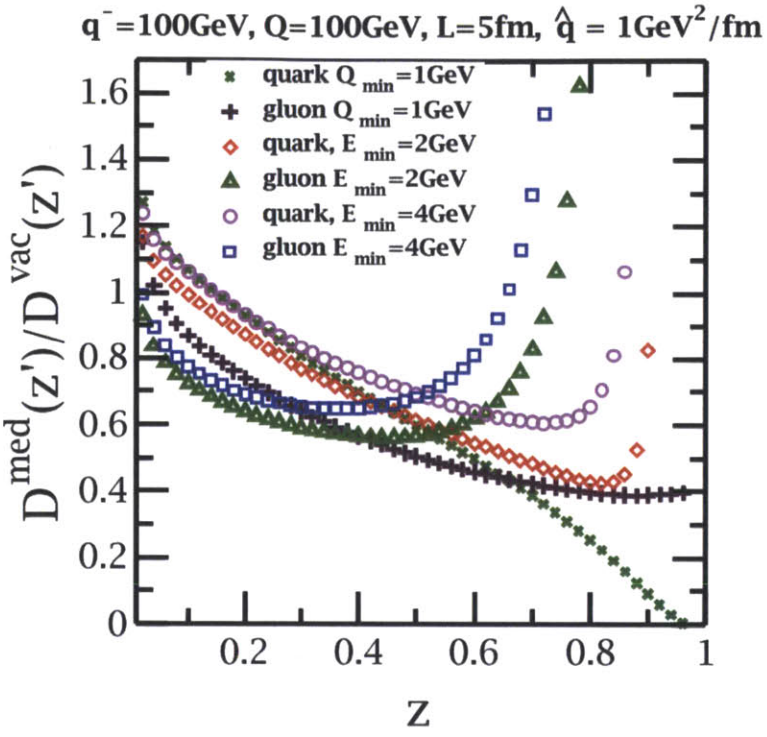


Figure 2-18: Calculations of the ratio of the medium modified fragmentation function to the vacuum fragmentation functions for a quark jet and a gluon jet with an initial energy of 100 GeV, propagating through a medium of length 5 fm, with a $\hat{q} = 1\text{GeV}^2/\text{fm}$. (from [27])

# Chapter 3

# Experimental Setup and Procedures

## 3.1 The CMS Detector

CMS is a particle detector with the goal of harvesting the discovery potentials at the LHC. As a discovery machine, the exact physics signals that CMS will measure are not known a priori. Therefore it is designed to be a general-purpose detector that aims to detect practically all particles emerging from the proton-proton collisions. At the same time it needs to measure the trajectories and momenta of these particles up to high $p_{\mathrm{T}}$ ( TeV scale). For these reasons CMS is also an excellent detector for heavy ion collisions.

To achieve the goal of detecting all particles that emerge from the collisions, CMS was built as a hermetic particle detector. A 3D drawing of the detector is shown in Fig. 3-1 to aid visualization. This figure is drawn to scale based on the Geant4 simulation of CMS.

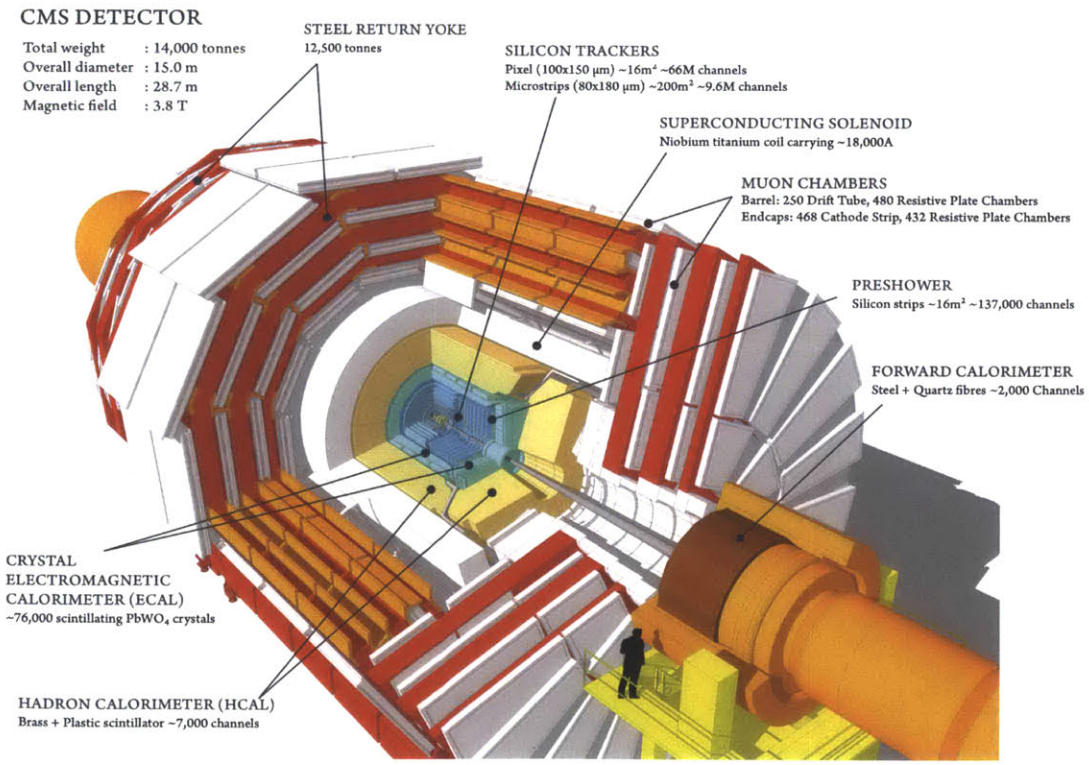


Figure 3-1: 3D view of CMS, drawn to scale. (Courtesy of CERN, CMS)

To measure the kinematic properties of a variety of species of particles from the

collision, CMS is assembled from a combination of individual detectors. These include a tracker, in combination with a strong magnetic field to measure the momentum and trajectories of charged particles; a calorimeter to measure energy of hadrons, electrons and photons; and a muon detector. These individual sub-detectors are positioned in a cylindrical onion-like fashion as shown in Fig. 3-2. The figure also shows the physical dimensions of the different sub-detectors.

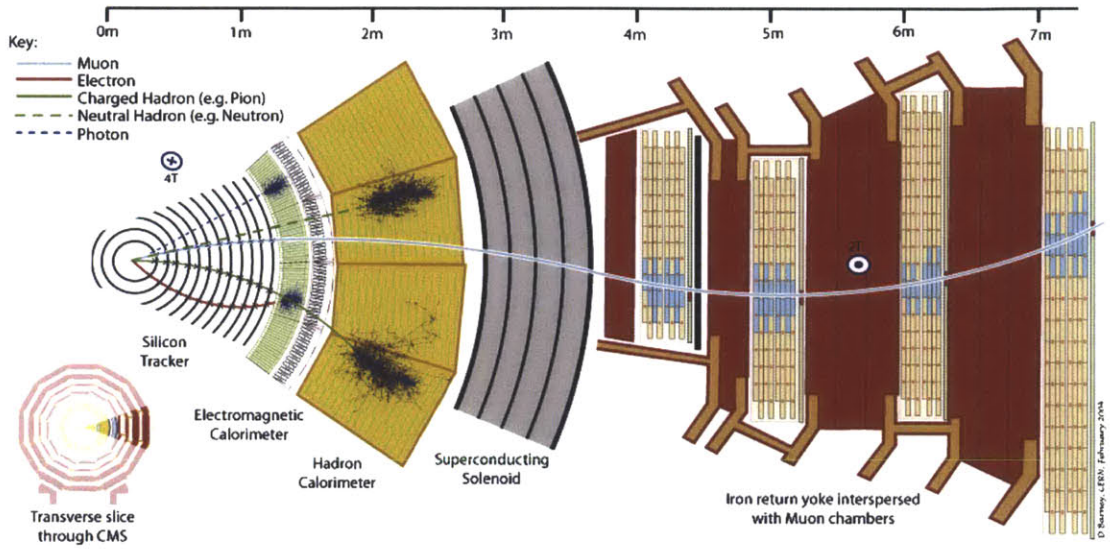


Figure 3-2: A transverse slice through the CMS detector, showing the layered, onion structure of subdetectors. The depicted interactions present detector behavior for different particles. (Courtesy of CERN, CMS)

CMS uses a right-handed coordinate system in which the $z$ axis points in the anticlockwise beam direction, the $x$ axis points towards the center of the LHC ring, and the $y$ axis points up, perpendicular to the plane of the LHC ring. The azimuthal angle $\phi$ is measured in radians with respect to the $x$ axis, and the polar angle $\theta$ is measured with respect to the $z$ axis. A particle with energy $E$ and momentum $\vec{p}$ is characterized by transverse momentum $p_{\mathrm{T}} = |\vec{p}| \sin\theta$, and pseudorapidity $\eta = -\ln[\tan(\theta/2)]$.

In this thesis, the strengths and features of the detectors that are relevant to measuring jet fragmentation functions are highlighted.

### 3.1.1 CMS Tracker

The CMS tracker is the detector closest to the interaction point. It is designed to provide a precise and efficient measurement of charged particles emerging from the LHC collisions. The tracker is cylindrical in shape and surrounds the interaction point. A homogeneous magnetic field of 3.8 T is provided by the CMS solenoid over the entire volume of the tracker.

Requirements of granularity, speed and radiation hardness leads to a tracker design that is entirely silicon based. It consists of a pixel detector for finest granularity close to the interaction point, and a silicon strip tracker at larger radii. A $r - z$ view of the tracker is shown in Fig. 3-3. Each system is completed by endcaps which extends the acceptance of the tracker up to a pseudorapidity of $|\eta| < 2.5$.

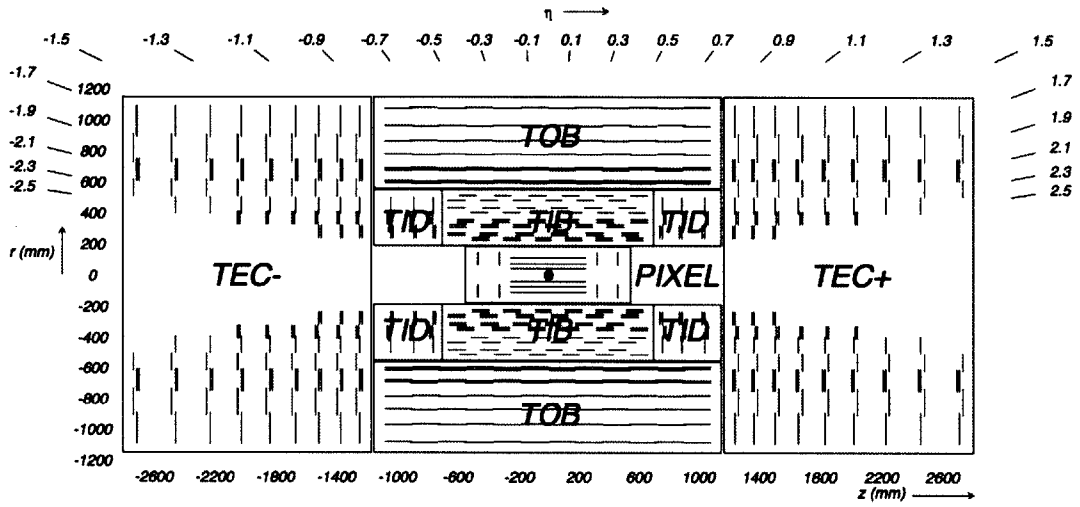


Figure 3-3: $r - z$ view of the CMS tracker. The solid black dot in the middle shows the interaction point.

#### CMS Pixel Detector

The pixel detector is the part of the tracker that is closest to the interaction point. It contributes precise tracking in $r - \phi$ and $z$ and therefore is responsible for a small impact parameter resolution that is important for secondary vertex reconstruction. A single pixel cell has size of $100 \times 150 \mu m^2$. The pixel system covers a pseudorapidity

range of $-2.5 < \eta < 2.5$. It has a total of 66 million pixels. Due to the large number of channels, the pixel system has a zero-suppressed read out scheme with analog pulse height read-out. The zero-suppression allows for a reduced data readout volume by removing channels with no signal. The analog pulse height read-out is used to improve the position resolution due to charge sharing. At the same time it helps to separate signal and noise hits as well as to identify large hit clusters from overlapping tracks.

For the barrel layers of the pixel detector, the drift of the electrons to the collecting pixel implant is perpendicular to the 3.8 T magnetic field of CMS. The resulting Lorentz drift leads to charge spreading of the collected signal charge across more than one pixel. With the analog pulse height being read out a charge interpolation allows to achieve a spatial resolution in the range of 15-20 $\mu$m.

Fig. 3-4 shows the geometry and coverage of the pixel detector. The pixel tracker consists of three 53.3 cm long barrel layers and two end-cap disks on each side of the barrel section. The innermost barrel layer has a radius of 4.4 cm, while for the second and third layers the radii are 7.3 cm and 10.2 cm, respectively.

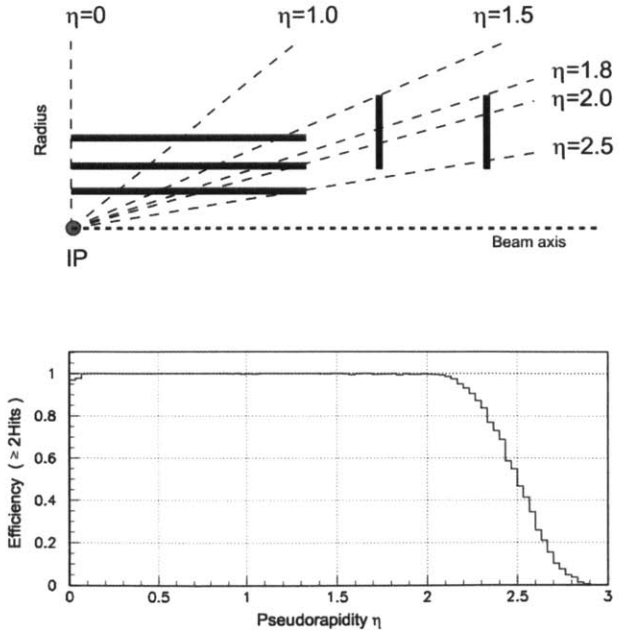


Figure 3-4: Geometrical layout of the pixel detector and hit coverage as a function of pseudorapidity $\eta$.

During the data-taking period addressed by this thesis, 98.4% of the pixel channels were operational. The fraction of noisy pixel channels was less than $10^{-5}$.

### CMS Silicon Strip Tracker

The CMS silicon strip tracker is located radially outside of the pixel detector. The sensor elements in the strip tracker are silicon micro-strip sensors. The tracker is divided into the barrel tracker region and the endcap region.

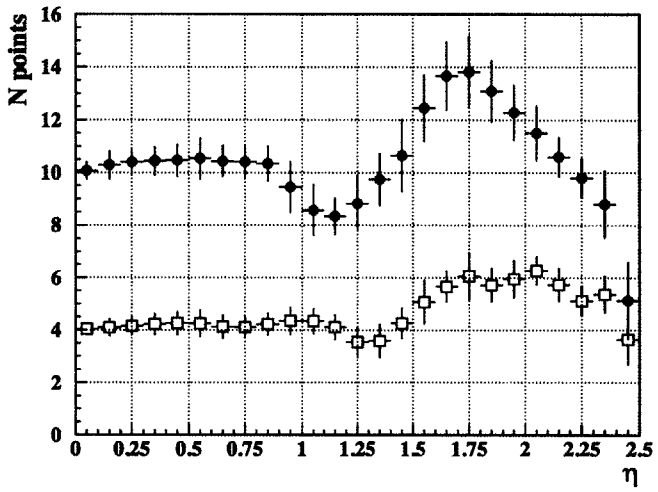


Figure 3-5: Number of measurement points in the strip tracker as a function of pseudorapidity $\eta$. Filled circles show the total number (stereo modules count as one) while open squares show the number of stereo layers.

In the barrel region, the silicon sensors have thickness of 320 $\mu$m and a strip pitch that varies from 80 to 120 $\mu$m. The first 2 layers are made with "stereo" modules in order to provide a measurement in both $r-\phi$ and $r-z$ coordinates. The stereo angle is chosen to be 100 mrad. This leads to a single-point resolution of between 23-34 $\mu$m in the $r-\phi$ direction and 230 $\mu$m in $z$. In the outer layers of the tracker, longer strip lengths and wider pitch distances are used since the particle density is lower.

The signal-to-noise ratio in the silicon strip depends on the sensor thickness. It was measured [28] from first LHC data to be around 20. The tracker was aligned as described in [29] using cosmic ray data prior to the LHC commissioning. The

precision achieved for the positions of the detector modules with respect to particle trajectories is 3-4 $\mu$m in the barrel for the coordinate in the bending plane.

Fig. 3-5 shows the number of detected hits on a track that passes through the silicon strip tracker. This information is useful in separating true tracks from fake tracks because true tracks will preferentially have a total of 17 hits (3 from pixel detector, 10 from silicon strip tracker, and 4 from stereo layers of the silicon strip tracker) if it passes through the entire tracker.

During the data-taking period addressed by this thesis, 97.2% of the silicon strip tracker channels were operational.

**Zero Suppression Read-out** The signals from the silicon sensors are amplified, processed and stored by a custom integrated circuit, the APV25. Upon a positive L1 trigger decision, the analogue signals of all channels are read-out to Front End Driver (FED) boards where the signal is digitized. In pp data taking, the pedestal and common mode noise are calculated and subtracted in the FEDs. The FEDs process data from up to 96 pairs of APV25 chips, before forwarding zero-suppressed data to the DAQ online farm. In heavy ion data taking, more sophisticated zero-suppression algorithm was required due to the high occupancy of the silicon strips. Thus the detector was read-out in raw mode without zero-suppression, and the improved zero-suppression algorithm was ran at the HLT.

The reason a more sophisticated zero-suppression algorithm is need for heavy ion run is because in heavy ion collisions, the occupancy in the first layer of the silicon strips can reach 20%. It is a challenge to correctly read out the signals in this dense environment. In particular the common mode calculation was studied in detail to ensure that no signal is subtracted in the zero-suppression process. An example of this study is shown in Fig. 3-6. Here the ADC readout of six modules is plotted versus strip number in the horizontal axis. The yellow highlighted region shows an example when the common mode was not properly calculated by the simple pp zero-suppression algorithm. These modules are identified and the raw digitized signals before pedestal subtraction are saved. This allows us to reprocess the data with a

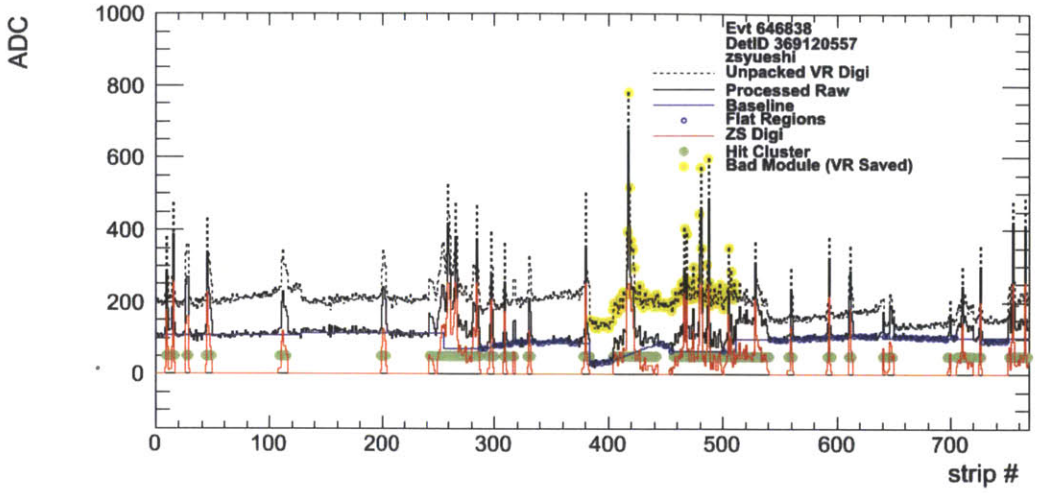


Figure 3-6: Illustration of the zero-suppression algorithm used during heavy ion data taking (Blue open circles connected by blue solid lines). The raw detector read-out is shown in dashed lines. The zero-suppressed values are shown in red solid lines. The yellow band highlights the identified module where the high occupancy makes it difficult for the simple CMS pp zero-suppression algorithm to reconstruct the correct baseline.

better zero-suppression in case we find a problem with the zero-suppression algorithm used during data time.

### 3.1.2 CMS Calorimeter

The CMS calorimeter is designed to measure the energies of electrons, photons and hadrons that emerge from the collision. The calorimeter system is crucial to the physics measurements at LHC for three reasons: First, its energy response resolution improves with energy, in contrast to magnetic spectrometers; second it allows the measurements of neutral hadrons, which cannot be detected by the tracker; third it provides the trigger system with quick detection of high $p_{\mathrm{T}}$ particles. For the jet fragmentation analysis, the CMS calorimeter provides the trigger as well the jet energy and direction measurements. CMS calorimeter is composed of an electromagnetic calorimeter (ECAL) and a hadronic calorimeter (HCAL). The ECAL is used mainly to measure electrons and photons through electromagnetic interactions such as bremsstrahlug and pair production. The hadronic calorimeter is used mainly to

measure hadrons through the strong interaction. Fig. 3-7 shows the locations of the ECAL and HCAL in and around the CMS magnet.

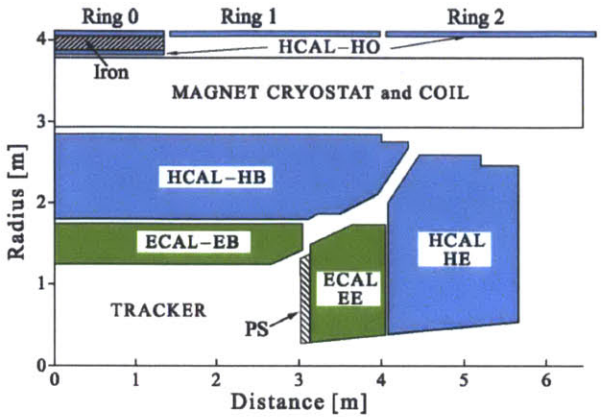


Figure 3-7: Location of the ECAL and the HCAL detectors (quarter slice-longitudinal cross section) in and around the CMS magnet

### CMS Electromagnetic Calorimeter

The Electromagnetic Calorimeter (ECAL) is a hermetic, homogeneous calorimeter comprising of lead tungstate ($PbWO_4$) crystals. These crystals have short radiation length of $X_0$=0.89cm and Moliere radius of 2.2 cm. They are fast (80% of the light is emitted within 25ns). However, the relatively low light yield requires use of photodetectors with intrinsic gain that can operate in a magnetic field. In the barrel, silicon avalanche photodiodes (APDs) are used; in the endcaps vacuum phototriodes (VPTs) are used. The use of $PbWO_4$ crystals allows the design of a compact calorimeter inside the solenoid. Fig. 3-8 shows the layout of the CMS electromagnetic calorimeter.

The barrel section (EB) has an inner radius of 129 cm. It is constructed with 36 identical "supermodules", each covering $0 < |\eta| < 1.479$. Each crystal covers 0.0174 in $\Delta\phi$ ($\approx$ 1 degree) and $\Delta\eta$. There are a total of 61200 crystals in the central barrel and 7324 crystals in the two endcaps.

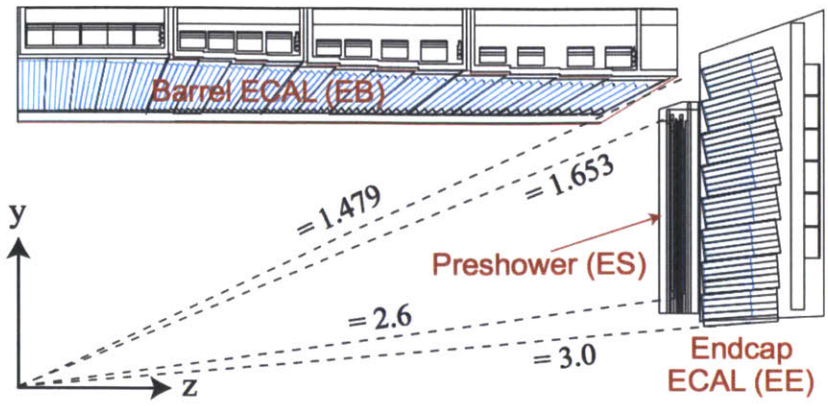


Figure 3-8: Geometry of the CMS electromagnetic calorimeter in a $\eta$-z slice.

### CMS Hadronic Calorimeter

The CMS Hadronic Calorimeter (HCAL) is mostly located inside the solenoid magnet and surrounds the ECAL system. Brass has been chosen as absorber material as it has a reasonably short interaction length (16.4 cm) and is non-magnetic. It is complemented by an additional layer of scintillators, referred to as the hadron outer (HO) detector, lining the outside of the coil. Fig. 3-9 shows the layout of the CMS hadronic calorimeter.

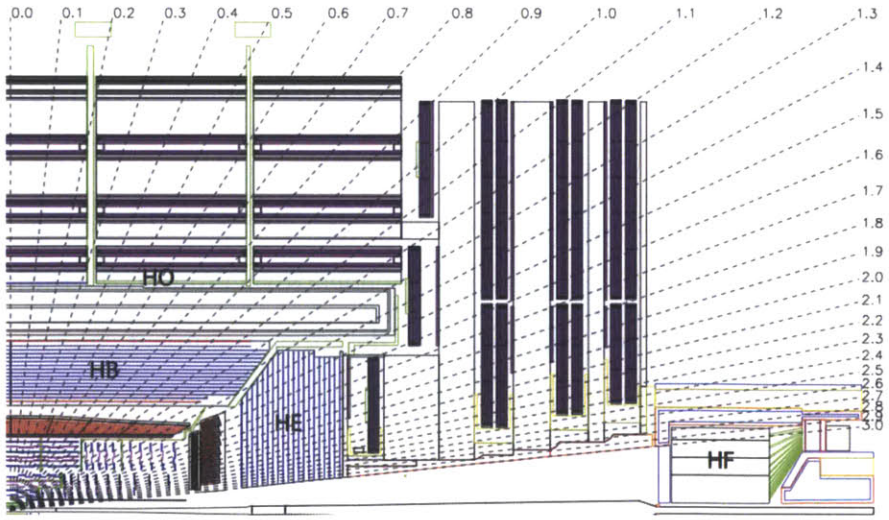


Figure 3-9: Geometry of the CMS hadronic calorimeter in a $\eta - z$ slice.

The hadron barrel (HB) part of HCAL consists of 32 towers coming the pseudorapidity region $-1.4 < \eta < 1.4$, resulting in a tower segmentation $\Delta\eta \times \Delta\phi = 0.087 \times 0.087$. The HB is constructed in 2 half barrels.

The hadron endcaps of HCAL cover the region $1.3 < |\eta| < 3.0$.

Finally steel/quartz fiber Hadron Forward (HF) calorimeter extends the calorimeter coverage to $|\eta| < 5$. Neutral component (ie. $\pi_0$) of the hadron shower is preferentially sampled in the HF detection strategy. The front face is located at 11.2 m from the interaction point. The signal originates from Cerenkov light emitted in the quartz fibers, which is then channeled by the fibers to photomultipliers. In this thesis, the HF is not used to analyze jet fragmentation. It is however used as a trigger to select minimum bias events.

### CMS Calorimeter Performance

One important challenge in the jet energy scale performance is the non-linearity of the HCAL response. Fig. 3-10 shows the single particle energy response of the CMS calorimeter.

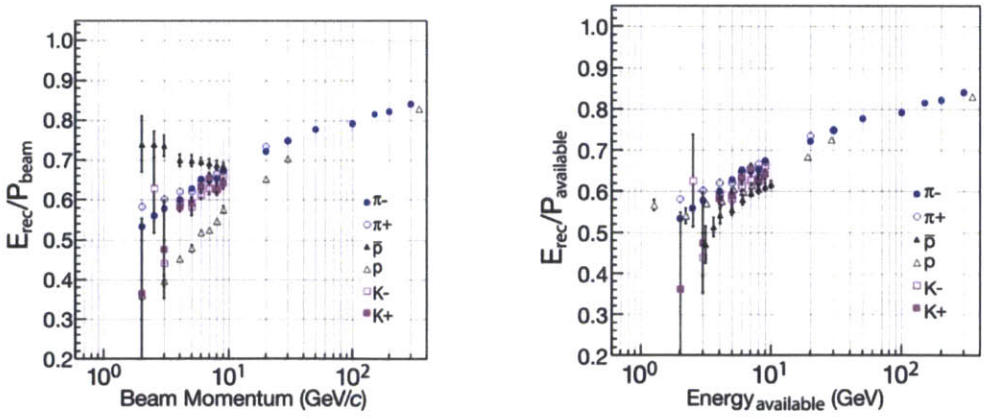


Figure 3-10: The response of the combined calorimeter system to six different particles is shown as a function of the beam momentum. Both the EB and HB are calibrated with 50 GeV/c electrons

This is one of the main reasons that in the thesis analysis, we use particle flow jet reconstruction (Sec. 3.5.1) which combines the calorimeter information with tracking

information.

### 3.1.3 Forward Detectors and Beam Monitoring

The Beam Scintillator Counters (BSC) are a series of scintillator tiles mounted on the inner side of the HF calorimeters. Situated at forward rapidity together with HF, BSC serves as a good minimum bias trigger for inelastic collisions. It is also used for beam-halo rejection.

The Beam Pick-up Timing for Experiments (BPTX) is a beam pickup device installed around the LHC ring to provide the detectors with the timing structure of the LHC beam. Two are specifically installed for CMS at 175 m left and right of the interaction point. The BPTX devices are cylindrical in shape. Proton beams passing through the enter of the BPTX induce a charge into the electrodes in the device that signals beam arrival time and position. During heavy ion data taking, the BPTX signal is used as a gating for the physics triggers to reduce beam background related noise.

### 3.1.4 CMS Trigger and Data Acquisition

Due to the high volume of data output in both pp and PbPb, data from only about O(100) events per second can be written to archival media. The goal of the CMS data acquisition is to record all interesting physics events, sampling the full collision luminosity, while at the same time reducing the total data volume. This is realized by a triggering system in the read-out.

The CMS trigger and data acquisition system consists of 4 parts: the detector electronics, the Level-1 trigger processors (calorimeter, muon, and global), the readout network, and an online event filter system (processor farm) that executes the software for the High-Level Triggers (HLT). A diagram of the CMS trigger and data acquisition system is shown in Fig. 3-11

The Level-1 (L1) trigger is a firmware based triggering system. Thus it can process events with a design output rate of 100kHz in pp collisions. The L1 triggers are

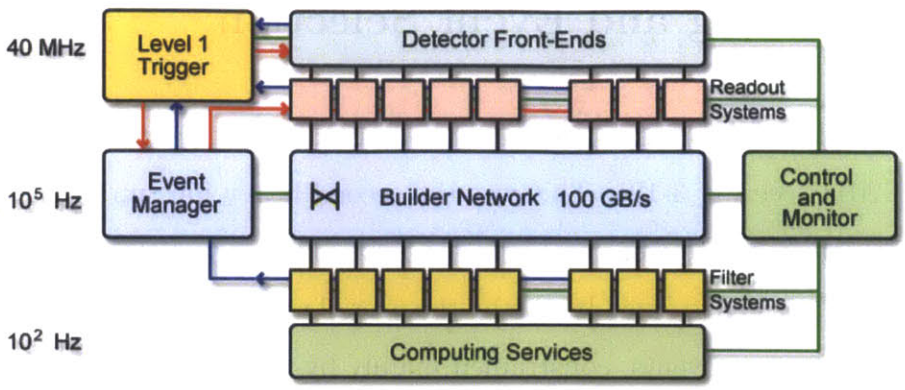


Figure 3-11: The CMS trigger and data acquisition system.

based on information from the CMS calorimeter and muon system, both of which are detectors that have fast detection time and readout. The HLT is comprised of an online computing farm running full event reconstruction algorithms based on the offline analysis reconstruction. The fact that software reconstruction is used at the second trigger level to select events online is the power of CMS trigger system. Because the heavy ion event sizes are much larger than pp by up to an order of magnitude for the central events, the readout bandwidth of the CMS detector in HI configuration is about 3.5 kHz.

The remaining parts of the CMS detector are not highlighted in this thesis. For further reading and details of the CMS detector, see [30].

## 3.2 Triggering and Event Selection

The data sample used for the thesis analysis was taken from the heavy ion run in November, 2011 (see Fig 3-12). This was the second heavy ion run at the LHC and the inelastic collision rate went as high as 5 kHz. The trigger strategy of CMS for PbPb collisions was constrained by the by the overall rate limitations of about 150 Hz (physics) for recording events, constrained mainly by the volume of data that could be stored permanently.

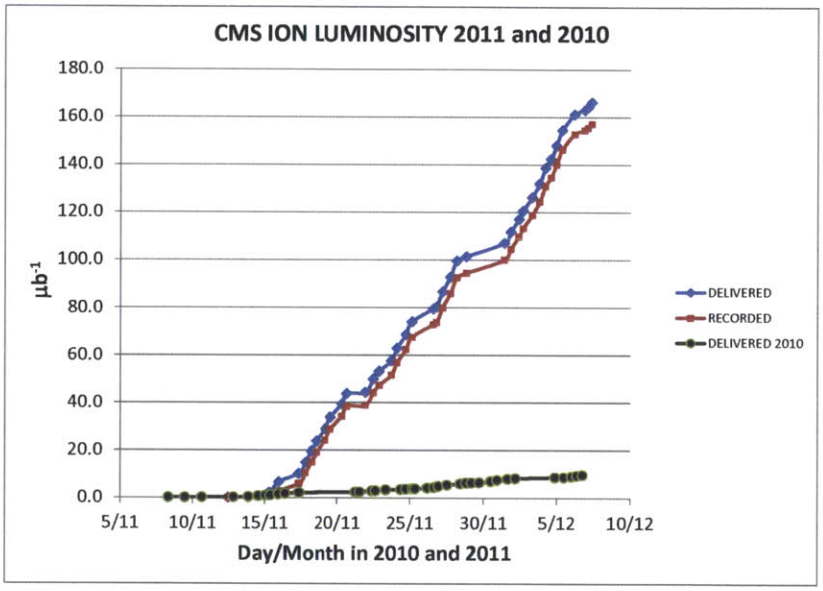


Figure 3-12: Cumulative amount of data collected as a function of time during the 2010 and 2011 heavy ion runs at the LHC.

For these reasons, the L1 trigger system had to provide a very efficient and clean trigger on hadronic collisions, with no or moderate (2 or 3) prescale for minimum bias events. The L1 also had to provide efficient and unprescaled seeds for the High Level Trigger (HLT) of high-$p_T$ jets, muons, or photons.

### 3.2.1 Selecting collisions with high energy jets

Since typically only about O(100) Hz of the collision events can be recorded, making use of the jet triggers at the L1 and HLT levels is necessary to keep the full jet statistics.

In in the L1 trigger, jet triggers with $p_{\mathrm{T}} > 36$ GeV/c and $p_{\mathrm{T}} > 52$ GeV/c thresholds were enabled. The L1 jet trigger essentially looks for local maxima in $\eta, \phi$ map of the energy deposited in L1 calorimeter trigger regions. The L1 calorimeter trigger regions are made of 3 by 3 calorimeter towers. Because there is no underlying event subtraction, the L1 jet triggers are not highly selective in central collisions. It selects about 30% of the inelastic collisions and almost all of the central collisions. Thus the required rate reduction of the trigger is achieved in the HLT.

In the HLT, full jet reconstruction is performed using calorimeter energy inputs and the iterative cone jet algorithm with radius 0.5. An iterative background subtraction algorithm is preferred to subtract contributions from the underlying event as is done offline (Sec. 3.5.3). Four trigger thresholds were used, with $p_{\mathrm{T}} > 55$, 65, 80 and 95 GeV/$c$. These HLT bits are seeded by the L1 jet triggers. Due to the full jet reconstruction and background subtraction, the HLT jet triggers reduced the rate of these triggers, with respect to the rate of the L1 seed, by roughly an order of magnitude.

The HLT trigger thresholds and prescales were chosen based on trigger studies during preparations that lead up to the 2011 PbPb data taking. The studies optimized the trigger thresholds and prescales based on the 2010 data and Monte Calo simulation. Fig. 3-13 shows the HLT trigger efficiency and fake rate; Fig. 3-14 shows the projected HLT accept rate based on the accept fraction in 2010 minimum bias PbPb data and for a predicted interaction rate of 2 kHz in the 2011 data.

For the jet fragmentation analysis in this thesis, the trigger that was finally used to select events for the analysis is the HLT jet trigger with threshold of 80 GeV/c (HLT_HIJet80). Motivation for this choice was that HLT_HIJet80 was never prescaled, and it had a low enough threshold not to have any bias for selecting jets

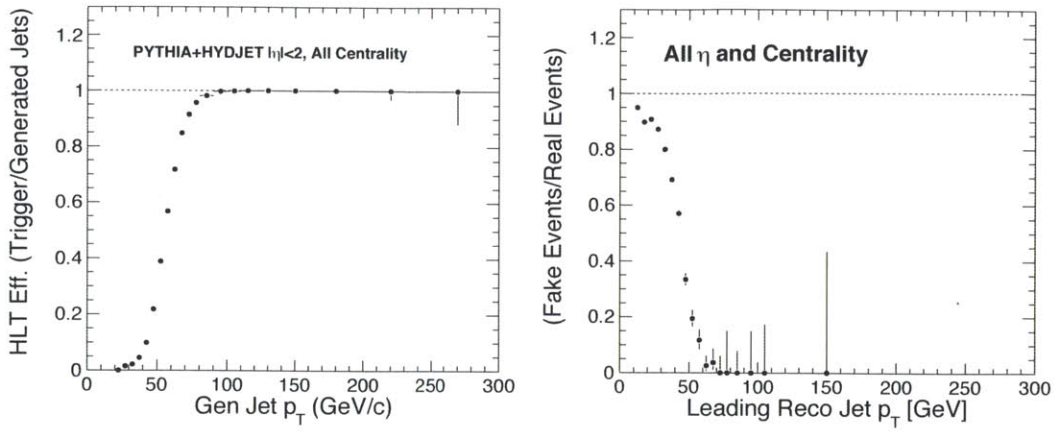


Figure 3-13: HLT jet trigger efficiency (left) and fake rate (right) based on Monte Calo simulation.

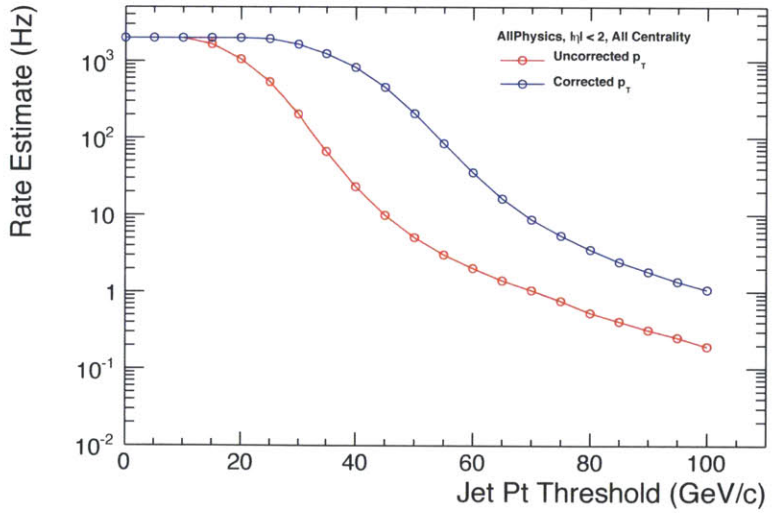


Figure 3-14: Projected HLT jet trigger accept rate as a function of trigger threshold based on 2010 minimum bias PbPb data. Blue points are for rates if trigger thresholds are applied on corrected jet energy. Red points are for rates if trigger thresholds are applied on raw jet energy. Rates correspond to inelastic collision frequency of 2kHz.

above 100 GeV/$c$ off-line.

The efficiency turn-on for the HLT_HIJet80 trigger plotted as a function of the offline particle flow jet corrected $p_{\mathrm{T}}$ is shown in Fig. 3-15. The efficiency is the ratio of the number of triggered events over the number of minimum bias events, as a function of the $p_{\mathrm{T}}$ of the leading offline jet. The turn-on is not infinitely sharp since the offline jet reconstruction used here included more sophisticated jet reconstruction (particle flow jet reconstruction, Sec. 3.5).

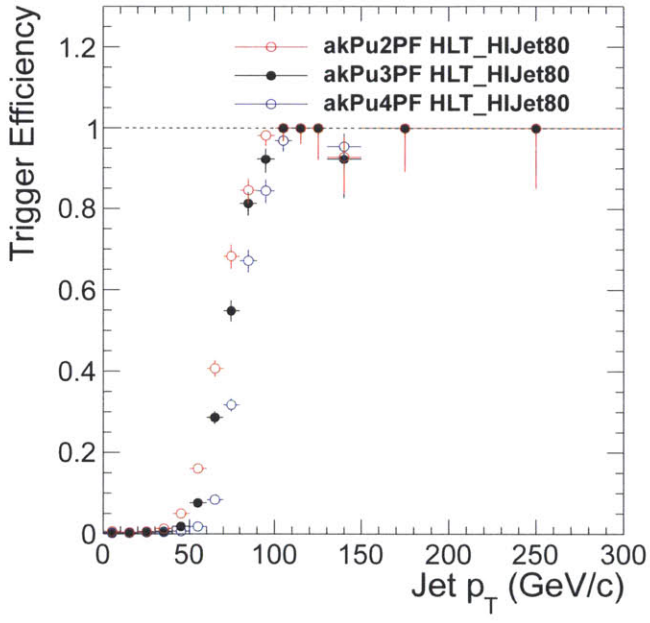


Figure 3-15: Efficiency curves for the HLT_HIJet80, as a function of the leading jet transverse momentum with $|\eta| < 2$ evaluated from minimum bias sample.

The selection of events for the present analysis was based on the above HLT triggers on jets. To obtain a pure sample of inelastic collisions, further offline event selection cuts were applied.

### Cleaning of events with anomalous signals in the HCAL

Early commissioning of the CMS HCAL have identified low rates of HCAL read-out noise, reporting spurious energy deposition. Rejection algorithms have been developed to remove such falsely triggered events from the HLT dataset [31]. Studies

performed with the 2010 PbPb data found that a basic collision event selection removed the majority of such HCAL noise events[32]. Nevertheless, the standard CMS HB/HE noise filter were applied with a few parameters adjusted for the high multiplicity environment in PbPb collisions as done in [11].

#### Jet quality identification by leading track

To reduce any remaining detector noise, jets are selected which compare the maximum track $p_{\mathrm{T}}$ within a jet to that of the total jet $p_{\mathrm{T}}$, keeping those jets with a ratio greater than 0.01. This selection rejects $\approx 1\%$ of jets in Monte Carlo studies.

### 3.2.2 Offline Collision Event Definition

Finally there can be triggered events due to beam gas, beam background (called PKAM, Previously Known As "Monster") events, a few more offline event selections are applied to select real inelastic PbPb collision events. These cleaning cuts are primarily used for minimum bias event selection, and have only a small effect on the selected jet events. But as mentioned earlier, they help to reduce jet events triggered by detector noise. Thus the following collision event definition selections are made on the jet dataset on top of the previous jet event selections:

1. Beam halo filter: events where any of the BSC halo bits fired (L1 Technical Trigger bits 36, 37, 38 or 39) were excluded from the analysis. This happened only in 0.5% of the events triggered by the HLT jet trigger with 50 GeV/$c$ threshold, thus any possible biases are negligible. Figure 3-16 shows a correlation between the number of hits in the first pixel layer and the total HF energy. Collisions passing all offline event selections (colored points) have a very tight correlation between the two quantities. However, events that fire the BSC beam halo bits have very small HF energy and quite a large number of pixel hits (black points near vertical axis). These are excluded from the analysis.

2. Requirement of a reconstructed 2-track primary vertex was imposed. This requirement removes non-inelastic-collision events (e.g. beam-gas) with large HF

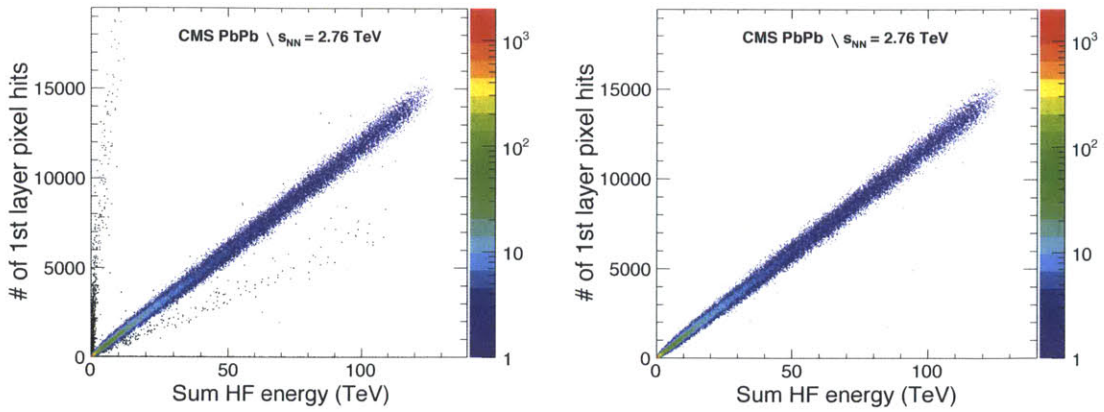


Figure 3-16: (Left panel) Correlation for 60k minimum bias events in one collision run (151077) between the number of pixel hits and the total energy deposited by the HF. Good collisions (colored points) have a tight correlation, while events firing the BSC halo bits, displaying PKAM-like features, or lacking a valid reconstructed vertex are off-diagonal (black points). (Right panel) The same correlation for only those events passing all selection cuts described in the text.

energy deposits but very few pixel hits (black points just above the horizontal axis in Fig. 3-16).

3. A cut to remove PKAM events, which is a requirement of pixel cluster-length compatibility with the vertex. This cut is the same as it was for the first 7 TeV $pp$ paper on $\mathrm{dN/d}\eta$ and $\mathrm{dN/d}p_T$ [33]. In Fig. 3-16, most background events with an excess of pixel hits compared to HF energy are removed by this selection. Some are already removed by the BSC beam halo filter alone, but all are eliminated by the combination of these two cuts.

4. A requirement of an off-line HF coincidence, which requires at least 3 towers on each side of the interaction point in the HF with at least 3 GeV total deposited energy.

## 3.3 Centrality Determination

Since the colliding Pb nuclei have finite extent in size, it is important to know the "centrality" of the collision, i.e., the amount of overlap (or impact parameter) between the two colliding nuclei. In this analysis, the observable used to determine centrality is the total energy deposited in both HF calorimeters. The distribution of the HF signal used in this analysis is shown in Fig. 3-17 (a). The central events are head-on collisions, with small impact parameter, that produce many particles (and hence total HF energy) because of the large number of nucleon-nucleon interactions. These central collisions are rare since there are fewer ways for the nuclei to hit exactly head-on. In contrast, peripheral events are glancing collisions which produce few particles. They are more frequent because there are more ways for the nuclei to imperfectly hit each other.

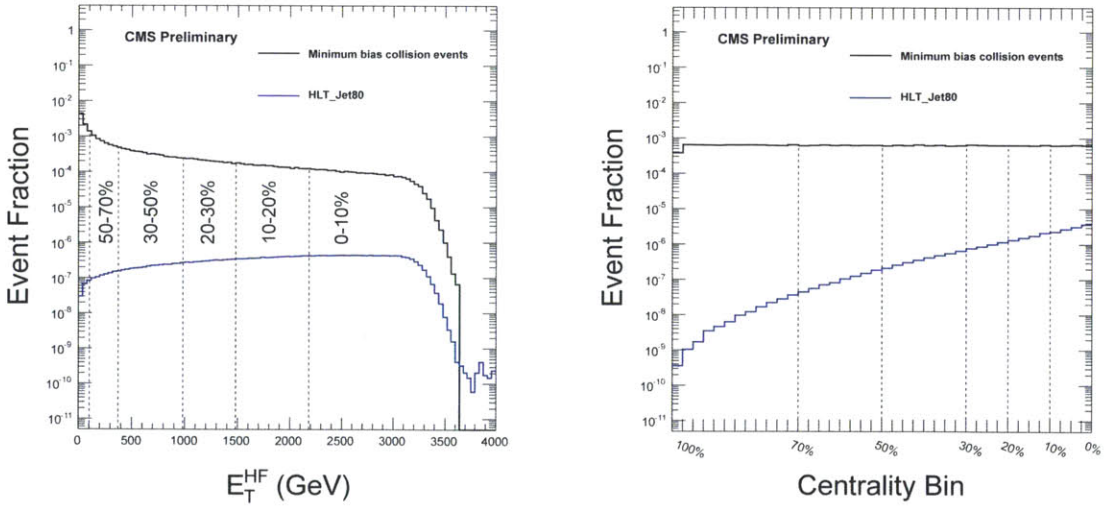


Figure 3-17: Left: Sum of HF $E_{\mathrm{T}}$ for minimum bias collisions (black) compared to those in jet triggered events (blue) in PbPb. Centrality bin division is shown with the dotted lines. Right: Centrality bin event fraction for minimum bias collisions (black) - flat by definition, compared to jet triggered events (blue shaded histogram).

The distribution of this total energy was used to divide the event sample into 40 centrality bins, each representing 2.5% of the total inelastic nucleus-nucleus interaction cross section. Because of inefficiencies in the minimum bias trigger and

event selection, the measured multiplicity distribution does not represent the full interaction cross section. MC simulations were used to estimate the distribution in the regions where events are lost, mostly occurring in the peripheral bin. Comparing the simulated distribution to the measured distribution, it is estimated that the minimum bias trigger and event selection efficiency is $97 \pm 3\%$.

Monte Carlo models (called Glauber model, reviewed in [34]) can be used to correlate centrality, as quantified by the fraction of the total inelastic collision cross section, with physical characteristics of the collision. For example the central collisions can be related to events with small impact parameters. Two other useful physical quantities are denoted $N_{part}$ and $N_{coll}$. $N_{part}$ is the total number of nucleons in the two nuclei which experienced at least one inelastic collision. $N_{coll}$ is the total number of binary nucleon-nucleon collisions.

Note that the selection of rare processes, such as the production of high $p_{\mathrm{T}}$ jets, lead to a strong bias in the centrality distribution of the triggered events towards more central events. This is because in more central events, $N_{coll}$ is very large and so more likely for high $p_{\mathrm{T}}$ jets to be produced. This bias can be seen clearly in Fig. 3-17 (b), where distributions of minimum bias (black line) and jet triggered events (blue shaded histogram) in the 40 centrality bins are shown.

## 3.4 Event and Detector Simulation

In this analysis, Monte Carlo (MC) simulations have been used primarily for evaluation of reconstruction performance, particularly in determination of tracking efficiency, and jet energy response and resolution. These studies mainly use QCD jet events simulated by PYTHIA MC generator [35] (version 6.423, tune Z2). These simulated PYTHIA events are propagated through the CMS detector using the GEANT4 package [36] to simulate the detector response.

In order to have rich statistics in all jet $p_{\mathrm{T}}$ ranges, different samples are produced with various cut-off values of $\hat{p}_{\mathrm{T}}$. These samples are combined with their corresponding cross-section values as weights.

In order to account for PbPb underlying event effects, the PYTHIA events are embedded into fully simulated PbPb events, generated by HYDJET [37], which is tuned to describe the minimum-bias PbPb data. The embedding is done by mixing the simulated digital information from PYTHIA and HYDJET. Table 3.1 summarize the number of events simulated for each sample.

Table 3.1: Summary of MC simulation statistics

| Generator | Process | Cross section (mb) | Number of events |
|---|---|---|---|
| Hydjet | Minimum Bias | $7640 \pm 420$ (Glauber) | 37k |
| Pythia + Hydjet | $\hat{p}_{\mathrm{T}} > 30$ GeV/$c$ | $1.079 \times 10^{-2}$ | 110k |
| Pythia + Hydjet | $\hat{p}_{\mathrm{T}} > 50$ GeV/$c$ | $1.021 \times 10^{-3}$ | 190k |
| Pythia + Hydjet | $\hat{p}_{\mathrm{T}} > 80$ GeV/$c$ | $9.913 \times 10^{-5}$ | 180k |
| Pythia + Hydjet | $\hat{p}_{\mathrm{T}} > 100$ GeV/$c$ | $3.069 \times 10^{-5}$ | 890k |
| Pythia + Hydjet | $\hat{p}_{\mathrm{T}} > 120$ GeV/$c$ | $1.128 \times 10^{-5}$ | 180k |
| Pythia + Hydjet | $\hat{p}_{\mathrm{T}} > 170$ GeV/$c$ | $1.47 \times 10^{-6}$ | 76k |
| Pythia + Hydjet | $\hat{p}_{\mathrm{T}} > 200$ GeV/$c$ | $5.31 \times 10^{-7}$ | 67k |
| Pythia + Hydjet | $\hat{p}_{\mathrm{T}} > 250$ GeV/$c$ | $1.192 \times 10^{-7}$ | 55k |
| Pythia + Hydjet | $\hat{p}_{\mathrm{T}} > 300$ GeV/$c$ | $3.176 \times 10^{-8}$ | 74k |

## 3.5 Jet Reconstruction

This section aims to describe how the jets used in the fragmentation function measurement are reconstructed. The reconstruction of jets can be divided into two main steps: first, basic inputs in the form of 4-momentums that represent the particles in the event are reconstructed; second, jet clustering algorithm is ran on the basic 4-momentum inputs to form the final list of jets. In the traditional approach at hadron colliders, the basic inputs are formed mainly from calorimeter hits. In this thesis, a more recently developed approach, called CMS particle flow algorithm [38], is employed. In the particle flow approach, information from all CMS sub-detector systems are used. In the following subsections, the particle flow reconstruction is described in more detail. After that, the jet clustering algorithm, including the background subtraction scheme, is described. Finally the performance of the reconstructed jets is evaluated.

### 3.5.1 Particle Flow Reconstruction

The idea of the particle flow event reconstruction is to identify and classify all stable particles in the event, i.e., electrons, muons, photons, charged hadrons, and neutral hadrons, by combining information from all CMS subdetectors. This allows the optimal use of the strengths of the different CMS subdetectors that are designed to measure different types of particles.

Charged particles are reconstructed by the CMS tracker with high precision. Photon are reconstructed with an excellent energy resolution by the ECAL. Charged and neutral hadrons deposit their energy in the HCAL. Muon candidates are the particles that can pass through both the ECAL and HCAL because they are minimally ionizing particles and do not interact strongly. The muons are then detected in the muon chambers. Muons are not relevant for jet reconstruction unless the analysis is related to heavy flavor jets. In the thesis analysis where inclusive jet fragmentation function is measured, discussions of muons are omitted.

Reconstructed objects from different subdetectors are combined together to form

particles. It is important to make sure that for each particle, information from all subdetectors are linked together. This ensures there is no double counting of energy in the event. This linking process is illustrated in Fig. 3-18.

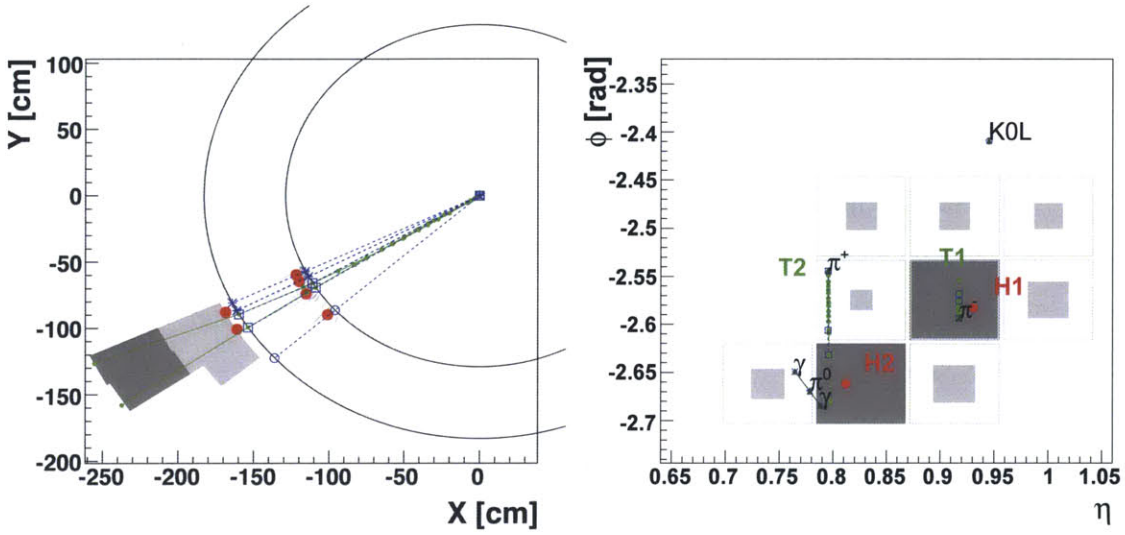


Figure 3-18: A Particle Flow reconstruction event display of a simple hadronic jet in the $(x, y)$ view (left) and in the $\eta$, $\phi$ view on the HCAL surface (right). The HCAL surface is the larger circle at a radius of $\sim$ 1.8m from the interaction point in the left figure. In both figures, the Particle Flow clusters are shown as red dots. Blue dashed lines are the simulated particles given by the generator. Green solid lines are the reconstructed tracks. The gray tower cells in the left figure and gray boxes in the right figure show the hit HCAL cells. The gray area is proportional to the logarithm of the energy measured in each cell. The open green markers represent charged hadron candidates because the tracks are linked to the hits primarily in the HCAL. The $*$ markers represent photon candidates because the ECAL clusters (not shown) are not linked to any tracks. (Figure from [38])

Compared to the traditional approach of using only calorimeter information to form jets, particle flow algorithm improves jet reconstruction energy response. This is mainly due to the use of tracker information. By using the track momentum of charged hadrons instead of HCAL energy, effects of the non-linear HCAL response (as shown in Fig. 3-10) is reduced. Also the use of tracking information reduces dependence of the jet energy on the jet fragmentation pattern. This is illustrated in Fig. 3-19.

Fig. 3-19 shows the corrected response to quark and gluon jets in PYTHIA events.

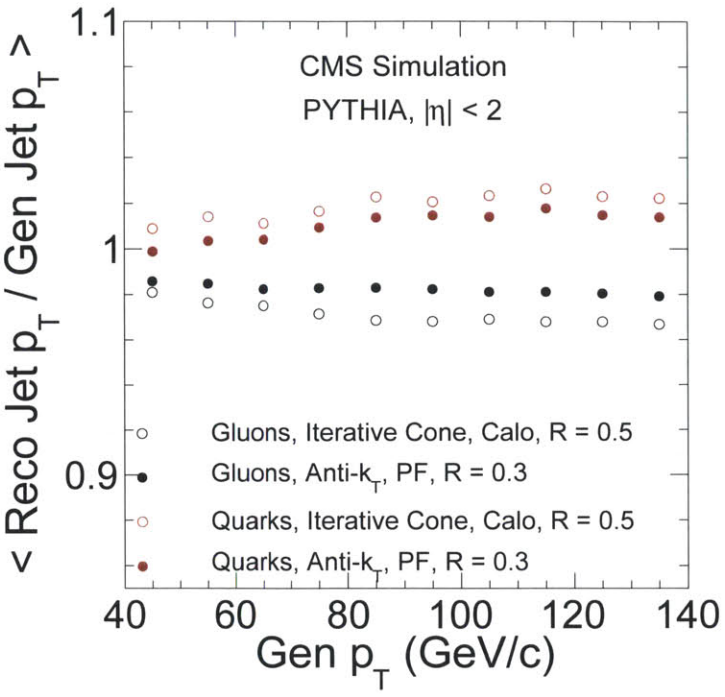


Figure 3-19: The jet response for quark and gluon jets for particle-flow and calorimeter jet reconstruction in PYTHIA.

Quark jets have a harder fragmentation pattern than gluon jets, on average, and thus show a larger response. This difference in response between quark and gluon jets is reduced for particle-flow jets, compared to calorimeter jets.

In heavy ion collisions, particle flow is run in nearly the same configuration as in *pp* collisions, with a few exceptions. Most notably, the reconstruction of charged particle tracks uses a different algorithm and different quality selections, as described in the next section. Particle flow electron reconstruction, links to elements from the pre-shower detector, and identification of nuclear interactions are disabled.

### 3.5.2 Jet Algorithm

Recall from Sec. 2.2.2 that due to asymptotic freedom, only the final state stable fragmentation particles are detected experimentally and never the partons themselves. A clustering algorithm is needed to identify and combine the final state particles into jets. As a result jets need to be defined. A jet definition is a set of rules for how

to group particles into jets and to assign a momentum to the resulting jet. A good jet definition should be applicable to experimental measurements, to the output of parton-shower Monte Carlo simulations, and to partonic calculations [39]. The first part of the jet definition consists of a prescribed set of rules for grouping particles into jets. These rules are called jet algorithms. The jet algorithms usually have some parameters that are related to the size of the resulting jets. Once the jets are found, a scheme is needed to combine the energy of the constituent particles to form the jet energy (the simplest approach is to directly add their 4-vectors). Taken together, a jet algorithm with its parameters and an energy recombination scheme form a "jet definition".

Over the decades since the first proposals to measure jets, a number of jet algorithms have been developed. They each have different strengths and weaknesses, experimentally or theoretically. In an attempt to arrive at some standard of a unified experimental and theoretical definition, a set of properties was agreed in 1990. It came to be known as the "Snowmass accord". It states that the properties of a jet definition should include [40]:

1. Simple to implement in an experimental analysis;

2. Simple to implement in the theoretical calculation;

3. Defined at any order of perturbation theory;

4. Yields finite cross sections at any order of perturbation theory;

5. Yield a cross section that is relatively insensitive to hadronization

In the most recent CMS analyses that involve jets, and also in this thesis, the anti-$k_T$ algorithm was chosen as the choice jet algorithm which conforms to the Snowmass accord. In the following section, we will motivate this choice of jet algorithm by expanding a little more on some of the properties in the Snowmass accord.

### Infrared and Collinear Safety

One important requirement of the Snowmass accord for a jet definition is that the resulting jets cross sections be theoretically calculable. In this case, the theory being pQCD, it implies that the cross sections converge at higher orders. Recall that the soft and collinear gluon radiation processes ($q \rightarrow qg$) are divergent in pQCD, as seen in Eq. 2.4. Normally these divergent diagrams are canceled by corresponding loop matrix elements that enter with the opposite sign. This is illustrated in (a) and (b) of Fig. 3-20.

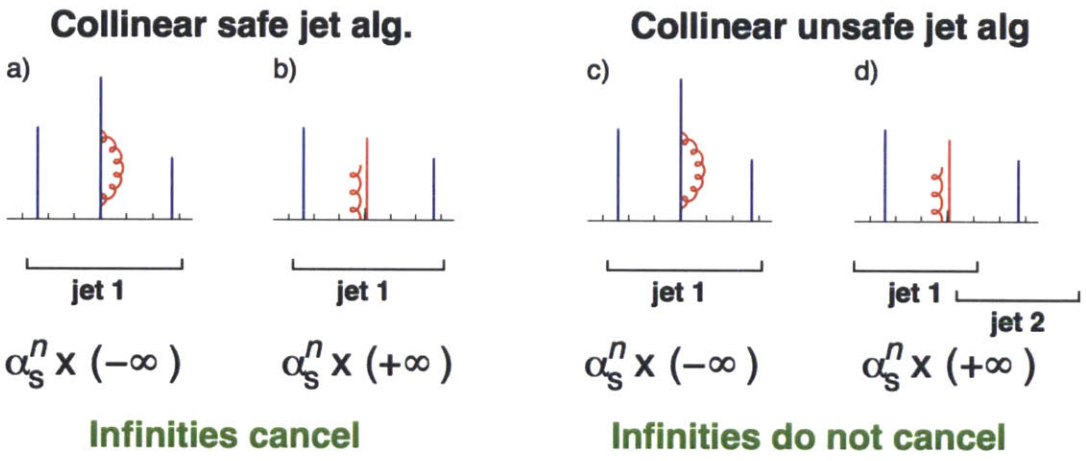


Figure 3-20: Illustration of collinear safety (left) and collinear unsafety (right) together with its implication for perturbative calculations. Partons are vertical lines, their height is proportion to their transverse momentum, and the horizontal axis indicates rapidity. (figure from [39])

If the jet algorithm determines one set of jets with the tree level splitting diagrams, while giving a different set of jets with the loop diagrams, then the canceling no longer work, leading to infinite cross sections in perturbation theory [39]. For example cone algorithms are a general class of algorithms traditionally used at hadron colliders due to their speed and robustness. Essentially, cone algorithms work by starting from some seed particle, draw a cone around the particle and move the cone direction towards the energy centroid of the cone. Once the cone direction coincides with the cone energy centroid, then the cone is stable and it is declared as a jet. The problem

with this is that the requirement of an initial hard particle as the seed to the algorithm can disrupt the cancellation of the divergent diagrams. This is illustrated in (c) and (d) Fig. 3-20. The splitting of the high $p_{\mathrm{T}}$ seed particle into two collinear particle with lower $p_{\mathrm{T}}$ can have the consequence that another high $p_{\mathrm{T}}$ particle suddenly becomes the hardest particle in the event, thus leading to a different set of final jets.

Another difficulty occurs in cone algorithms where all particles above some minimal threshold are used as seeds. Here the addition of a new soft particle can lead to new stable cones being found and thus changing the final set of jets. This is illustrated in Fig. 3-21.

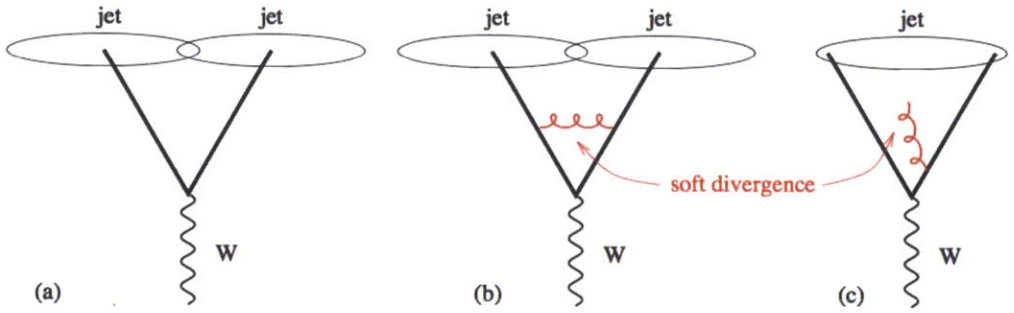


Figure 3-21: Illustration of infrared unsafety. The addition of a soft gluon converts the event from having two jets to just one jet. Here the explicit angular directions of the partons are shown. (figure from [39])

In short, the Snowmass accord practically implies that a good jet algorithm should determine a list of final jets independent of the presence of collinear splitting or the presence of additional soft particles. This is what is meant by infrared and collinear (IRC) jet algorithms.

### Anti-$k_T$ Algorithm

The anti-$k_T$ algorithm [41], as encoded in the *FastJet* framework [42], is a type of sequential recombination jet algorithm. Sequential recombination algorithms are algorithms that repeatedly recombine pairs of particles that are close in some distance measure. Because this recombination scheme in some sense reverses the QCD parton branching, it has the advantage of usually being IRC safe. To be specific the algorithm

can be summarized as ([39]):

1. For each pair of particles $i, j$ work out the particle-pair distance measure

$$d_{ij} = \min(p_{ti}^{-2}, p_{tj}^{-2}) \frac{\Delta R_{ij}^2}{R^2}, \tag{3.1}$$

   In addition, for each particle work out the particle-beam distance measure

$$d_{iB} = p_{ti}^{-2}, \tag{3.2}$$

   Where $\Delta R_{ij}^2 = (\eta_i - \eta_j)^2 + (\phi_i - \phi_j)^2$ is the angular distance in $\eta, \phi$ space, and R is a parameter of the algorithm that acts similar to the role of a cone radius, as will be explained shortly.

2. Find the minimum of the $d_{ij}$ and $d_{iB}$.

3. If it is a $d_{ij}$ , recombine $i$ and $j$ into a single new particle and return to step 1.

4. Otherwise, if it is a $d_{iB}$, declare $i$ to be a [final-state] jet, and remove it from the list of particles. Return to step 1.

5. Stop when no particles remain.

The word $k_T$ is related to the $\frac{\Delta R_{ij}^2}{R^2}$ term which denote a measure of relative transverse momentum between the two particles. The name anti-$k_T$ reflect the inverse $p_T^2$ in the equations. This inverse momentum term prioritize hard particles over soft particles. Thus the jets grow outward around hard particle "seeds". This helps the algorithm to be insensitive to additional soft particles either from soft QCD radiations or from the underlying event background. And unlike cone algorithms, anti-$k_T$ algorithm is also collinear safe because a collinear branching automatically gets combined at the beginning of the sequence. We see that R determines the size of the jet: if a particle $i$ has no other particles within a distance R then $\frac{\Delta R_{ij}^2}{R^2} > 1$ and thus the $d_{iB}$ will be smaller than the $d_{ij}$. The result is a IRC safe algorithm that gives rise to circular hard jets, making it a good replacement for the traditional cone algorithms.

These are the reasons anti-$k_T$ algorithm was chosen as the default jet algorithm in CMS.

In this thesis, anti-$k_T$ algorithm with R=0.3 is used to combine the particle-flow candidates into jets. The small effective cone size (as compared to 0.5) helps to reduce the sensitivity of jet reconstruction to distortions in the energy scale that could arise by picking up radiated energy from the quenching process or from fluctuations of the background from soft collisions.

### 3.5.3 Underlying event subtraction

One of the major challenges to jet reconstruction in heavy ion collisions is to understand the uncorrelated background within the selected jet cone due to the large multiplicity in the heavy ion collisions.

The algorithm used in this thesis to subtract the underlying event background is a variant of an iterative "noise/pedestal subtraction" technique. This technique is designed for discrete quantification of the energy in $\eta$ and $\phi$, which works well for a calorimetric measurement. To use the same subtraction code to candidates reconstructed with particle flow, which have a continuous distribution in momentum space, a calorimeter tower geometry is imposed on the PF objects [43]. This is performed by summing up the $p_{\mathrm{T}}$ of the PF candidates that point to a fixed $\eta \times \phi$ bin that corresponds to the HCAL cell granularity, as shown in Fig. 3-22. Here the $p_{\mathrm{T}}$ is evaluated with respect to the momentum values of candidates at the vertex, not the calorimeter surface. After this projection, the mean value $< E_{\mathrm{cell}} >$ and dispersion $\sigma(E_{\mathrm{cell}})$ of the energies in each of these cells are calculated from the ring of cells at the same pseudorapidity. This approach is the same as employed in [44] and originally described in [45].

A pedestal energy is subtracted from each cell with the cell energy being set to zero in the case that the pedestal value is larger than the cell energy. The algorithm subtracts $\langle E_{\mathrm{cell}} \rangle + \sigma(E_{\mathrm{cell}})$, rather than $< E_{\mathrm{cell}} >$, from each cell in order to compensate for the bias caused by this elimination of negative energy. The jet clustering algorithm is run on the subtracted towers. The pedestal calculation is then redone excluding

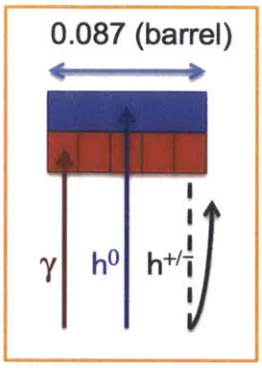


Figure 3-22: Projection of PF candidates into calorimeter tower geometry in $r - \phi$ view. The blue block represents one single barrel HCAL cell ($\Delta\phi = 0.087$). The red blocks represent the 5 ECAL cells ($\Delta\phi = 0.0174$) which fit into a single HCAL cell.

cells within R $< 0.5$ ($R = \sqrt{\phi^2 + \eta^2}$) of any jet of $p_{\mathrm{T}} > 15$ GeV/$c$. The threshold of 15 GeV/$c$ was chosen based on a study where response and resolution are optimized in central dijet embedded in PbPb simulations. The cell energies are updated with the new pedestal function (again subtracting mean plus dispersion). The final sample of jets is then reconstructed from this set of pseudo-towers.

### Underlying event simulation comparison to data

A crucial issue in the evaluation of jet reconstruction performance is the understanding of the local fluctuations in the underlying event, and the accuracy of the simulation of these effects. For this, minimum bias events are analyzed by summing up energies in cones with randomly determined axes. The estimated background fluctuations are shown in Fig. 3-23. It shows that the background fluctuations as a function of centrality are consistent between data and HYDJET. The estimated background can also be subtracted from these random cones (taking a tower energy to be zero if it is below the amount of estimated background), and the subtracted energy distributions describe the positive part of the fluctuations of reconstructed jet energy.

To further understand the background behavior, one can sum up the estimated background for each jet, and plot the distributions of this background as a function of jet $p_{\mathrm{T}}$ and centrality. The subtracted background $\langle p_{\mathrm{T}} \rangle$ for reconstructed jets within

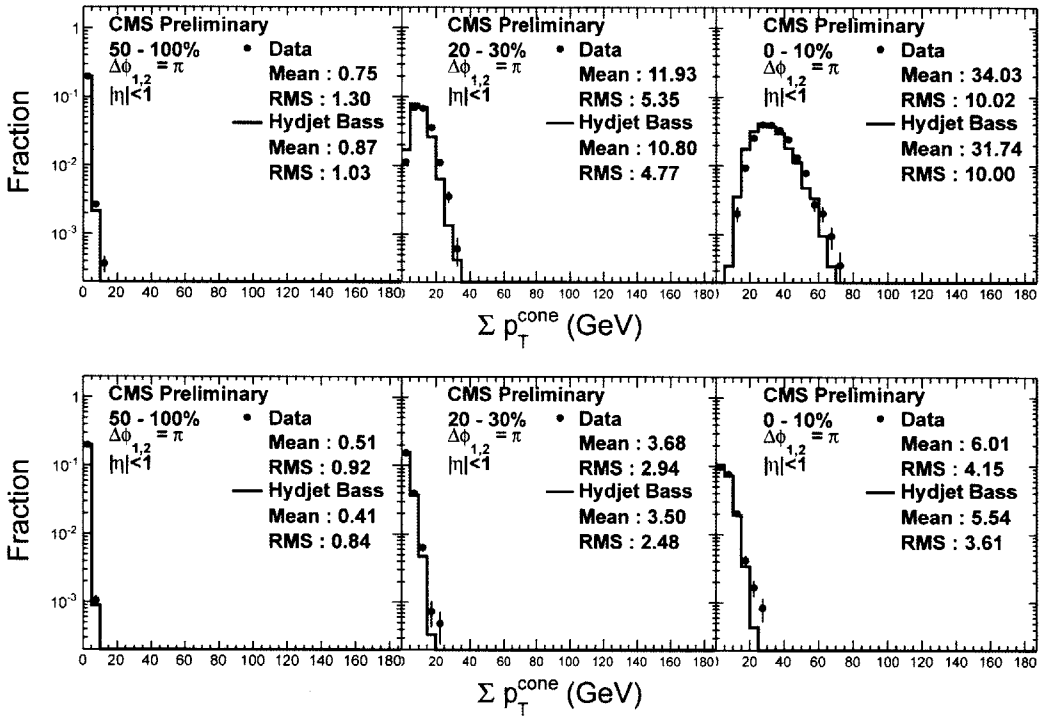


Figure 3-23: Study of background fluctuations by random cones, from peripheral (left) to central (right) events. Data are represented by filled circles, minimum bias HYDJET simulations by lines. The top row is the sum of $p_{\mathrm{T}}$ in a cone of size 0.3, and the bottom row shows the sum of $p_{\mathrm{T}}$ subtracted from that cone, where pseudotowers that fall below the estimated background are not counted. Error bars are statistical.

$|\eta| < 2$ as a function of collision centrality for anti-$k_{\mathrm{T}}$ PF jet algorithm with a resolution parameter of $R = 0.3$ in PbPb collisions data can is shown in Fig. 3-24. The average background (in terms of $\langle p_{\mathrm{T}} \rangle$ and RMS) is consistent with simulations over the wide range of reconstructed jet $p_{\mathrm{T}}$.

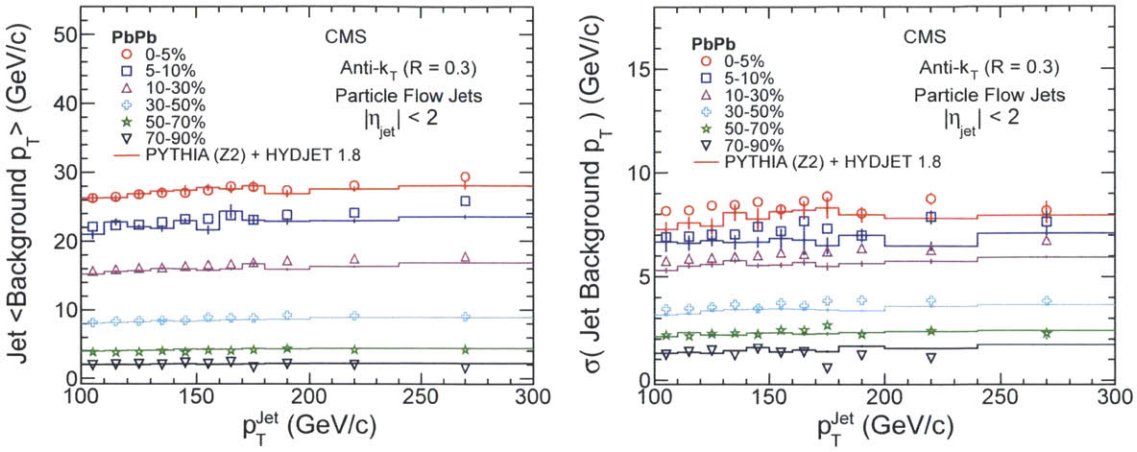


Figure 3-24: Subtracted underlying event background $p_{\mathrm{T}}$ for jets reconstructed with $100 < p_{\mathrm{T}}(\,\mathrm{GeV}/c) < 110$ for different PbPb collision centralities. Data is represented by closed symbols, MC by the histogram, and statistical uncertainty is shown.

### 3.5.4 Jet Energy Scale and Resolution

CMS uses a factorized multi-step approach to correct the jet energy [46]. The separate relative ($\eta$) and the absolute ($p_T$) correction steps are required to correct for the variation in jet energy response in pseudorapidity and the transverse momentum consecutively. These relative (L2) and absolute (L3) corrections are applied to correct for the variation in jet energy response in pseudorapidity and $p_{\mathrm{T}}$ [47, 48]. The factorized approach allows for the study and optimization of each correction separately. For the results shown in this thesis the corrections are applied to the uncorrected jet energy as illustrated in the Equation 3.3,

$$\text{Corrected Jet Energy} = (\text{Raw Jet Energy} - \text{offset}) \times C(rel : \eta) \times C(abs : p_T) \quad (3.3)$$

with $C(rel : \eta)$ and $C(abs : p_T)$ denoting respective correction factors. Jet energy corrections are derived from PYTHIA simulations. Jets reconstructed with particle flow utilizing heavy ion tracking require different corrections than those derived in pp at 7 TeV with pp tracking.

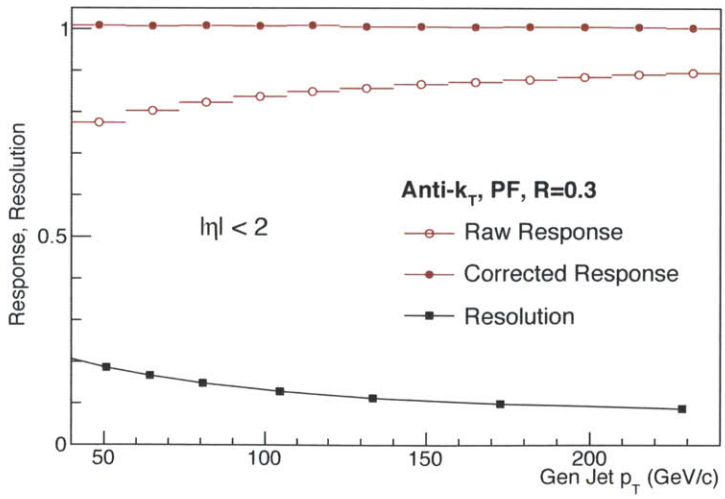


Figure 3-25: Raw response, corrected response and resolution for anti-$k_T$ PF jets using R=0.3, in (pp) PYTHIA simulations.

PYTHIA pp dijet events at 2.76 TeV are reconstructed with heavy ion tracking, anti-$k_T$ with resolution parameter of 0.3, and particle flow. As these are pure pp simulations, no pileup subtraction is used. Jet corrections are computed and applied using the standard JetMET energy correction framework. Figure 3-25 shows the jet energy before and after applying the computed corrections in pp. For the PbPb analysis we assume the background subtraction is factorized from the jet energy scale of the embedded jet. Thus these pp derived L2 and L3 corrections are applied to underlying event subtracted jets in PYTHIA+HYDJET simulations and data.

To validate the jet energy correction procedure the energy of the corrected, reconstructed jets are compared to the their matched generated jets. The mean of these distributions is found as the corrected jet energy scale, shown in the lower plots in Fig. 3-26. Jet energy scale from pp simulations are shown as closed circles, and from PbPb as open circles. The PYTHIA results are close to unity as expected. The jet energy scale for PbPb deviates from unity, and is included in the later systematic uncertainty.

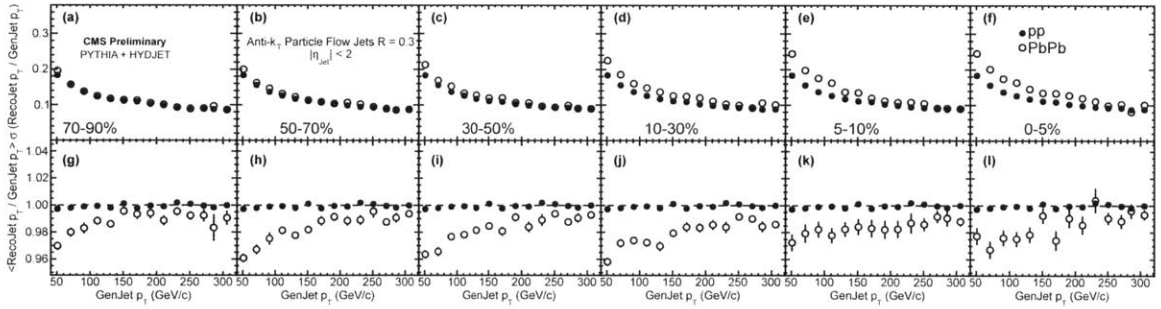


Figure 3-26: Jet $p_{\mathrm{T}}$ response and $p_{\mathrm{T}}$ resolution for anti-$k_{\mathrm{T}}$ jet algorithm with $R$=0.3 for pp (PYTHIA Z2) and different centralities in PbPb (PYTHIA Z2 + HYDJET 1.8). Different centralities are shown from left (peripheral) to right (central) for PbPb, with the pp simulations repeated in all centralities.

The upper parts of Fig. 3-26 show the jet $p_{\mathrm{T}}$ resolution, which is found from the width of the RecoJet/GenJet ratio distributions. In peripheral collisions, the PbPb resolution is similar to that of pp. However, in central collisions, the jet $p_{\mathrm{T}}$ resolution of PbPb simulations is worse at lower GenJet $p_{\mathrm{T}}$, and closer to pp at higher GenJet $p_{\mathrm{T}}$. As the effective jet radius increases (0.2 to 0.4) and the jet finder (even with pileup

subtraction) has the opportunity to pick up more background, the jet $p_{\mathrm{T}}$ resolution worsens for lower GenJet $p_{\mathrm{T}}$ values.

### 3.5.5 Jet Finding Efficiency

The jet finding efficiency and fake rate are studied with an inclusive jet selection within $|\eta| < 2$ in minimum bias HYDJET events. Reconstructed jets are matched to the corresponding generator jet position within $\Delta R(\sqrt{\Delta\phi^2 + \Delta\eta^2}) < 0.3$. The jet reconstruction efficiency is given as the fraction of reconstructed jets that have a matched GenJet for a particular GenJet $p_{\mathrm{T}}$, as shown in Fig. 3-27 (left).

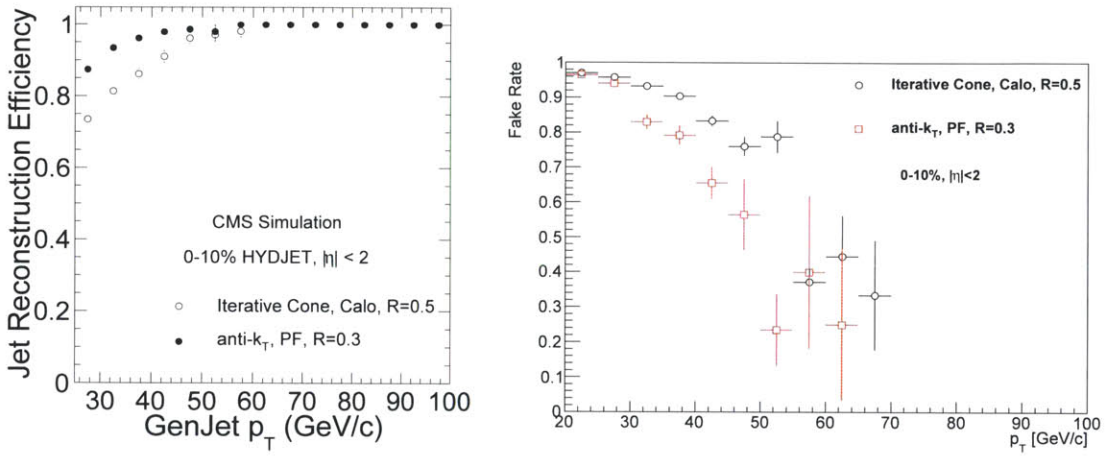


Figure 3-27: Left panel shows jet reconstruction efficiency (i.e., the fraction of genjets that have matched, reconstructed jets) in 10% most central HYDJET events. Right panel shows the fraction of inclusive fake jets in 10% most central HYDJET events.

Right panel of Figure 3-27 shows the fake jet fraction in the HYDJET sample for the 10% most central events. Fake jets are defined as reconstructed jets with no matching generated jet within $\Delta R < 0.3$.

## 3.6 Charged Particle Reconstruction

### 3.6.1 Tracking Algorithm

The heavy ion track reconstruction [49] is a modified version of the minimum bias pp tracking [50] algorithm with several parameters tuned to cope with high track density environment in PbPb collisions.

The charged particles are reconstructed in the following steps, which are similar to [7]. First, prior to track reconstruction, the three-dimensional primary vertex position is fitted from a collection of pixel-only tracks reconstructed with three hits in the pixel detector and extrapolated back to a region around the beam spot. Next, to reduce the random combinatorial background, track candidates are built from triplet seeds alone, consisting of hits in three layers of the pixel barrel and endcap detectors. The seeds from a restricted region within 2 mm of the primary vertex are constructed with a minimum $p_{\mathrm{T}}$ of 0.9 GeV/$c$. Further selections are made on the normalized goodness-of-fit (i.e. $\chi^2$) of the track fit and on the compatibility of the fitted triplet seeds with the primary vertex, before propagating the seed trajectories through the strip tracker to build fully reconstructed tracks. To improve the track reconstruction efficiency, two more iterations of the tracking are performed after removing hits unambiguously belonging to the tracks found in the first iteration. This procedure is based on the standard pp iterative tracking [51]. More efficient pp-based triplet-track and pixel-pair seedings are used in the second and third iterations, respectively. The tracks found in the later iterations are merged with the first-iteration tracks after removing any duplicate tracks, based on the fraction of shared hits. A notable difference compared to the tracking method described in Ref. [7] is the omission of the "calorimeter compatibility" requirement. This compatibility condition allowed the loosening of the track quality selection criteria by requiring a track-$p_{\mathrm{T}}$-proportional energy deposited in the closest ECAL and HCAL calorimeter cells. In the analyses presented in this document the track quality criteria are never loosened to keep a low fake track rate especially for tracks at $|\eta| > 1.4$. The minimal transverse momentum for tracks entering the analyses was set to 1 GeV/$c$.

In order to minimize the contribution of fake and non-primary tracks while maintaining relatively high efficiency in the highest track density environment, the following additional quality selections were applied to the tracks from the *HiGlobalPrimTrack* collection, a standard heavy-ion tracking collection:

- relative $p_T$ uncertainty below 5%: *trk.ptError()/trk.pt()*$< 0.05$
- at least 12 hits on the track: *trk.numberOfValidHits*$>= 12$
- relative impact parameter cuts: *abs(d0/d0err)*$< 3$ *AND abs(dz/dzerr)*$< 3$
- normalized $\chi^2$ per track layers with hit: *chi2n_par*$<= 0.4$,

where $d0$ and $dz$ refer to the impact parameter calculated with respect to the primary vertex, e.g., $trk.d0(vtx.position())$. Also, $d0err$ and $dzerr$ refer to the sums in quadrature of the transverse and longitudinal track impact parameter uncertainties and the respective uncertainties on the vertex position. Note that in the second and third iteration, a stricter requirement of 14 hits on the track was imposed because the higher iterations are more prone to fake tracks.

### 3.6.2 Tracking Performance

The study of the tracking performance is of primary importance for this analysis. The tracking performance was studied using jet events simulated with PYTHIA Z2 embedded into a HYDJET 1.8 background. The track-by-track corrections are computed in track $\eta$, track $p_{\mathrm{T}}$, neighboring jet $p_{\mathrm{T}}$ and event centrality bins without any selection criteria imposed on reconstructed jets.

The performance of tracking depends on the local environment in which the tracking operates. Therefore the tracking correction tables are computed for four centrality classes used in the analysis: 0-10%, 10-30%, 30-50% and 50-100%. The tracking efficiency (upper set of points) and the fake track rate (lower set of points) for the PYTHIA and for the four HYDJET-embedded PYTHIA centrality classes are shown in Fig. 3-28. At low $p_{\mathrm{T}}$ the efficiency is $\sim$8% higher for the PYTHIA sample than for the

HYDJET-embedded PYTHIA, while at high $p_{\mathrm{T}}$ the difference is about 2%. The fake rate is small for all samples, it ranges from 4% at 1 GeV/$c$ to 2% at 120 GeV/$c$.

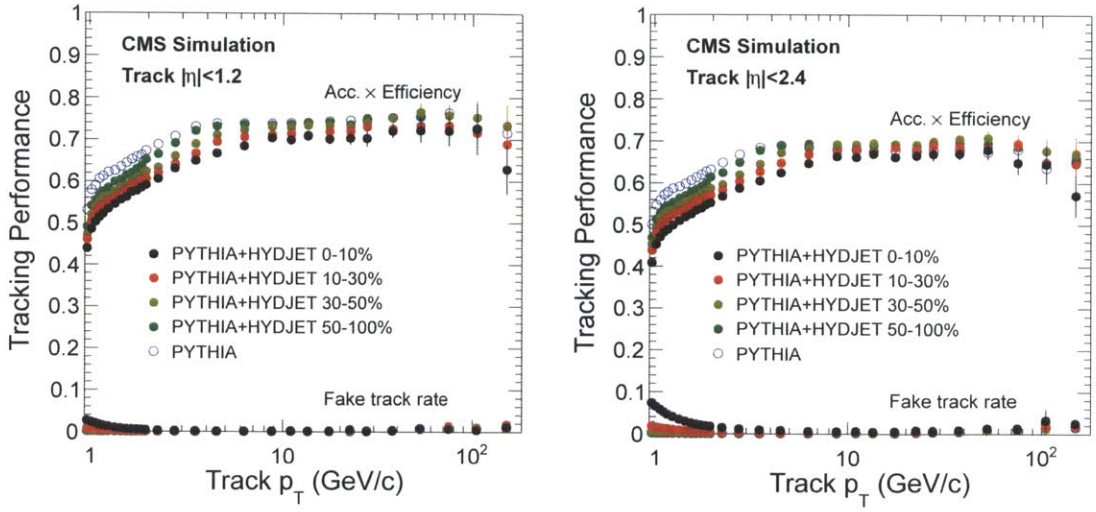


Figure 3-28: Tracking efficiency (upper set of points) and fake track rate (lower set of points) as a function of track $p_{\mathrm{T}}$ computed simulated samples. Left panel is for tracks in mid-rapidity, right panel is for tracks in the full tracker acceptance.

To understand the performance of tracking using the CMS tracker, it is important to note that the high granularity of the detector requires a high density of the on-detector electronics and cooling system. Fig. 3-29 shows the material budget of the tracker as a function of $\eta$. The presence of the material leads to multiple scattering, bremsstrahlung, photon conversion and nuclear interactions. These material related effects cause a relatively worsened tracking performance in the regions with greater material budget.

In order to test the precision of the track reconstruction procedure, various tests were performed. In these so called "closure" tests the fully corrected track distributions are compared to the generator level truth, and the agreement is evaluated. The closure test for the inclusive charged particle spectrum in $\hat{p}_{\mathrm{T}} > 80$ GeV/$c$ HYDJET-embedded PYTHIA events selected by the inclusive jet selection criteria is shown in Fig. 3-30. The generator level and the corrected reconstructed track level distributions agree within 2%. For tracks found within the jet cone the agreement is better than 5%.

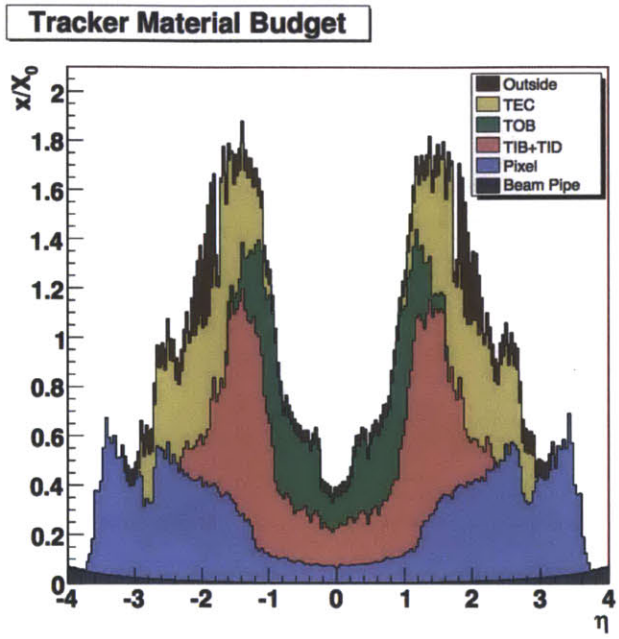


Figure 3-29: Material budget in units of radiation length as a function of pseudorapidity $\eta$.

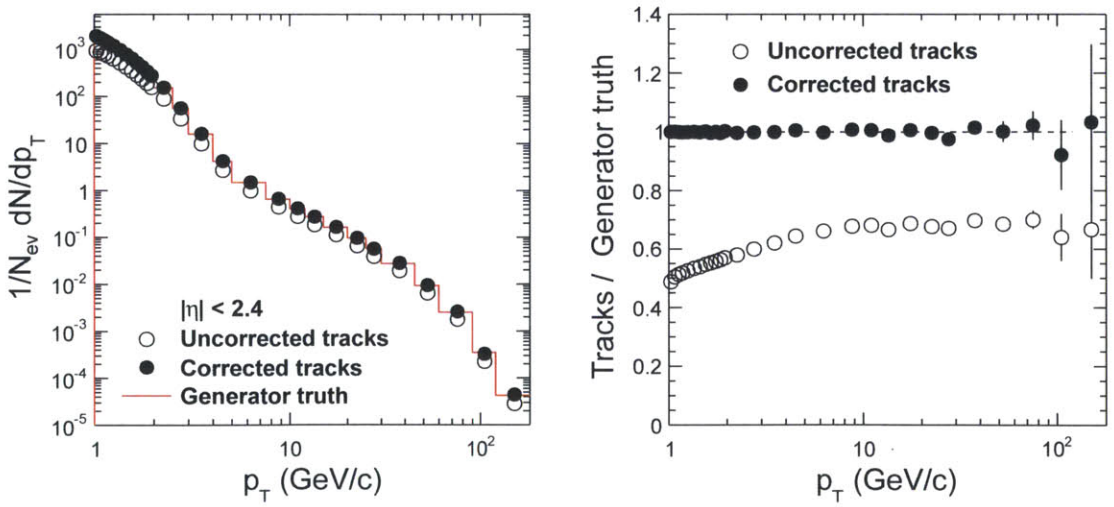


Figure 3-30: *Left:* the generator truth (red histogram), the raw reconstructed (circles), and the corrected reconstructed (dots) $p_{\mathrm{T}}$ distributions in the $\hat{p}_{\mathrm{T}} > 80$ GeV/$c$ HYDJET embedded PYTHIA sample. The events are selected according to the inclusive jet selection requirements. *Right:* the ratio of the reconstructed and the generator truth distributions.

### 3.6.3 Tracking Validation

Because the tracking efficiency correction used in this analysis is derived from the HYDJET Heavy Ion Monte Carlo (MC), it is important to check that track quality variables are similar in minimum bias data and simulation.

To demonstrate the validity of the quality cuts, we begin by examining the uncut *HiGlobalPrimTracks*. First, the number of valid hits on a track shown is in Fig. 3-31. We see that there is a peak around 17. This is expected for real tracks, because in CMS there are 3 pixel layers, 10 strip layers and 4 stereo layers. Thus we see that the peak around 17 valid hits corresponds to real tracks while the first peak corresponds to fake tracks. This observation is also confirmed by explicitly examining fake (unmatched) tracks in MC (Fig. 3-32). Thus we see that the number of valid hits on a tracks nicely separates real and fake tracks. We note that the minimum of this distribution is the same in data and MC, and this justifies our cut at 13.

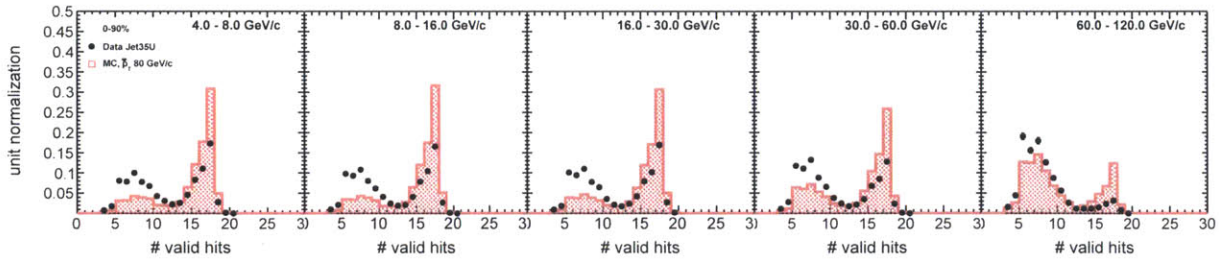


Figure 3-31: The distribution of number of valid hits ($N_{hits}$) for *HiGlobalPrimTracks* in data and MC, in different track $p_{\mathrm{T}}$ bins.

Given a minimum of 13 valid hits, we expect that the remaining tracks will have a much reduced fraction of fake tracks. We next look at the $\chi^2$ per tracker layer for tracks with nhit >= 13 cut. This is shown in Fig. 3-33. We see that real tracks have a peak around $\chi^2 = 0$. Also we see that the MC distribution nicely describes data.

After we require these two baseline cuts (minimum of 13 valid hits and a normalized $\chi^2$ per tracker layer less than 0.15), the remaining tracks contain a small fraction of fake tracks. We compare the remaining tracking quality variables after these two cuts to gain confidence that the efficiency we estimate in MC is applicable to data.

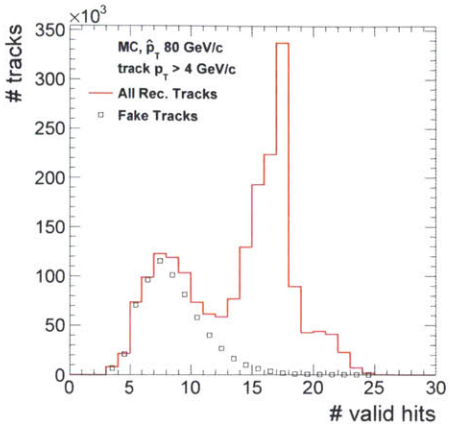


Figure 3-32: The distribution of number of valid hits ($N_{hits}$) for *HiGlobalPrimTracks* in MC comparing all reconstructed tracks with fake tracks. The tracks are from all centralities, with a leading jet $|\eta| < 2$ and $pT > 80GeV/c$.

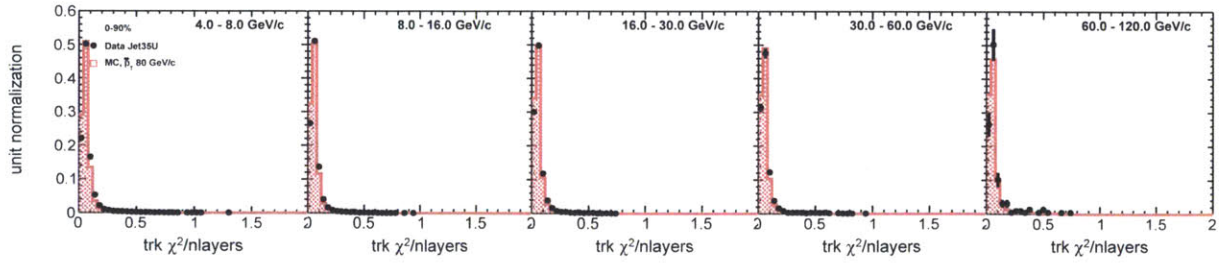


Figure 3-33: The distribution of $\chi^2$ per tracker layer for *HiGlobalPrimTracks* with 13 valid hits in data and MC, in different track $p_{\mathrm{T}}$ bins.

Figures 3-34-3-38 show data compared to MC distributions of the five track quality variables applied in the *HiGoodTightTracks* cuts for different $p_T$ ranges, inclusive in centrality. We see a good agreement between the data and the MC. Note that from the final track efficiency figures (Fig. 3-28), we expect the dependence on centrality to be small.

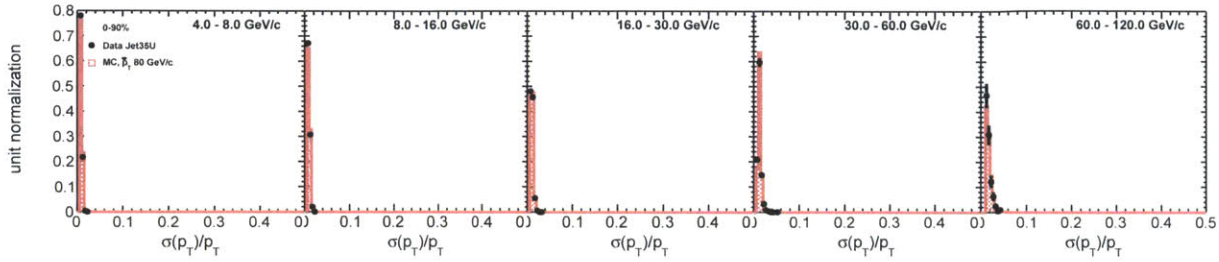


Figure 3-34: The distribution of relative $p_T$ uncertainty for *HiGlobalPrimTracks* given baseline cuts in data and MC, in different track $p_T$ bins.

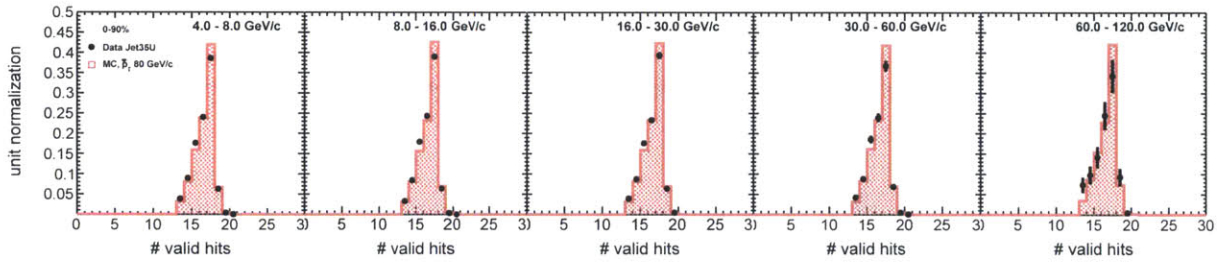


Figure 3-35: The distribution of number of valid hits on a track for *HiGlobalPrimTracks* given baseline cuts in data and MC, in different track $p_T$ bins.

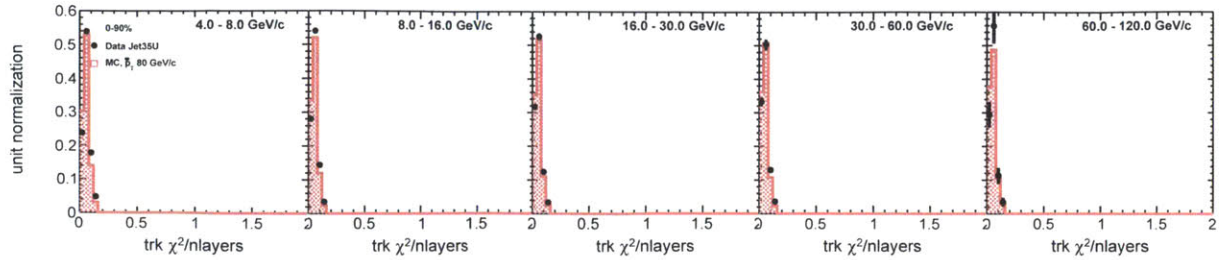


Figure 3-36: The distribution of normalized $\chi^2$ per tracker layer with hit on a track for *HiGlobalPrimTracks* given baseline cuts in data and MC, in different track $p_{\mathrm{T}}$ bins.

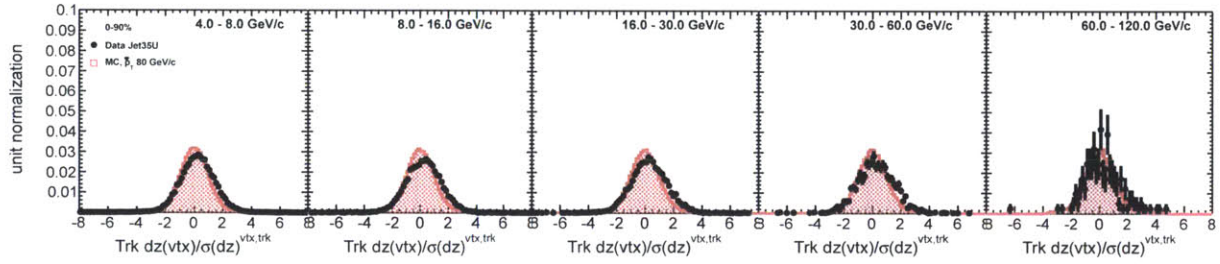


Figure 3-37: The distribution of relative impact parameter in the beam direction for *HiGlobalPrimTracks* given baseline cuts in data and MC, in different track $p_{\mathrm{T}}$ bins.

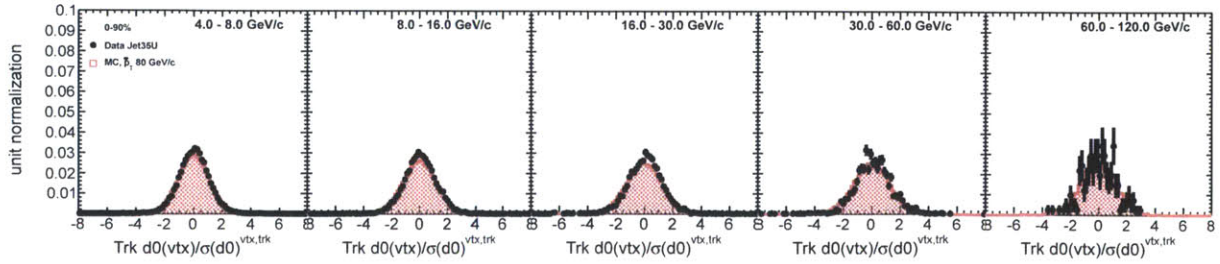


Figure 3-38: The distribution of relative impact parameter in the traverse plane for *HiGlobalPrimTracks* given baseline cuts in data and MC, in different track $p_{\mathrm{T}}$ bins.

# Chapter 4

# Jet Fragmentation Analysis

As discussed in Theory Sec. 2.3.2, colored partons propagating through QGP are expected to interact strongly with the QCD medium and lose energy. Since the decades that followed Bjorken's first proposal, experimental measurement of in-medium jet modification have today become a reality with the modern relativistic heavy ion colliders at Brookhaven (RHIC) and recently at CERN (LHC). In Chapter 3 basics of jet and charged particle reconstruction have been described. In this chapter, we now put the individual ingredients together and present the analysis of jet fragmentation measurement in PbPb and pp. The goal is to measure the distribution of particles which fragment from a jet in heavy ion collisions and to compare it to vacuum expectations.

Recall from Sec. 2.3.3 that most of the quenching models expect medium interactions to cause a softening of the jet fragmentation function. Before going to technical details of the analysis and the results, it is instructive to first examine the event display of a di-jet event in a central heavy ion collision. The $\eta, \phi$ unrolled calorimeter energy deposition in one such example event is shown in Fig. 4-1.

In Fig. 4-1, energy deposited in the calorimeter is plotted in the z axis versus $\eta, \phi$. Two jets can be clearly seen that stand above the underlying event background. These two jets form a di-jet pair because they are well back-to-back in $\phi$, as can be seen in the $r - \phi$ projection of the same event in the top panel of Fig. 4-2.

From the detector displays in Fig. 4-1 and Fig. 4-2, we see the di-jet pair has un-balanced momentum in the transverse plane. The highest $p_{\mathrm{T}}$ jet has $p_{\mathrm{T}} = 205$

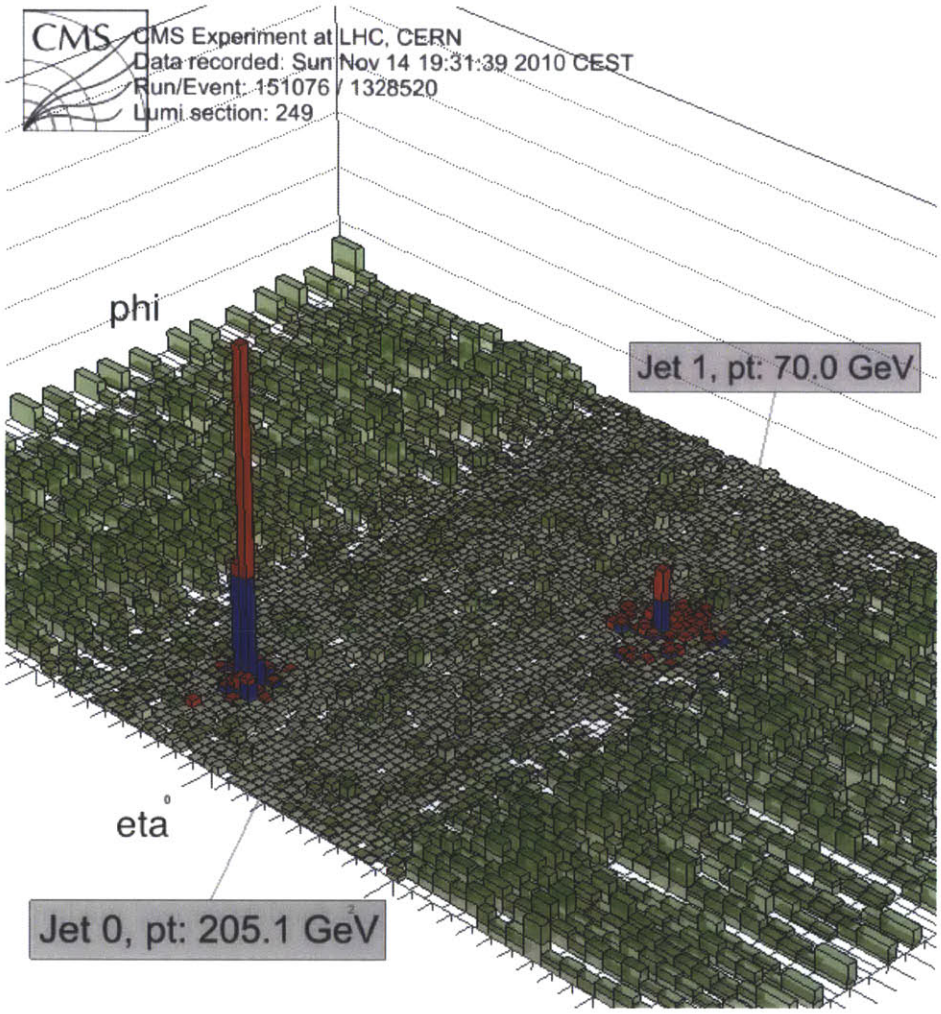


Figure 4-1: Example of an unbalanced dijet in a central PbPb collision event at $\sqrt{s_{NN}} = 2.76$ TeV. The summed transverse energy in the ECAL and HCAL calorimeters is plotted vs. $\eta$ and $\phi$. ($\eta$ is the longer edge of the rectangle in the plot) The HCAL and ECAL towers are selected with a minimum $p_{\mathrm{T}}$ selection at $\gtrsim 1$ GeV/c. The identified jets are highlighted and labeled with the corrected jet transverse momentum.

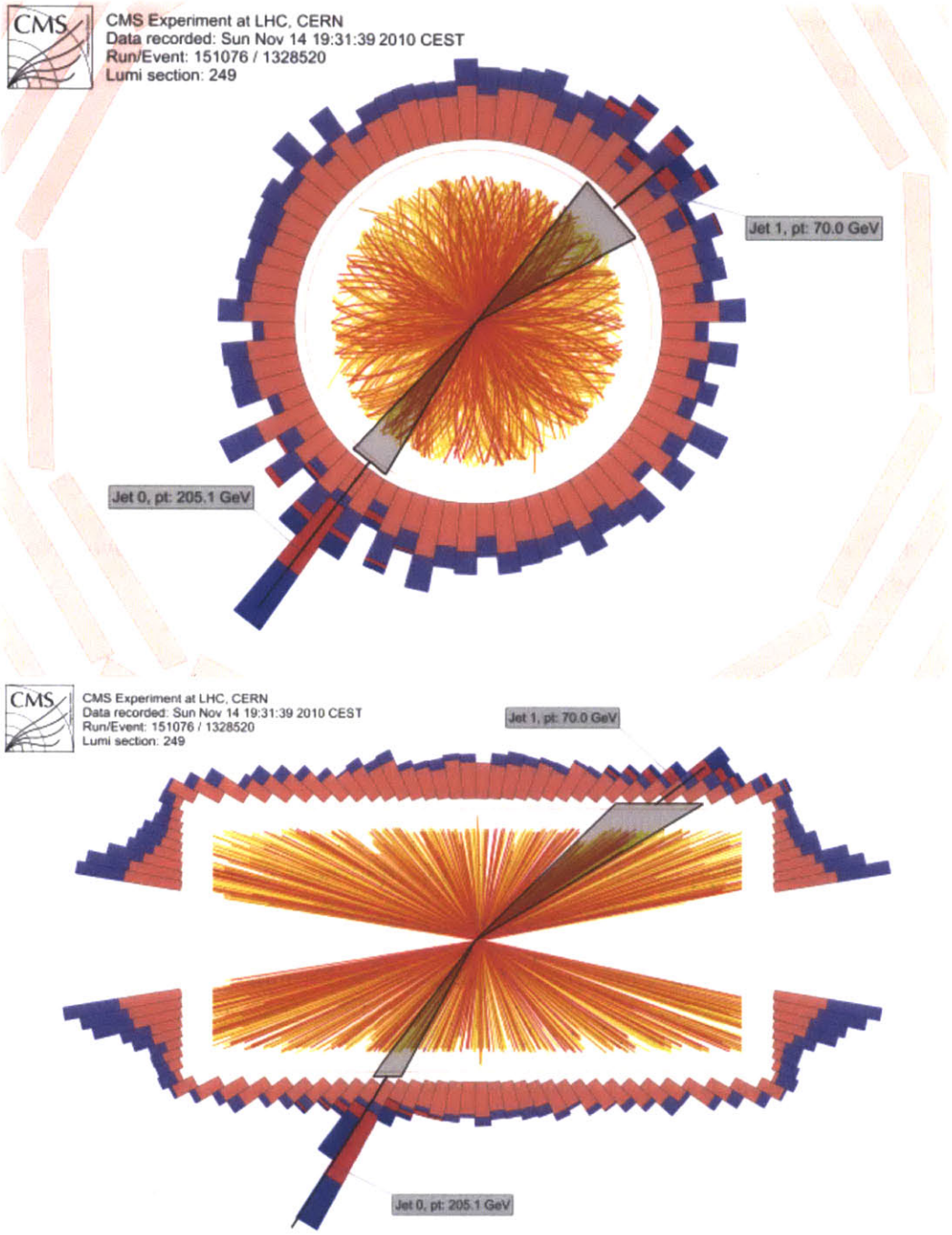


Figure 4-2: Same event as Fig. 4-1, but with different $r - \phi$ and $r - z$ projections of the detector including tracks. The height of the calorimeter cells represent the summed transverse energy in the electromagnetic and hadron calorimeters. The towers highlighted in blue and red show the towers in the jet region in Fig. 4-1.

GeV/c, while its partner has $p_{\mathrm{T}} = 70$ GeV/c. This is puzzling since from the $r - \phi$ event display, we know that the hard parton scattering is a 2 to 2 process. This is shown in a diagrammatic drawing of the event:

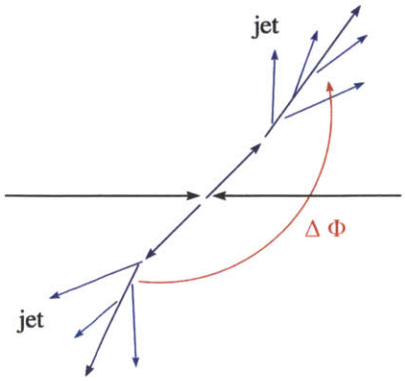


Figure 4-3: $r - \phi$ view of the hard scattering of the event display above. Note the out-going jets are back-to-back in $\phi$ (Figure from [23].)

Since the incoming beams have $\Sigma\vec{p_{\mathrm{T}}} = 0$, the outgoing hard scattered partons must also have $\Sigma\vec{p_{\mathrm{T}}} = 0$, due to momentum conservation. Thus the observed momentum imbalance is caused by interactions in the final state. We think this is due to energy loss of the partons within the dense QCD medium formed in the heavy ion collisions, as discussed in the Theory section 2.3.2. Since the hard scatterings occur randomly within the collisions volume, one parton has traversed a longer path than the other, thus losing more energy.

Now that we think the lower energy jet has undergone more medium interaction, we can visually compare the fragmentation patterns of the two jets. By inspection from Fig. 4-1, we see the lower $p_{\mathrm{T}}$ jet has relatively more low $p_{\mathrm{T}}$ particles as compared to its less modified partner. At the same time the fragmentation products appear to be more spread out forming a larger jet area. To compare these qualitative observations to theory, more quantitative analyses are needed. This forms the remaining content of this chapter.

One main challenge to the analysis is the high multiplicity environment as shown in the three event displays in Fig. 4-1 and Fig. 4-2. The jets are immersed in an

"underlying event" due to low $p_{\mathrm{T}}$ particle production coming from the heavy ion collision. These background particles are not produced by jet fragmentation and their effects need to be subtracted.

## 4.1 Analysis Overview

The main steps of the analysis can be summarized as follows:

1. Event selection.
2. Jet reconstruction and selection.
3. Track reconstruction and selection.
4. Construction of fragmentation function based on the reconstructed and selected jets and tracks.
5. Underlying event subtraction.
6. Construction of pp reference
7. Additional analysis level corrections.

The following sections will address each of the individual steps. Afterwards, systematic uncertainties of the measurement are estimated and justified.

## 4.2 Jet Fragmentation Function Observable

The theoretical definition of fragmentation function was given in the Sec. 2.2.2 by Eq. 2.1 and Eq. 2.2. Experimentally, jet fragmentation functions are measured by reconstructing charged-particle tracks that are contained within the parent jet cones. Due to inherent limitations of hadron collider experiments, the experimental definition of the fragmentation variable, $z$, varies slightly from the theory definition. This thesis follows the experimental definition as used previously at hadron colliders [52]. The fragmentation function is presented as a function of the variable

$$\xi = \ln \frac{1}{z} \; ; \quad z = \frac{p_{\parallel}^{\text{track}}}{p^{\text{jet}}}, \tag{4.1}$$

where $p_{\parallel}^{\text{track}}$ is the momentum component of the track along the jet axis, and $p^{\text{jet}}$ is the magnitude of the jet momentum. This definition differs from the theoretical definition in Sec. 2.2.2 by $O(\Delta R^2)$). The tracks in a cone of $\Delta R = \sqrt{(\Delta\phi)^2 + (\Delta\eta)^2} < 0.3$ around the jet axis are selected for analysis. The choice of using the variable $\xi = \ln(1/z)$ is motivated by anzats to the pQCD evolution equations as described in Sec. 2.2.3. The fragmentation function, defined as $1/N_{\text{jet}}\ dN_{\text{track}}/d\xi$, gives the expected number of final state fragmentation particles per jet at a given $\xi$. Note that here no particle identification is used, we are measuring the species inclusive fragmentation function.

## 4.3 Event Selections and Analysis Cuts

The starting point of the analysis is to select a set of jet candidate events for performing the fragmentation measurement. As described in Sec. 3.2, CMS uses a (two-level) trigger system for recording collision datasets. The main trigger used for the fragmentation analysis is HLT_HIJet80, which selects high momentum jet candidate events at the online level. This trigger uses fully reconstructed jets based on calorimeter information. The online threshold of 80 GeV/c is chosen such that it is fully efficient for jets with offline reconstructed and corrected $p_{\mathrm{T}}$ above 100 GeV/c (Sec. 3.2.1). Given the jet triggered dataset, the events are further filtered by a set of offline event selection criteria that result in a pure sample of true inelastic collisions events as described in Sec. 3.2.2. Finally the events are passed through an offline jet event pre-selection to select a subset of events that have at least one reconstructed calorimeter jet with $p_{\mathrm{T}} > 90$ GeV/c in the calorimeter barrel or endcap region ($|\eta| < 3$). This "skimming" step selects the highest momentum jets of interest and is intended to speed up the full analysis reconstruction that includes the iterative tracking (Sec. 3.6) and particle flow reconstruction (Sec. 3.5). This forms the set of events used for jet fragmentation analysis.

Given the events passing analysis event selection, particle flow jets are reconstructed with the anti-$k_T$ algorithm ($r = 0.3$, Sec. 3.5). All reconstructed jets with $100 < p_{\mathrm{T}} < 300$ GeV/c and $|\eta| < 2$ are considered for analysis. The choice of jet $|\eta| < 2$ is motivated by the fact that particle flow jets have best performance when the jet is completely within the tracker acceptance ($|\eta| < 2.4$). Jets with $p_{\mathrm{T}} > 100$ were chosen for the analysis because it is the lowest $p_{\mathrm{T}}$ where both jet reconstruction as well as the trigger are highly efficient (Fig. 3-27, Fig. 3-15). The offline event pre-selection of a calorimeter jet with $p_{\mathrm{T}} > 90$ GeV/c introduces a slight inefficiency at the analysis threshold of jet $p_{\mathrm{T}} > 100$ GeV/c. This is shown in Fig. 4-4. The inverse of the jet spectrum ratio of after/before the offline calorimeter jet skim (bottom row of Fig. 4-4) was used as reweighting factors to correct for this slight skimming inefficiency.

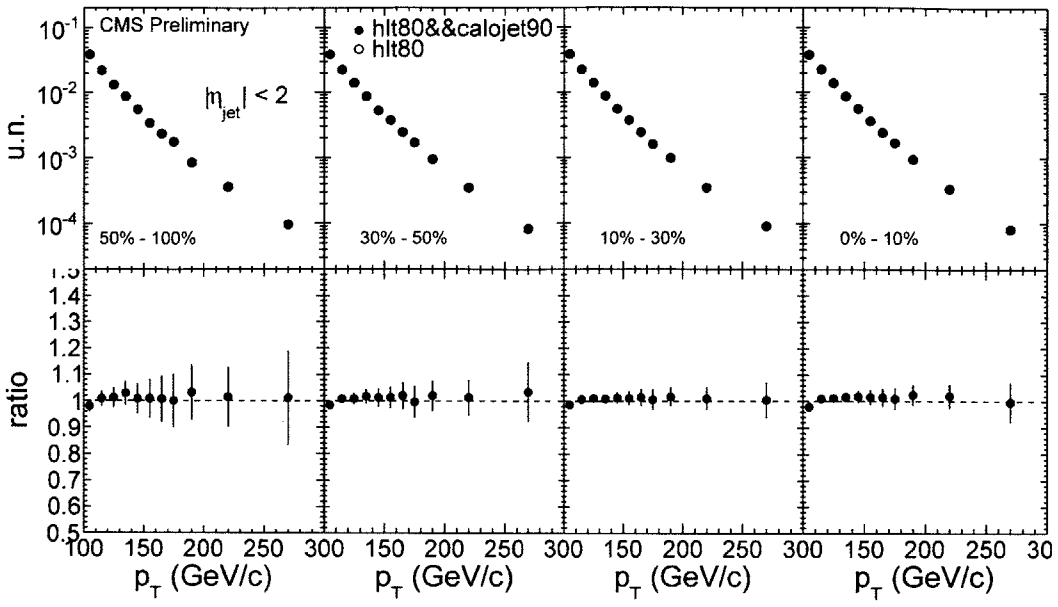


Figure 4-4: Comparison of jet spectra in in the jet triggered events before and after the calorimeter jet $p_T > 90$ GeV/c offline jet event pre-filtering in the analysis centrality bins. Top row shows the unity normalized jet spectra before and after the calorimeter jet event pre-filtering. Bottom row shows the ratio of the spectra.

Tracks are also reconstructed using iterative tracking (Sec. 3.6) for the selected analysis events. The reconstructed tracks are then further filtered by a set of track quality cuts to ensure a low fake rate and reasonably high tracking efficiency (Sec. 3.6.2). For the fragmentation analysis only tracks with $p_T > 1$ GeV/c and $|\eta| < 2.4$ are considered. This choice of track lower $p_T$ threshold at 1 GeV is because the tracking efficiency (Fig. 3-28) for iterative tracks drops very quickly below 1 GeV. $|\eta| < 2.4$ corresponds to the tracker acceptance.

## 4.4 Fragmentation Function Construction

Once the jets and tracks are reconstructed and selected in the analysis events, the fragmentation function can be constructed for $p_T > 100$ GeV/c jets. Tracks contained within the jet cones at $\Delta R < 0.3$ are selected for the fragmentation measurement. For each particle the quantity $\xi$ (Equ. 4.1), is calculated and entered into a histogram. Each track is entered with a weight that is the result of the tracking efficiency and fake rate correction. The histogram is then normalized by the number of selected jets (Sec. 4.2). The resulting histogram is the $1/N_{\rm jet}\ dN_{\rm track}/d\xi$ distribution. The raw fragmentation functions are shown as open circles in the left of Fig. 4-5 and 4-6 for the different analysis centrality bins.

The integral of the $\xi$ histogram is just the average number of (charged) particles per jet that are in the jet cone at $\Delta R < 0.3$. The jet $p_T$ distributions of the selected jets are also shown in the figures. Notice the general hump-back shape of the fragmentation distribution in $\xi$ as discussed in Sec. 2.2.3.

Note that the fragmentation function decreases sharply at $\xi \sim 4.6$, in contrast to the gradual decrease as seen in Fig. 2-11. This sharp fall off is due to the kinematic thresholds of the analysis at jet $p_T > 100$ GeV/c and track $p_T > 1$ GeV/c, which translates to $\xi \approx \ln(100/1) = 4.6$. Another useful number to build some intuition in reading the plot is that for a jet with $p_T$ =100 GeV/c, $\xi = 1$ approximately corresponds to tracks of $p_T \approx 100/e^{1.} = 37$ GeV/c.

For the central events in Fig. 4-5 there is a high number of tracks that are contained within the jet cone at low $p_T$ around the analysis threshold of track $p_T > 1$ GeV/c, $\xi \sim 4.6$ reflecting the high multiplicity environment. The contribution from the uncorrelated heavy ion background results in a bump shape at $\xi \sim 4.6$. The low $p_T$ tracks are particles produced by the underlying heavy ion collision that are within the jet cone. These particles are not associated with jet fragmentation and need to be corrected for.

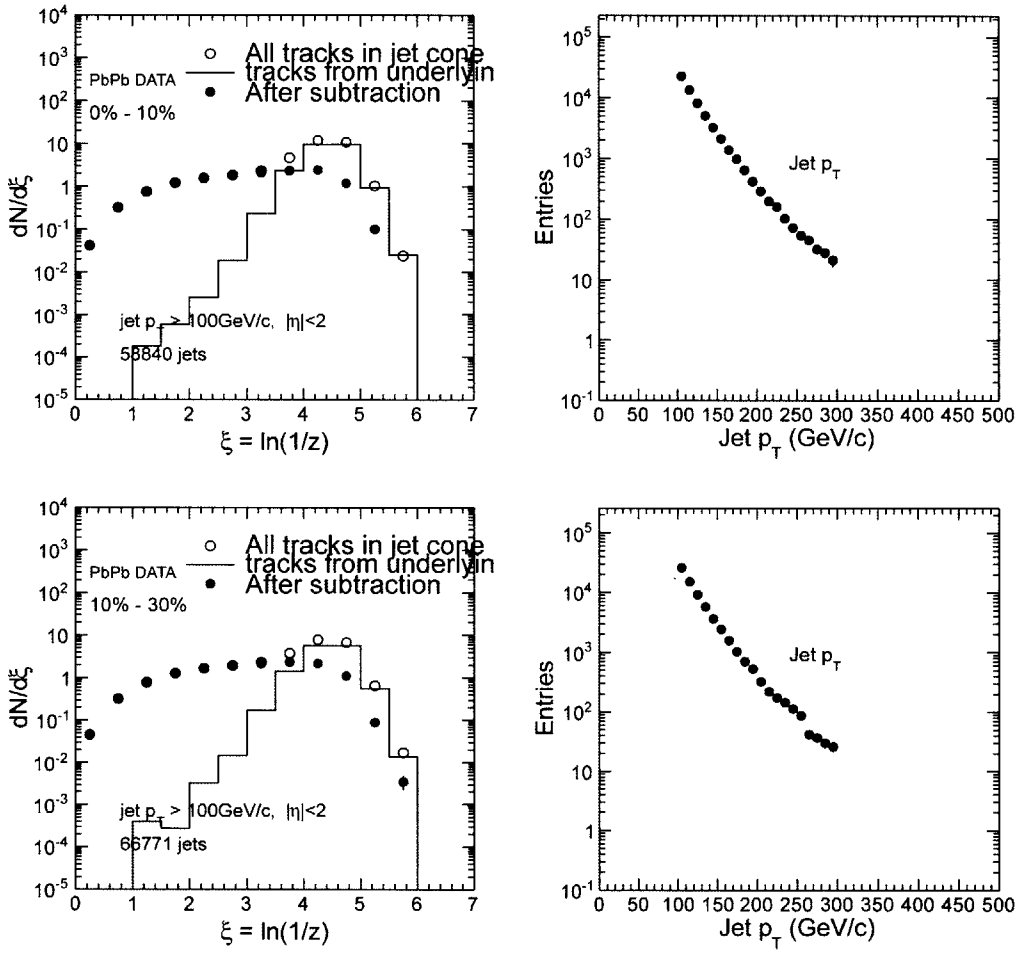


Figure 4-5: Fragmentation function calculation in the two top analysis centrality bins (0-10% and 10-30%). Right is the spectra of jet transverse momentum. Background was estimated from $\eta$ reflection method.

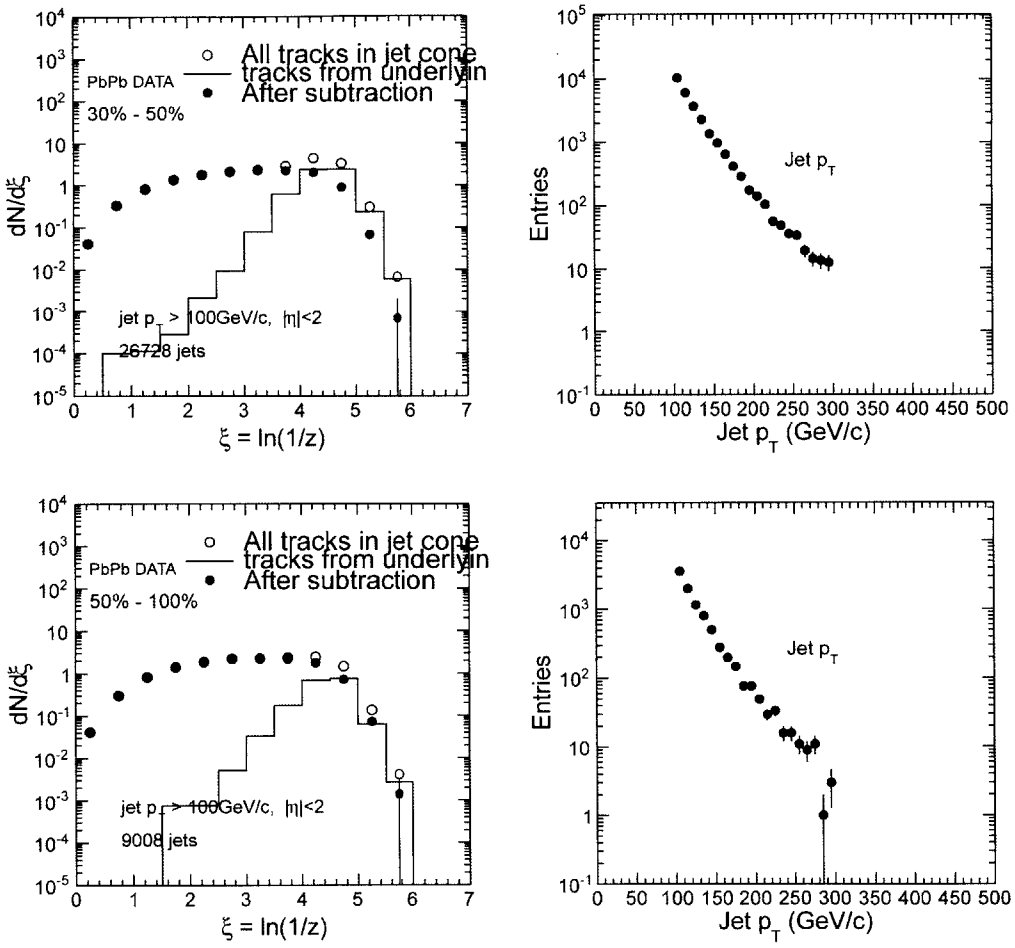


Figure 4-6: Fragmentation function calculation for the two peripheral analysis centrality bins (30-50% and 50-100%). Right is the spectra of jet transverse momentum. Background was estimated from $\eta$ reflection method.

## 4.5 Underlying Event Background Subtraction

As discussed above, due to the high level of underlying event activity coming from the heavy-ion collisions, tracks that are not associated with the jet fragmentation can be included in the jet cone. Experimentally we cannot distinguish which tracks are from the heavy ion event and which tracks are from jet fragmentation. Instead the uncorrelated background contribution is subtracted statistically in the $\xi$ distribution. A method called the $\eta$-reflection method is used in this analysis.

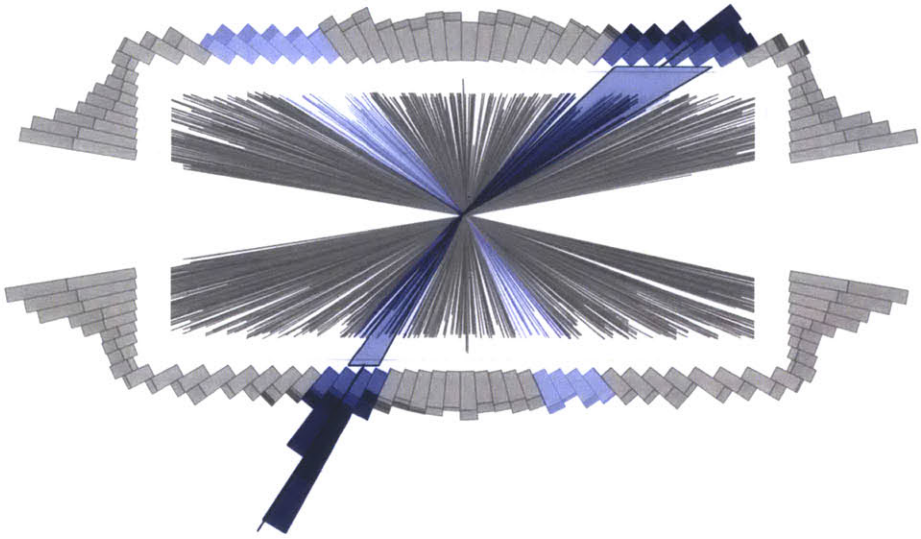

Figure 4-7: Same $r-z$ view of the detector as in Fig. 4-2, but with the jet regions (dark blue) and $\eta$ reflected regions (faint blue) highlighted.

The underlying event contribution that is not associated with the hard interaction, is estimated by selecting charged particles that lie in a background jet cone obtained by reflecting the original jet cone around $\eta = 0$ while keeping the same $\phi$ coordinate. The motivation for this approach can be illustrated by looking at the event display in Fig. 4-7. The figure is the same as the bottom panel of Fig. 4-2, except it is highlighted to emphasize the jet region (dark blue) in contrast to the underlying heavy ion event (gray). From this $r-z$ view of the heavy ion event, it can be seen that the underlying event is $\eta$ symmetric around the collision point. This is expected since the incoming

beams are $z$ symmetric. Not only so, we know from studies of azimuthal anisotropy of charged particles at high $p_{\mathrm{T}}$ that the correlation function between a high $p_{\mathrm{T}}$ particle and another particle in $\Delta\eta$ is symmetric [53]. Thus the reflected $\eta$ region is a good control region to estimate the background distributions in the jet region.

To estimate the background particle distribution within the jet cone, for each signal jet, a separate $\xi$ histogram is filled using the jet $p_{\mathrm{T}}$ and particles in the reflected jet cone just as what was done in the signal cone. It is then also normalized to the number of selected jets. The background distribution is subtracted from the raw $\xi$ distribution obtained from the signal jet cone. Assuming the average background is perfectly $\eta$ symmetric, what then remains is just the $\xi$ distribution from the jet fragmentation alone.

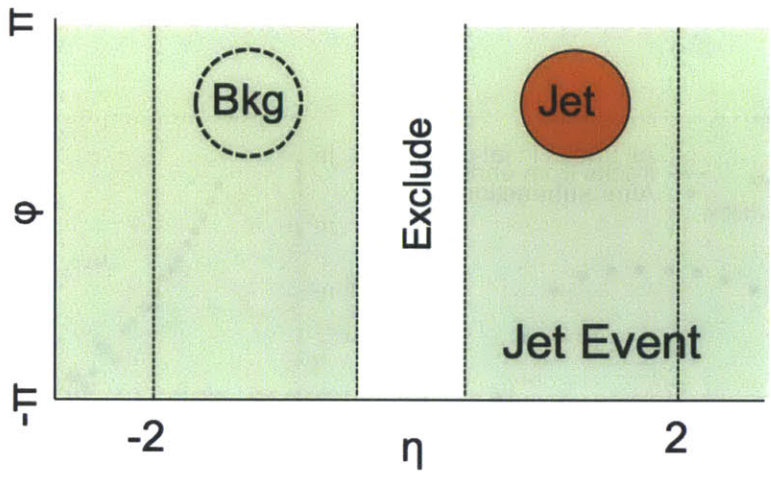


Figure 4-8: Diagram of the analysis regions for the jets cones, background cones, and excluded jets.

For this procedure, jets in the region $|\eta|$ <0.3 are excluded to avoid overlap between the signal jet region and the region used for background estimation. The different analysis regions are summarized in the diagram in Fig. 4-8. The estimated background contribution to the fragmentation function using the $\eta$ reflection method are shown as the black histogram line in Fig. 4-5 and 4-6. And the background subtracted distributions are shown in the figures as solid plot dots.

## 4.6 Constructing pp Reference

In order to quantify the medium-related effects, the results are compared to the reference jet fragmentation function based on pp data. The dataset used for this reference analysis was from pp collisions at the same per nucleon collision energy, $\sqrt{s_{NN}} = 2.76$ TeV, as the heavy ion data. The events were collected with a jet trigger having threshold of $p_{\mathrm{T}} > 60$ GeV/c based on jets reconstructed from the calorimeter information. Offline event selection procedure similar to the heavy ion analysis was applied to obtain a pure set of pp inelastic collision events. For the pp events, jets and tracks were reconstructed with the same reconstruction algorithms as in the heavy ion analysis. The same analysis thresholds were applied and the fragmentation analysis was repeated as in heavy ion data. The raw pp jet fragmentation function is shown in Fig. 4-9.

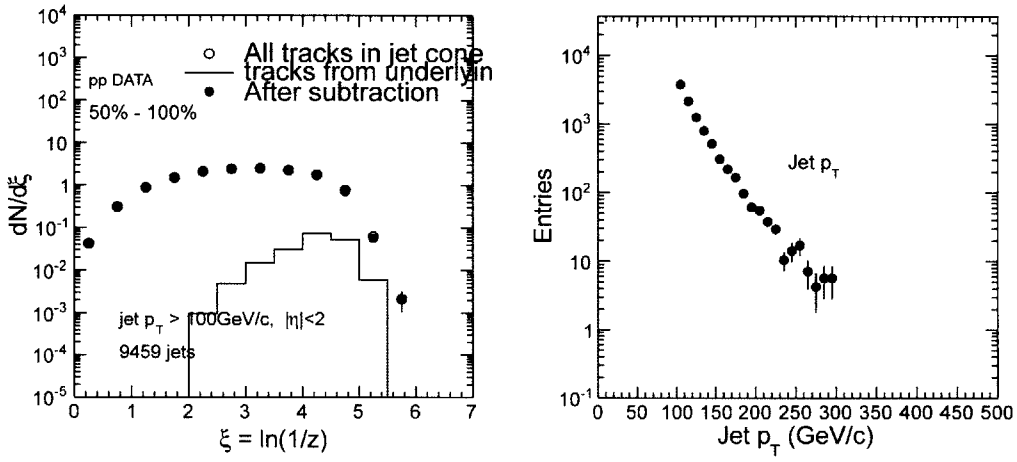


Figure 4-9: Fragmentation function calculation for the pp analysis. Right is the spectra of jet transverse momentum. Background was estimated from $\eta$ method. (disregard the centrality label in the left plot)

For a proper comparison between pp and PbPb collisions, the jet momentum resolution deterioration in PbPb events has to be taken into account. The jet energy resolution in PbPb and pp was discussed in section 3.5.4, and shown in Fig. 3-26. For analysis usage, the jet energy scales and resolutions were parametrized as a function of jet $p_{\mathrm{T}}$ for the four analysis centrality bins in PbPb and in pp. These are

shown in Fig. 4-10. The figure shows the jet energy scale and jet energy resolution parametrization for PYTHIA di-jet events (blue) and also PYTHIA di-jet events embedded into simulated HYDJET heavy ion events (red).

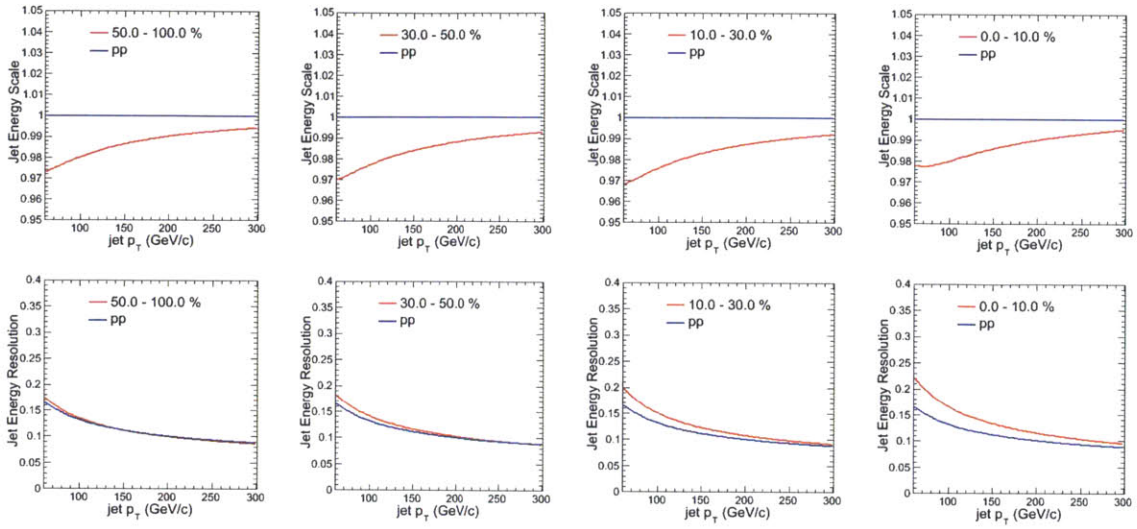


Figure 4-10: Parametrization of jet energy scale (top) and resolution (bottom) using PYTHIA+HYDJET events.

From the direct overlay of the jet energy resolutions (bottom, Fig. 4-10), we see in peripheral PbPb events, the jet energy resolution in PbPb is comparable to pp. However, as the centrality increases, the PbPb jet energy resolution becomes increasingly worse than pp.

To treat the difference in jet energy resolution in the PbPb and pp jets, one may directly unfold the jet energy used in the $\xi$ distributions given the response matrix. However, because jet energy only enters the fragmentation analysis as a higher order effect, we choose to simply smear the pp jets to match the PbPb jet resolution. For each jet in pp data, the reconstructed $p_{\mathrm{T}}$ is smeared by the quadratic difference of the jet resolution in PbPb and pp as shown in Fig. 4-10. To be precise, for each pp jet, a random number was drawn from a Gaussian distribution with a mean of 1 and width of $\sigma_{diff} = \sqrt{\sigma^2_{PbPb} - \sigma^2_{pp}}$, where $\sigma_{PbPb}$ and $\sigma_{pp}$ are the PbPb and pp jet energy resolutions respectively. The smeared jet $p_{\mathrm{T}}$ distribution in PYTHIA is shown in Fig. 4-11 and overlaid with the PYTHIA+HYDJET to show that smearing allows the

pp distribution to better match with with PbPb. The data is shown in Fig. 4-12.

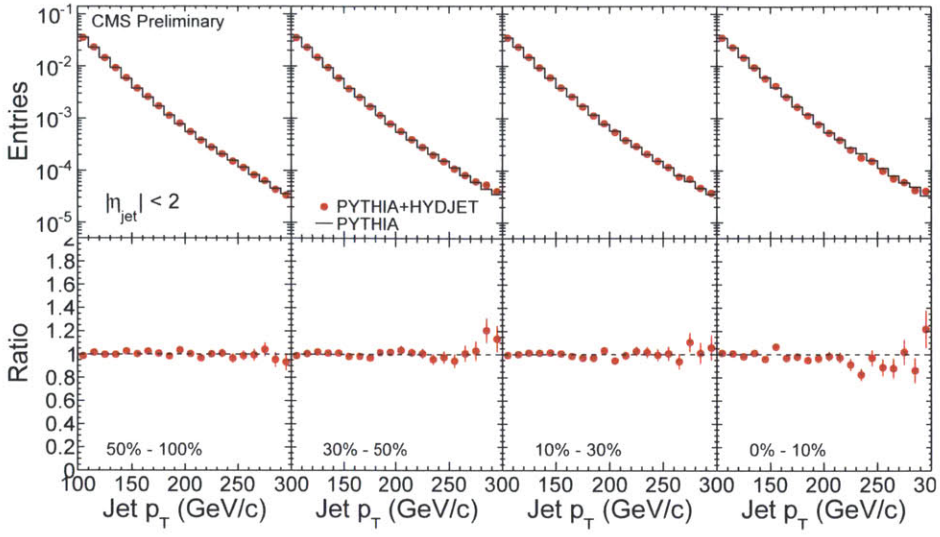


Figure 4-11: Top row shows jet $p_{\mathrm{T}}$ distributions in PYTHIA+HYDJET (red dot) compared to the jet $p_{\mathrm{T}}$ distributions in smeared PYTHIA. The bottom shows the ratio of the distributions of PbPb/pp.

Fig. 4-12 shows the smeared pp jet distributions from pp data in comparison with the jet $p_{\mathrm{T}}$ distribution in PbPb data. In contrast to MC, even after the pp smearing the jet $p_{\mathrm{T}}$ distribution in PbPb is still different than that of pp. This effect is not an occupancy related effect, since we see that even given the increasing multiplicity background in the MC analysis, the PbPb jet $p_{\mathrm{T}}$ distribution was similar to pp in all centralities in PbPb MC. Thus the difference in the jet $p_{\mathrm{T}}$ distribution is like to by caused by real physics.

The physics of the jet $p_{\mathrm{T}}$ distribution in PbPb is not the goal of this analysis. What concerns the jet fragmentation analysis is to keep the jet kinematic constraints consistent in the PbPb to pp comparison. That is, we want to compare the fragmentation function of PbPb jets at the same jet energy as the pp jets so that the exact shape of the jet $p_{\mathrm{T}}$ distribution factorized out of the analysis. The inverse of the PbPb/pp ratio in the bottom of Fig. 4-12 is applied as a re-weighting factor to the smeared pp data, such that the resulting pp jet $p_{\mathrm{T}}$ distribution matches the one in PbPb in each centrality bin of the analysis. To be precise, the re-weighting factor is applied to each jet as a function of jet $p_{\mathrm{T}}$ and analysis centrality bin when generating

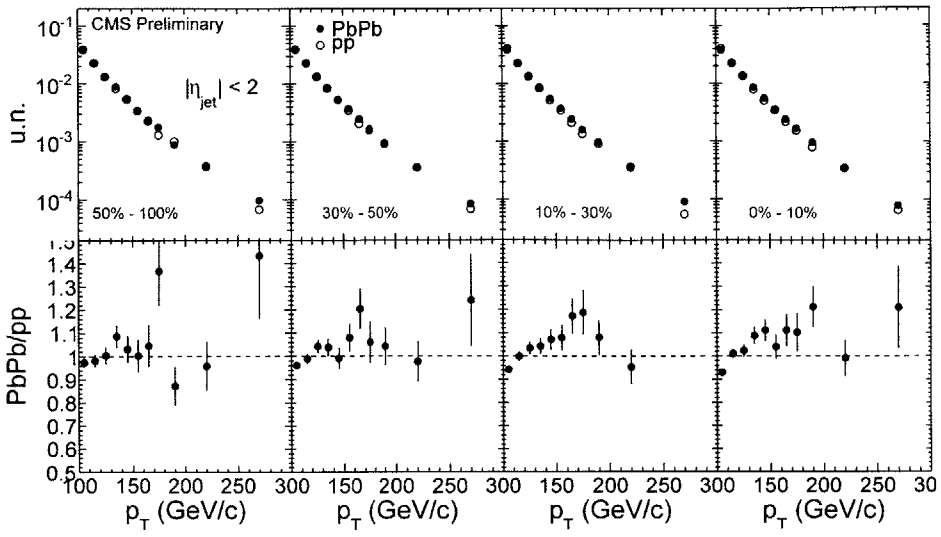


Figure 4-12: Comparison of jet spectra in PbPb data and the smeared pp data is shown in the top row. The bottom plots are the ratios of PbPb to pp, which are used as the re-weighting factor in the analysis.

the corresponding fragmentation function reference distributions for pp.

## 4.7 Additional Analysis Corrections

Given the reconstructed jets, tracks, tracking efficiency correction, background contribution subtraction we have constructed the fragmentation functions for both PbPb in the previous sections. We have also constructed a pp reference by repeating the same analysis on pp data except in addition smearing and re-weighting the jet $p_{\mathrm{T}}$. The physics message may now be obtained by taking the ratio of the fragmentation function in PbPb and pp. However, before we look at the results in data, one may first test the analysis for simulated Monte Calo events. The full reconstruction chain is completed for PYTHIA+HYDJET events and we treat it as the PbPb data. Similarly, the full reconstruction chain is completed for PYTHIA events and we treat it as pp data.This is shown in Fig. 4-13. The systematic uncertainly (yellow) band will be explained in later part of the chapter.

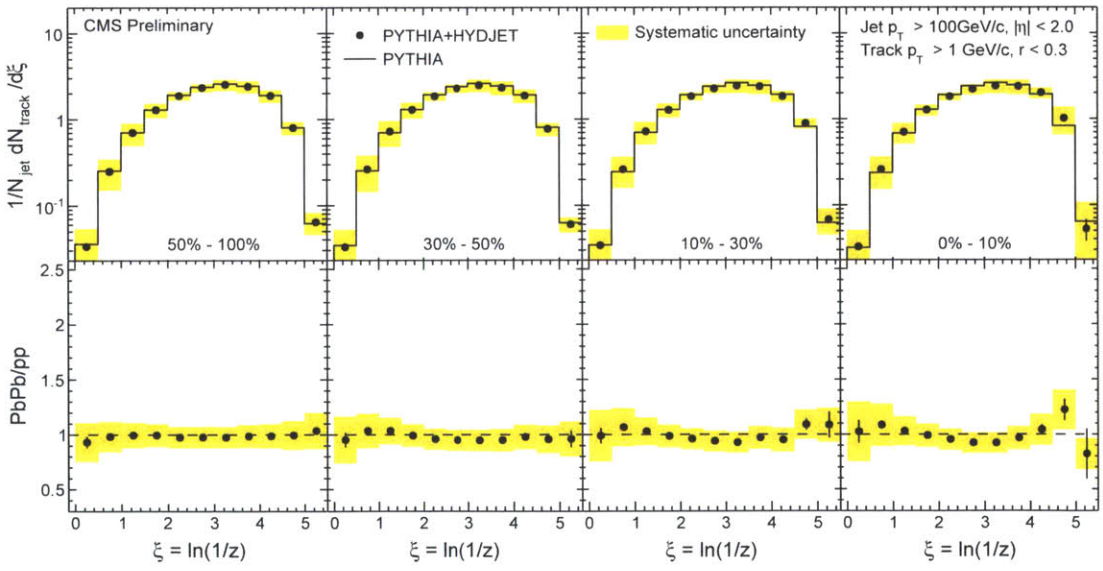


Figure 4-13: Fragmentation function analysis for reconstructed Monte Carlo events. The yellow band represents the estimated analysis systematic error band applied to the MC as if it were data.

Further information can be gained by looking at the explicit $p_{\mathrm{T}}$ distribution of the fragmentation particles. This is shown in Fig. 4-14.

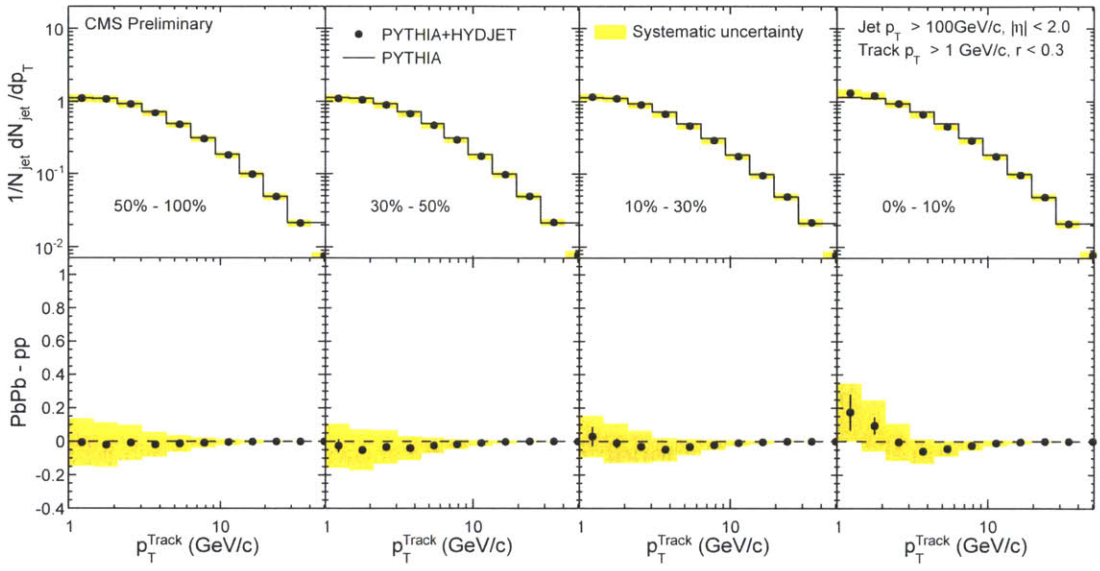


Figure 4-14: Fragmentation track $p_{\mathrm{T}}$ analysis for reconstructed Monte Carlo events. The yellow band represents the estimated analysis systematic error band applied to the MC as if it were data.

### 4.7.1 Biases in Fragmentation Function Introduced by Reconstruction

The same jet physics is contained in the embedded PYTHIA events as the standalone PYTHIA events, and we expect that after all analysis, the reconstructed ratio of fragmentation function in the PbPb/pp MC will be unity. But in Fig. 4-13 and Fig. 4-14, we see that the reconstructed ratio is in fact not at 1, but it shows systematic deviations. Two main features can be seen in the MC analysis:

1. A *centrality dependent* excess in the low $p_{\mathrm{T}}$ part of the fragmentation function ratio, for $\xi \gtrsim 4$ (bottom, Fig. 4-13) and correspondingly for track $p_{\mathrm{T}} \lesssim 3$ (bottom, Fig. 4-14). This biases the PbPb fragmentation to be softer than the pp reference at low track $p_{\mathrm{T}}$.

2. A downward slope in the $\xi$ ratio between $0 \lesssim \xi \lesssim 4$ can be seen. (bottom, Fig. 4-13). It biases the PbPb fragmentation function to be harder compared to the pp reference. Correspondingly this slope shows up as an upward slope in the mid-$p_{\mathrm{T}}$ to high $p_{\mathrm{T}}$ part of the track $p_{\mathrm{T}}$ analysis. (bottom, Fig. 4-14).

The centrality dependent deviation of fragmentation function in PbPb MC from the pp MC is artificially introduced by the reconstruction. We need to include additional corrections to remove the reconstruction biases to the measured fragmentation functions.

### 4.7.2 Understanding the Biases

To understand the biases of the fragmentation function introduced by the reconstruction, we can trace back the reconstruction chain step by step back to the generated event, since the analysis is completely in Monte Carlo. In particular we may disentangle effects of tracking reconstruction from the effect of jet reconstruction.

### Background fluctuation Bias

The first thing we can do is to repeat the analysis using all generated charged particles instead of reconstructed tracks. We reconstruct jets as before, but take all generated charged particles in the jet cone to construct the raw fragmentation function. Then we construct the background distribution using generated charged particles in the $\eta$ reflected cone. This is shown in Fig. 4-15 for the $\xi$ analysis and in Fig. 4-16 for the track $p_{\mathrm{T}}$ analysis.

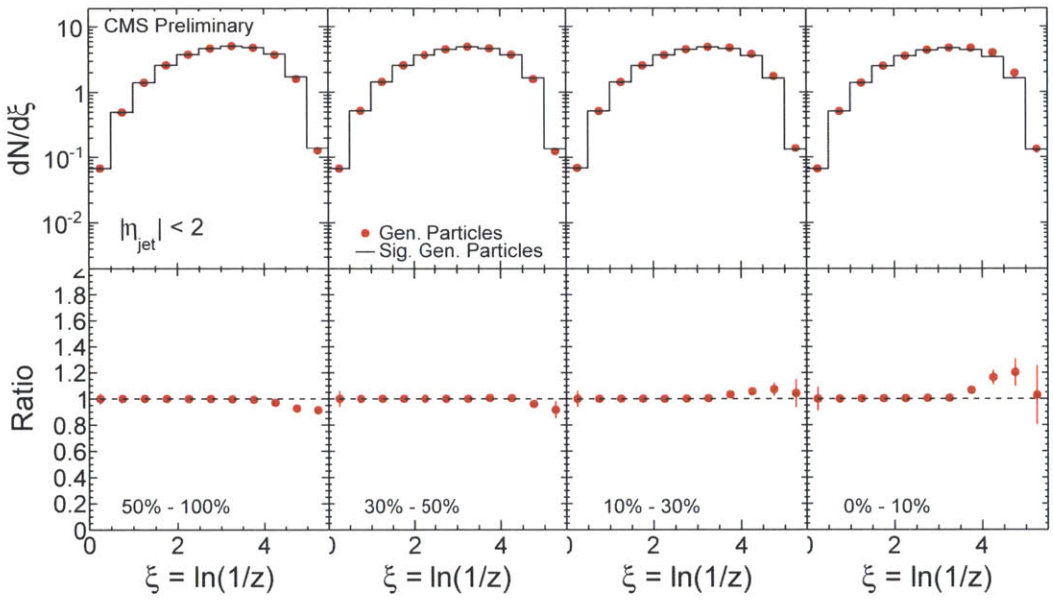


Figure 4-15: Generator particle level background subtraction for the $\xi$ analysis.

From Fig. 4-15 and Fig. 4-16 we see that the background subtraction using the $\eta$ reflection method works well for high $p_{\mathrm{T}}$ tracks but does not fully subtract the low $p_{\mathrm{T}}$ tracks. This means that the excess we observed at low track $p_{\mathrm{T}}$ in the full reconstruction analysis is unrelated to tracking reconstruction but related to the background estimation procedure. But we know that the HYDJET background is $\eta$ symmetric so how can the $\eta$ reflection method under-estimate the background under the jet cone? Apparently the background under the jet cone is biased to be higher than the average HYDJET background which is approximated by the reflected cones. We can tell that this effect is related to the multiplicity of the events since the bias increases as a

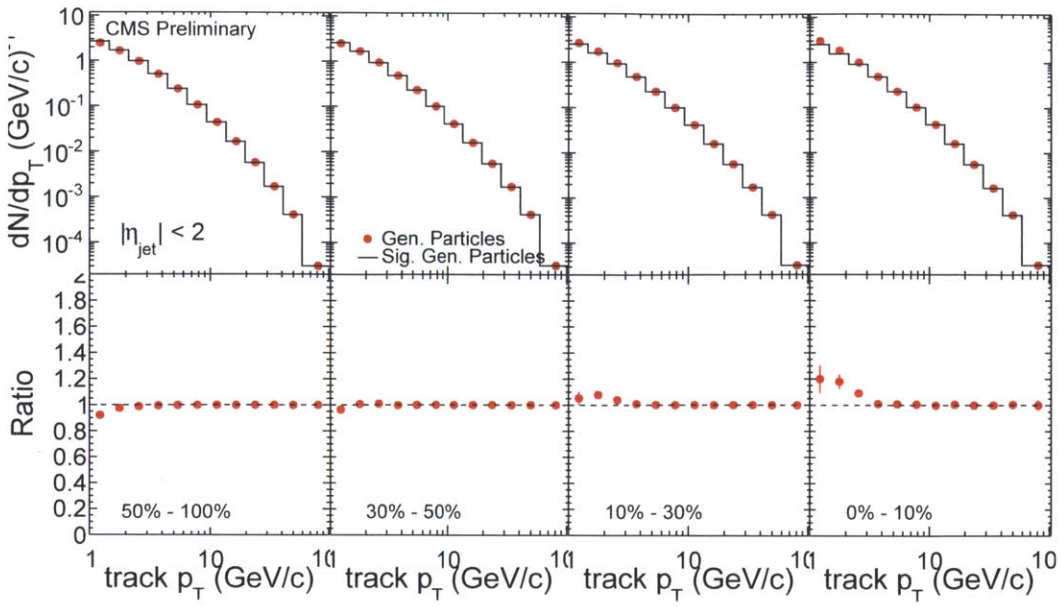


Figure 4-16: Generator level particle background subtraction for the track $p_{\mathrm{T}}$ analysis.

function of centrality.

If tracking reconstruction is not causing the bias, then the bias is introduced by the jet reconstruction. We know that the jets are embedded at random positions in the heavy ion event. Assuming the bias is related to jet reconstruction then if we use the generated jets instead of reconstructed jets then we expect the bias should then go away. In fact we can even take an intermediate step where we still use reconstructed jets but require that they have the corresponding generator level jet to have $p_{\mathrm{T}}$ above the analysis threshold of 100 GeV/c. This is shown in Fig. 4-17 and Fig. 4-18.

Once we require the reconstructed jets to have corresponding generator level jet with $p_{\mathrm{T}}$ above the analysis jet threshold, then the background subtraction works well. This means that the bias in the fragmentation function at low track $p_{\mathrm{T}}$ is really coming from jets which have true $p_{\mathrm{T}}$ below the 100 GeV/c analysis threshold but were reconstructed with $p_{\mathrm{T}}$ above the 100 GeV/c threshold. This is a result of the worsened jet energy resolution due to the fluctuations in the underlying event. These jets have true $p_{\mathrm{T}}$ below 100 GeV/c but sit on top of an upward fluctuation in the underlying event, and thus are reconstructed at higher jet energy. Due to the steeply falling jet $p_{\mathrm{T}}$ distribution, these jets with over-estimated energy cross the analysis jet

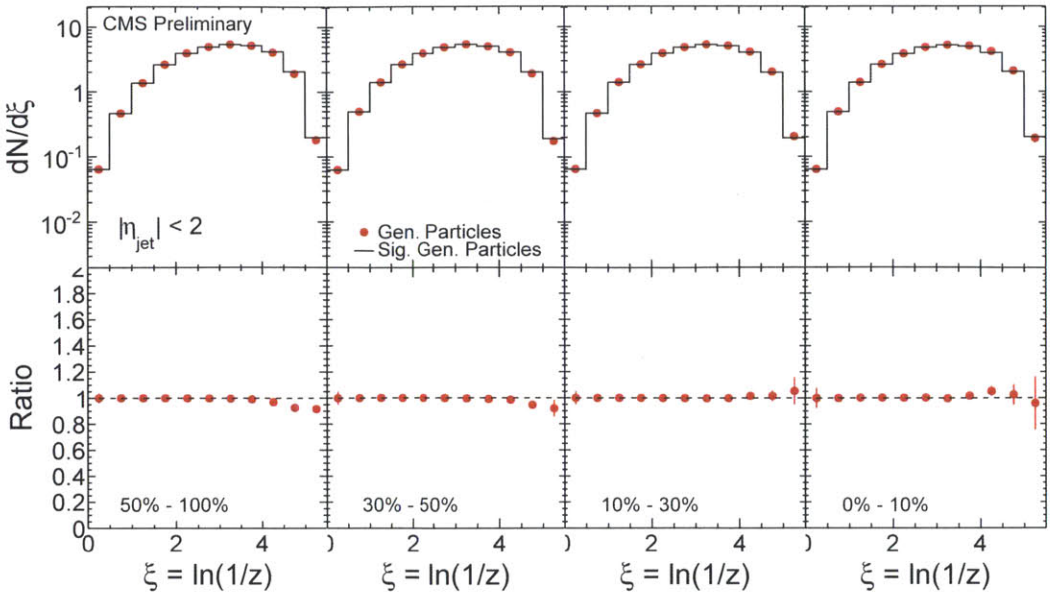


Figure 4-17: Generator level particle background subtraction for $\xi$ analysis after require additionally that the reconstructed jets have genjet $p_{\mathrm{T}} > 100$ GeV/c.

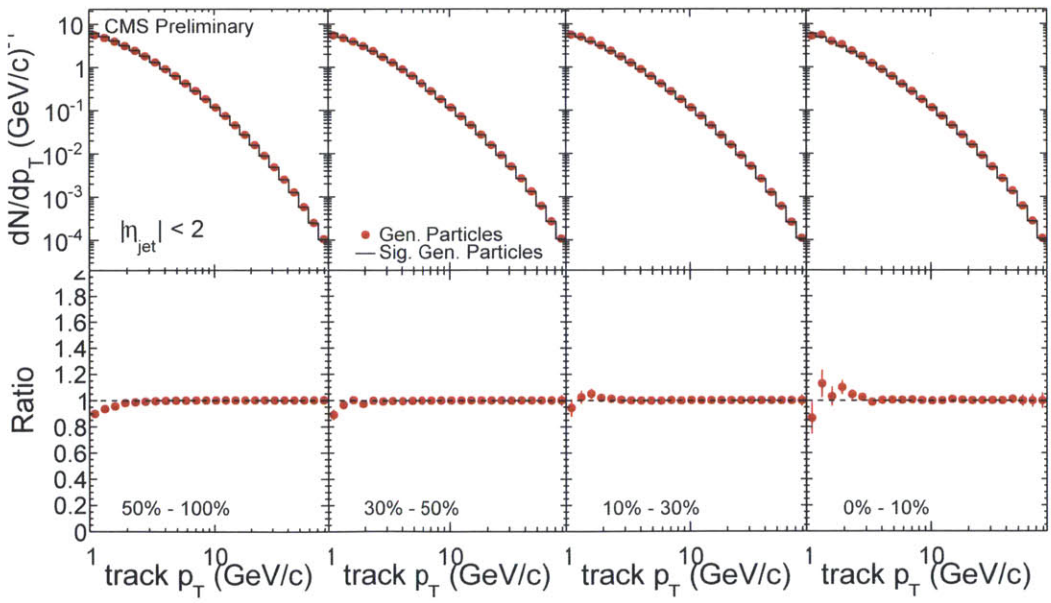


Figure 4-18: Generator level particle background subtraction for track $p_{\mathrm{T}}$ analysis after require additionally that the reconstructed jets have genjet $p_{\mathrm{T}} > 100$ GeV/c.

threshold more often than the jets which sit on top of a downward fluctuation in the underlying event and so fluctuated below the jet threshold. Hence whenever we are looking at the tracks within cones of reconstructed jets, we are preferentially looking at regions in the underlying events which have upward fluctuations.

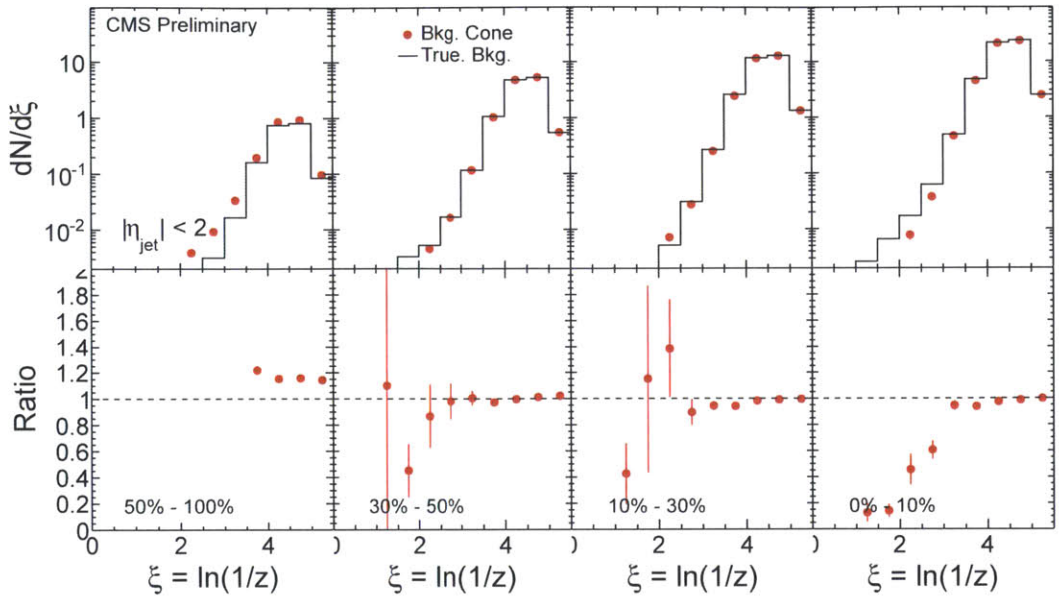


Figure 4-19: Generator particle level background in reflected cone vs truth HYDJET generator level background in jet cone. The above unity ratio in peripheral events are below one due to a technical issue whether or not to include underlying event in PYTHIA as true signal particles.

To test this hypothesis more explicitly, we can go one more level towards the generator truth: we can explicitly separate the particles coming from the PYTHIA events and the particles that come from HYDJET events within the jet cones. This is shown in Fig. 4-19 and Fig. 4-20. From these figures we see that indeed the true background level under the jet cones for reconstructed jets is higher than the background level in the average event. Note that in the peripheral events the true background seems to be lower than the estimated background in the $\eta$ reflected cone. This is a technical point, related to how whether the underlying event in PYTHIA should be counted as the part of the signal or not. We will ignore this technical point, since the signal dominates over the background in peripheral events, and the background fluctuation bias correction is not applied for peripheral events..

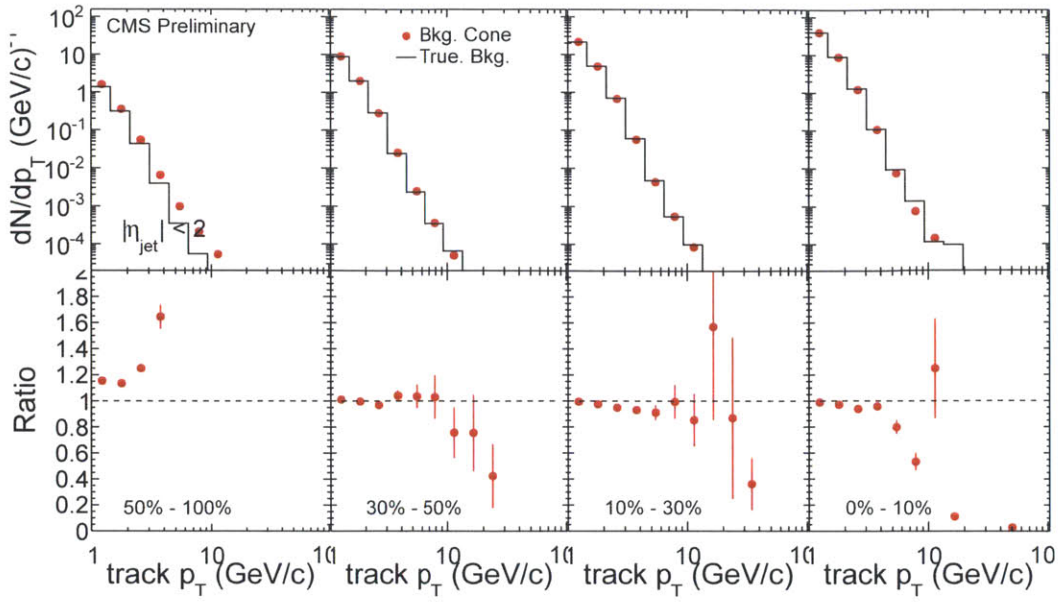


Figure 4-20: Generator particle level background in reflected cone vs truth HYDJET generator level background in jet cone. See capture of Fig. 4-19 for more details.

### Jet Reconstruction Bias

We now turn our attention to the slope in the MC PbPb to pp fragmentation function ratio for higher $p_{\mathrm{T}}$ tracks. This should not be related to the background effects since the background falls off very sharply above $p_{\mathrm{T}} \gtrsim 4$ GeV/c. To narrow down this bias, we can go further towards the generator truth. We repeat the MC analysis using only the signal generator particles from the embedded PYTHIA event. This is shown in Fig. 4-21 and Fig. 4-22.

From Fig. 4-21 and Fig. 4-22 we see that the true fragmentation function of the embedded signal jets are biased to be harder in the reconstructed PbPb jets than the reconstructed pp jets. This can be understood in the sense that jets which fragment harder are easier to reconstruct and have higher energy scale to be more likely to cross the jet threshold. This gives the sloping bias in the fragmentation function of the reconstructed PbPb jets relative to the reconstructed pp jets. This effect is larger in PbPb because PbPb jets have worse energy resolution.

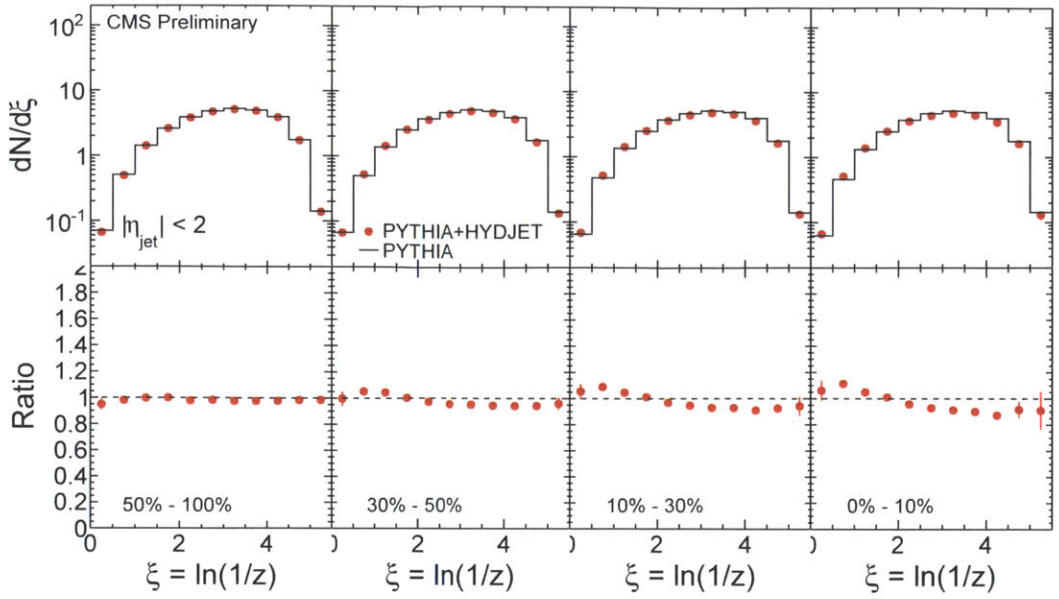


Figure 4-21: Truth signal event generator particle level fragmentation function for reconstructed jets in MC $\xi$ analysis. Here PbPb is PYTHIA+HYDJET and pp is PYTHIA.

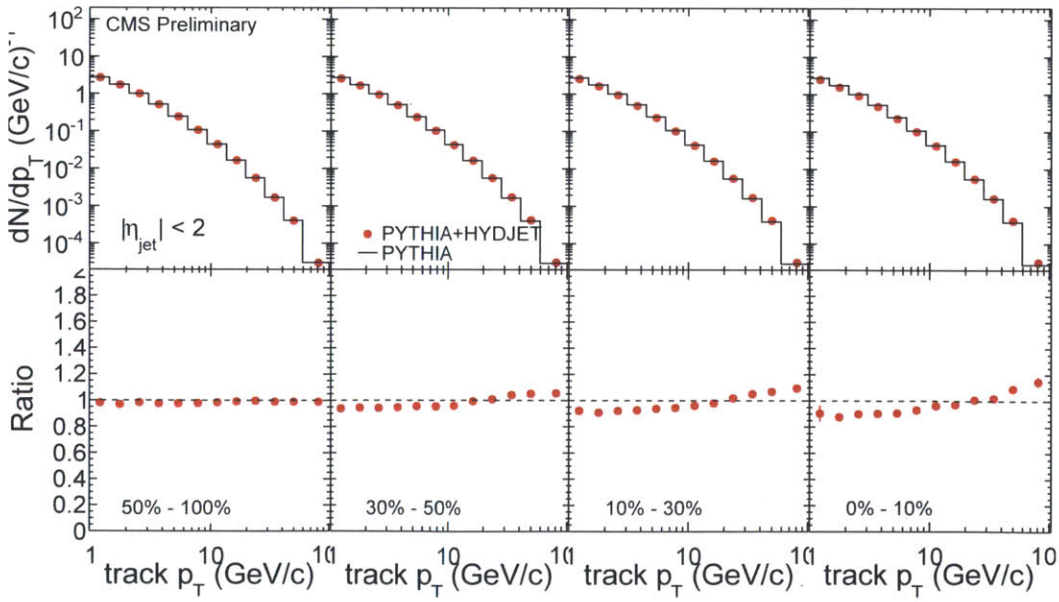


Figure 4-22: Truth signal event generator particle level fragmentation function for reconstructed jets in MC track $p_{\mathrm{T}}$ analysis. Here PbPb is PYTHIA+HYDJET and pp is PYTHIA.

### 4.7.3 Correcting the Biases

To fundamentally correct the reconstruction related biases that we discovered in Sec. 4.7.2, we should improve the jet reconstruction so that it is not biased by background fluctuations or jet fragmentation. However this is a very difficult problem. An easier solution is to derive analysis level corrections to the fragmentation function based on MC and then check that the MC is sufficiently similar to data so that errors to the correction is small. This is the strategy we will follow in the thesis.

The idea to the MC based corrections to the fragmentation function is to correct the problem as close to the source as possible. We want to avoid high analysis level corrections, so as to force the MC analysis to have PbPb/pp ratio of 1. This would introduce too much dependence on the MC and also make the size of the correction un-necessarily large. We will assume that the bias effects from the background fluctuation and jet reconstruction arise independently and so the corrections are factorized – this gives an overall smaller correction since they add in quadrature (since the independently fluctuating effects sometimes add and sometimes cancel). In particular we assume:

1. The bias is independent of tracking effects, and thus can be derived fully from generated particles.

2. The bias introduced by background fluctuation is independent from the bias introduced by jet reconstruction.

As a result of the second assumption we may correct the estimated background from the $\eta$ reflected cone for the background fluctuation bias without correcting particles in the jet cone. And for the fragmentation bias introduced by the jet reconstruction, we may derive the correction based on the signal event generated particles.

For the fluctuation bias correction we weigh the tracks in the $\eta$ reflected cone with the inverse of the ratio in Fig. 4-16. If we apply only this correction then the full reconstruction MC analysis now looks like Fig. 4-23, Fig. 4-24.

After the fluctuation bias correction, we see that the excess at low track $p_{\mathrm{T}}$ is

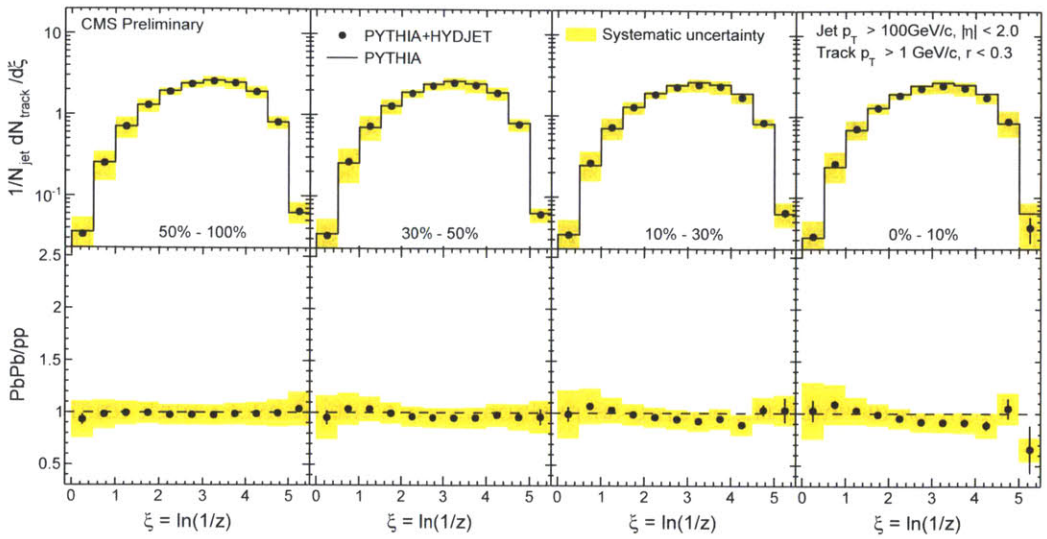


Figure 4-23: Full analysis in $\xi$ for reconstructed Monte Carlo events corrected for background fluctuation bias only.

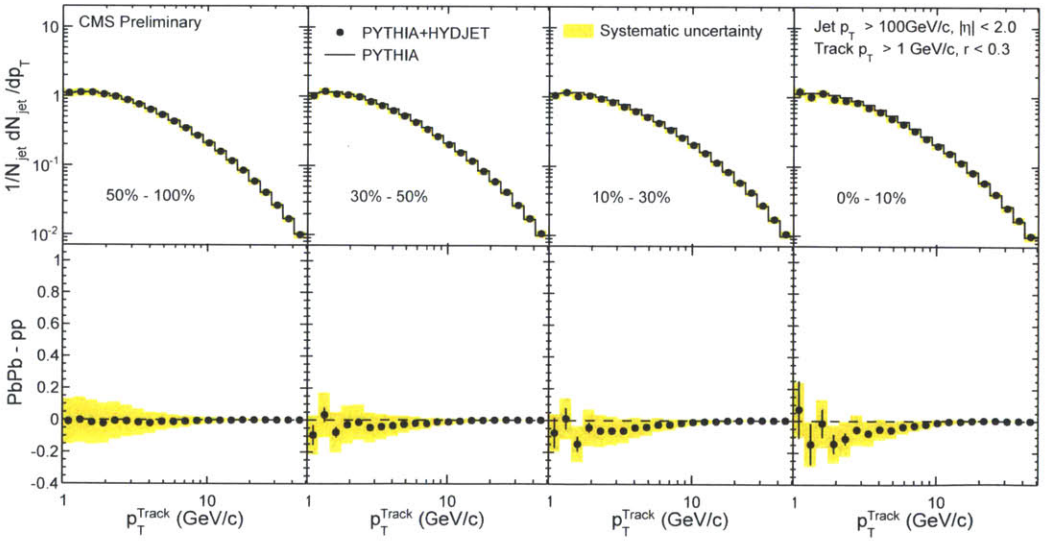


Figure 4-24: Full analysis in track $p_{\mathrm{T}}$ for reconstructed Monte Carlo events corrected for background fluctuation bias only.

now gone. Note also that due to the factorized nature of the correction, the jet reconstruction bias is still there.

For the jet reconstruction bias, we apply a correction based on the relative difference between the signal truth event fragmentation in PbPb jets and the truth fragmentation in pp jets as shown in Fig. 4-22. Similar to how we smear the pp jet energy to match PbPb jet energy resolution, we here artificially bias the pp reference to have the similar bias level as the PbPb jet. Thus to correct for the bias caused by jet reconstruction we weigh tracks in the pp jet cone by the inverse of the ratio in Fig. 4-22. Note there is a subtle technical point in this approach. We cannot use the direct ratio as in Fig. 4-22 because we are weighting the tracks in the pp jet cone on a track by track basis. Thus we need to take the correction based on the PbPb/pp fragmentation ratio before correcting for the background. To keep the background effect factorized, what is actually done in the analysis is to add to the pp fragmentation function the same background as in the PbPb MC before taking the ratio. Then the resulting inverse ratio is used to weight the tracks in the pp jet cone. This is only a technical point, but the essential idea is to derive the correction based on Fig. 4-22. If we only apply the jet reconstruction bias correction then the full reconstruction MC analysis looks like Fig. 4-25 and Fig. 4-26.

With only the jet reconstruction bias correction we see that the sloping deviation from 1 at higher track $p_{\mathrm{T}}$ is now gone. Again note the factorized nature of the correction, the fluctuation bias now explicitly remain.

Finally we apply both bias corrections at the same time. The result is shown as the solid black dots in Fig. 4-27 and Fig. 4-28.

With both corrections applied, we see that the MC analysis ratio is finally consistent with 1 within the statistical and estimated systematic uncertainties. With these two additional analysis level corrections, we consider the analysis to be complete. In the next section we estimate the systematic uncertainty of the full analysis.

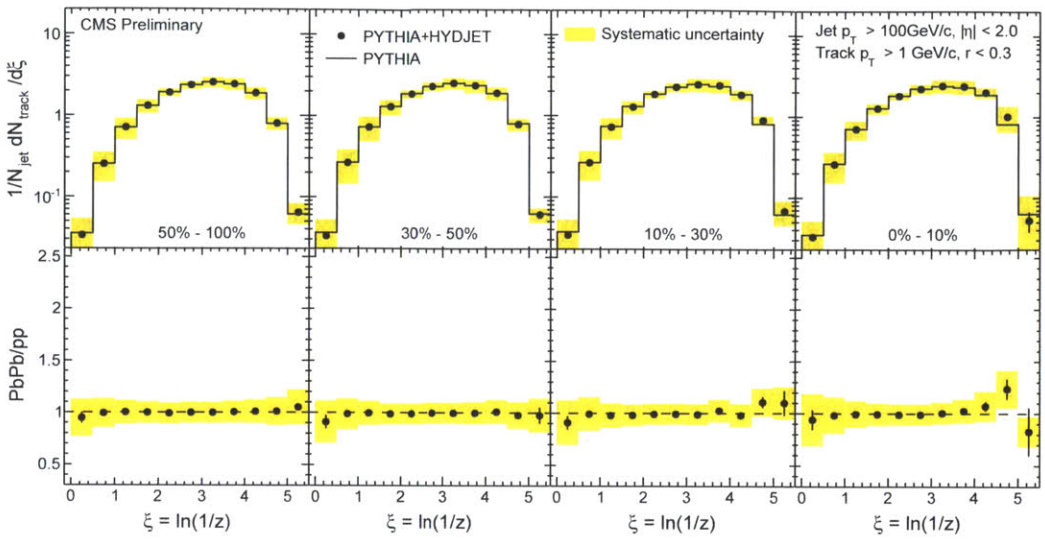


Figure 4-25: Full analysis for reconstructed Monte Carlo events corrected for jet reconstruction bias only.

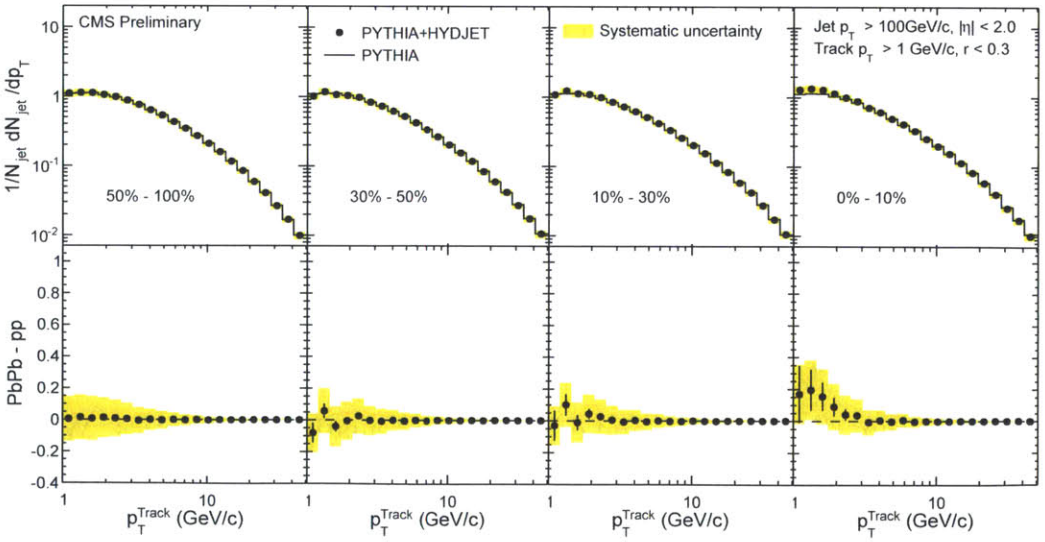


Figure 4-26: Full analysis for reconstructed Monte Carlo events corrected for jet reconstruction bias only.

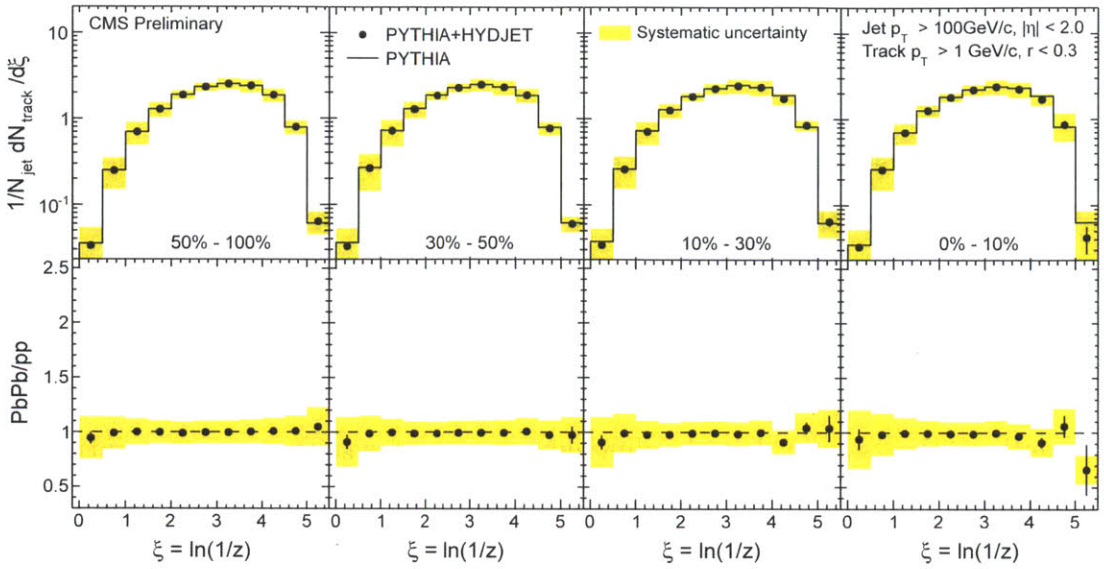


Figure 4-27: Full analysis for reconstructed Monte Carlo events after all bias corrections.

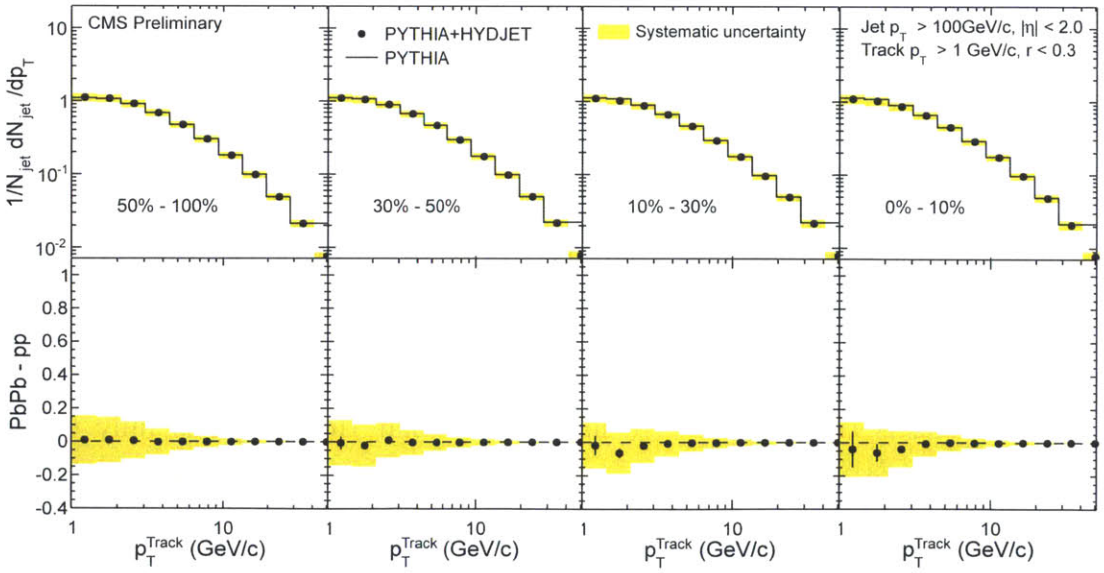


Figure 4-28: Full analysis for reconstructed Monte Carlo events after all bias corrections are applied.

## 4.8 Systematic Uncertainties

This section will give an estimate of the systematic uncertainties of the fragmentation function measurement. It will try to quantify to limits of the accuracy of the measurement and the sensitivities of the final observables to various assumptions of the analysis. To estimate the total systematic uncertainty of the final measurement, each input to the analysis will be examined and its associated uncertainty estimated. We will try to identify the dominant uncertainties to build some intuitions to understand the sensitivities of the analysis. At the end we will combine the individual uncertainties together. We assume that the different sources of systematic uncertainties arise independently and thus can be added in quadrature. To understand where errors may arise in the analysis, it is helpful to review the analysis components listed in Sec. 4.1. As one may guess, the dominant uncertainties will come from jet and track reconstruction and effects of the underlying background. In what follows a discussion will be given for each input to the analysis, namely, event selection, jet reconstruction and selection, track reconstruction and selection, underlying event subtraction, pp reference and finally MC dependencies of the analysis corrections.

### 4.8.1 Uncertainties from Event Selection

Uncertainties in the event selection arise mainly as a result of either inefficiency in the event selection that biases the analysis data sample or background events leaking into the event selection. Starting from the online trigger, each stage of the event selection procedure may contribute biases to the final analysis events. First selection of the collisions is the trigger. We have shown that the trigger is fully efficient for reconstructed jets with offline $p_{\mathrm{T}} > 100$ GeV/c (Fig. 3-15). In addition, the calorimeter jet trigger was also shown to be efficient for generator level jets with $p_{\mathrm{T}} > 100$ GeV/c (Fig. 3-14). Thus the trigger is not the major contribution to event selection uncertainties. Second selection is the offline event selection. The offline event selection looks for any inelastic collision activity in the detector, and is thus a looser event selection than the requirement of a high $p_{\mathrm{T}}$ jet in the event. Thus it

contributes little to the event selection uncertainties. Third selection is the offline jet event pre-filtering which requires at least one reconstructed calorimeter jet with $p_T > 90$ GeV/c (Sec. 4.3). This was found to cause a slight inefficiency for the analysis particle flow jets at $p_T \sim 100$ GeV/c (Fig. 4-4). The last event selection is the analysis jet $p_T$ threshold at 100 GeV/c. We had shown that for jets with $p_T > 100$ GeV/c the jet fake rate is low and the efficiency is essentially 100% as seen in Fig. 3-27. Thus the analysis jet threshold is not expected to affect the event selection much.

In summary we find the the dominant event selection uncertainty to be the jet event pre-filtering. To estimate the effect of this jet event pre-filtering inefficiency, the analysis was repeated with a higher jet threshold at 120 GeV/c where even the jet event pre-filtering becomes fully efficient (Fig. 4-4). The result of the repeated analysis is shown in Fig. 4-29.

Comparing the repeated data analysis with higher jet threshold at 120 GeV/c (black solid dots in Fig. 4-29) to the standard analysis with jet threshold at 100 GeV/c (open red circles in Fig. 4-29), it can be seen that the jet event skimming inefficiencies does not cause an uncertainty beyond statistical fluctuations. For these reasons we conclude that uncertainties in event selection are not the dominant contribution to the systematic uncertainties to the jet fragmentation function.

### 4.8.2 Uncertainties from Jet Reconstruction and Selection

Uncertainties in jet reconstruction and selection can arise in three ways:

1. Jet finding efficiency and fake rate

2. Jet energy scale and resolution

3. Jet reconstruction biases

As mentioned before, at $p_T > 100$ GeV/c, jet finding efficiency and fake rate contribute negligible errors (Fig. 3-27). Jet energy scale affects the fragmentation function during the jet selection as well as in the calculation of the $\xi$ variable. In the track $p_T$ analysis, jet energy scale enters only in terms of the jet selection. Finally, jet

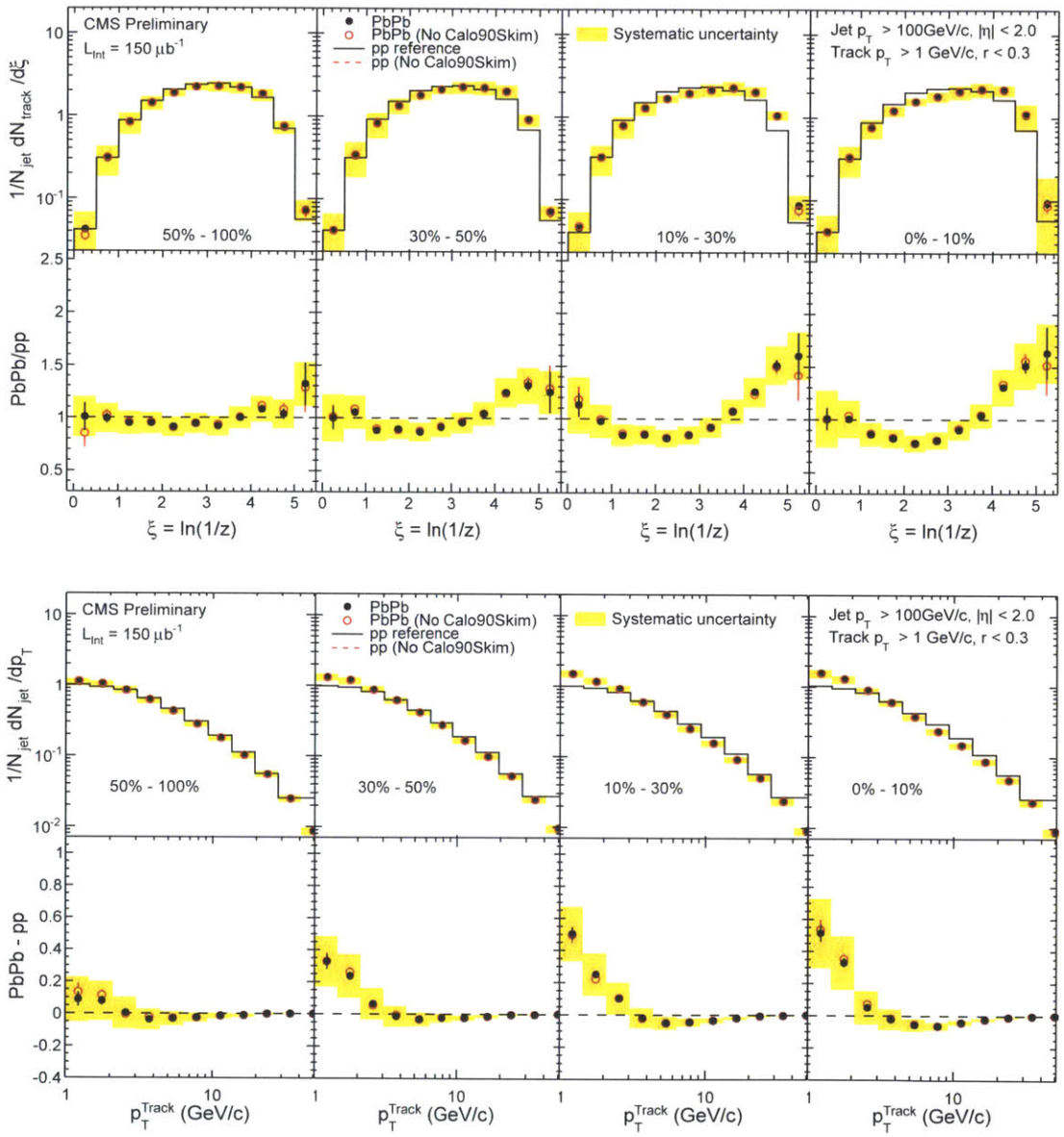


Figure 4-29: Analysis repeated on jet triggered dataset directly without offline jet event pre-selection of requiring at least one calorimeter jet with $p_{\mathrm{T}} > 90\,\mathrm{GeV}/c$.

reconstruction biases contribute systematic uncertainty to the fragmentation function because of the steeply falling jet $p_{\mathrm{T}}$ spectrum in combination with a finite jet reconstruction resolution. Whenever a jet threshold cut is made on the reconstructed jet energy, jets with true $p_{\mathrm{T}}$ below the threshold will enter the analysis due to the finite energy resolution. The reconstructed energies of these jets with true $p_{\mathrm{T}}$ slightly below the threshold fluctuate and they compete to cross the analysis threshold. If there is any correlation between the reconstructed jet energy scale with the fragmentation function, then jets with a fragmentation function that gives a slightly higher reconstructed energy will preferentially cross the threshold. Because the jet $p_{\mathrm{T}}$ spectrum is steeply falling, much more jets with overestimated energies will enter the analysis than jets with underestimated energies leave the analysis. This results in a bias in the final reconstructed fragmentation function.

The uncertainty due to the energy scale is estimated by shifting the energy of the jet in the PbPb data by 5%. This amount was determined by combining in quadrature the uncertainty of jet energy scale in pp data (3%), the MC jet energy scale non-closure in PYTHIA+HYDJET (1%), and change in jet energy scale observed when the fragmentation pattern was modified by arbitrarily adding particles to the jet in PYTHIA+HYDJET events (4%). The resulting change to the fragmentation function is seen in Fig. 4-33, Fig. 4-34.

In order to estimate the effects of the jet energy resolution, we smear the fragmentation functions from PbPb data after varying the jet energy with the additional jet energy resolution due to the underlying event. The systematic uncertainty is assigned by comparing the fragmentation function before and after smearing the jet momentum.

The bias due to jet reconstruction is discussed in Analysis section 4.7.2. It is noted that there is a correlation between reconstructed jet energy with the jet fragmentation function. Jets that fragment harder have a higher energy scale and are thus more likely to cross the energy threshold. This is also a correlation between the jet energy and the charged fraction of the fragmentation products. In the ideal analysis we may correct the jet energy iteratively as a function of the measured fragmentation. We

did not attempt this in the present analysis since it is an higher order effect of the jet energy scale. It is worth to note that this bias is accounted for by the relative PbPb/pp bias correction in Sec. 4.7.3. This bias correction however depends on the jet fragmentation pattern in the Monte Carlo, which we know to be different than data. The uncertainties that arise due to Monte Carlo dependence will be discussed later.

### 4.8.3 Uncertainties from Track Reconstruction and Selection

The systematic uncertainty in fragmentation function arising from the tracking efficiency and fake rate consists of two parts:

1. Uncertainties in the estimated tracking efficiency and fake rate

2. Uncertainties in the correction procedure.

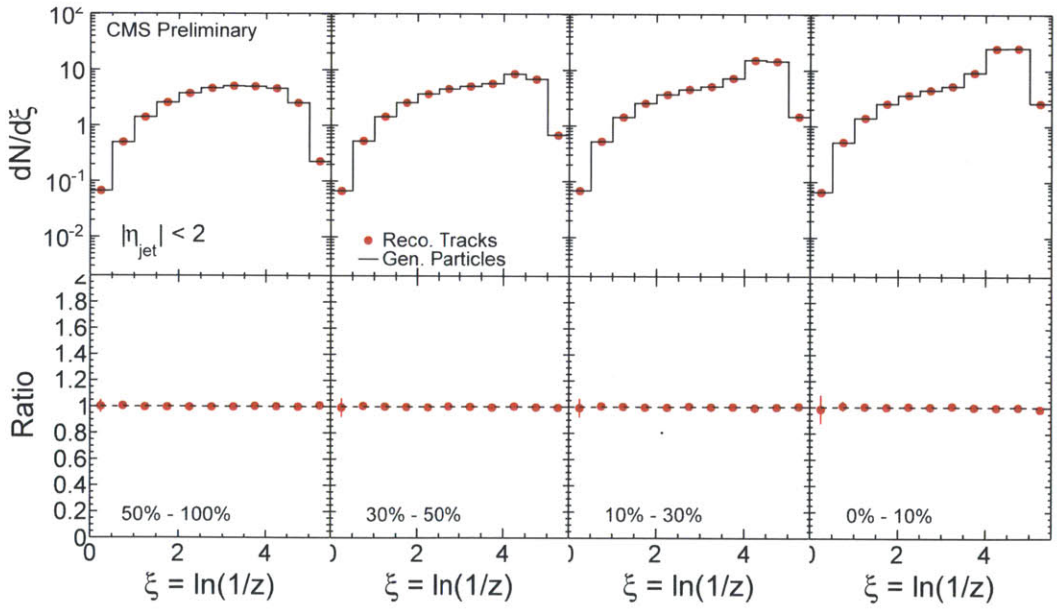


Figure 4-30: Ratio of PbPb fragmentation functions before background subtraction obtained from reconstructed tracks are compared to fragmentation functions obtained from identical analysis using generator level charged final state particles. Both are derived from the same simulated MC PYTHIA+HYDJET using identical, selected reconstructed jets. The four panels show four bins in increasing centrality (left–right).

Tracking corrections need to be applied across a wide $p_{\mathrm{T}}$ range and in multiple observables. Special care needs to be taken when the efficiency is correlated with the final observable. For example, we observe a correlation between the tracking efficiency with the jet reconstruction, since tracking information was used in the particle flow jet reconstruction. Even if tracking information is not explicitly used in the jet reconstruction, there still exists a correlation between jet reconstruction and tracking efficiency due, for example, to to nuclear interactions in the tracker that interrupt a particle's trajectory and prevent it from reaching the calorimeter. The effect of these correlations can be tested in a closure test where the fragmentation function using corrected, reconstructed tracks is compared with the fragmentation function obtained by charged final particles at generator level. To keep tracking effects factorized from jet effects, the same reconstructed jets are used in both cases. The tracking closure test in $\xi$ is shown in Fig. 4-30 for PbPb MC and in Fig. 4-31 for pp MC.

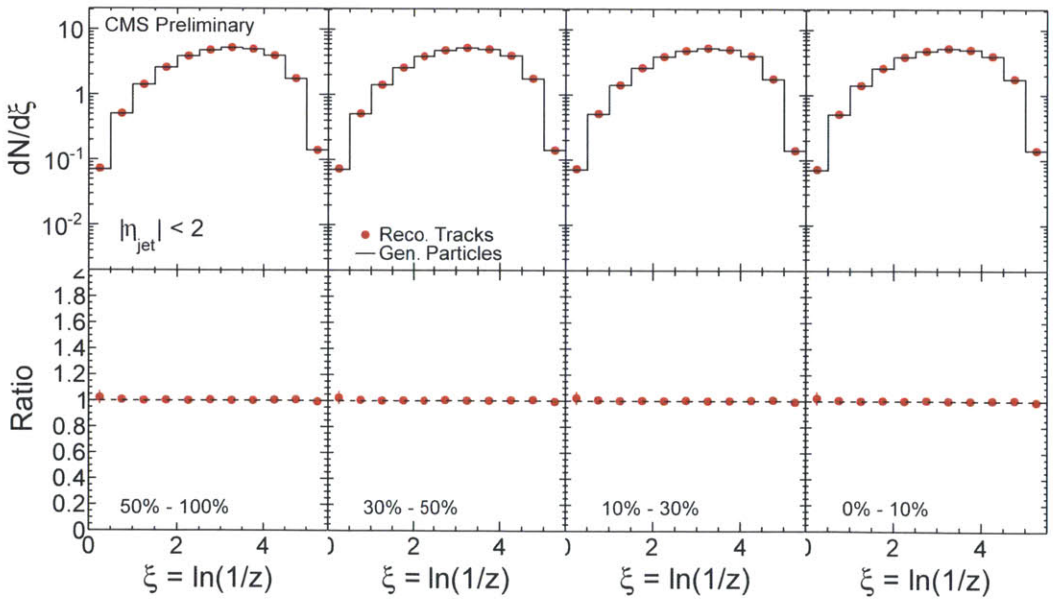


Figure 4-31: Ratio of pp fragmentation functions before background subtraction obtained from reconstructed tracks are compared to fragmentation functions obtained from identical analysis using generator level charged final state particles. Both are derived from the same simulated MC PYTHIA using identical, selected reconstructed jets. The four panels show four bins in increasing centrality (left–right).

Based on the tracking correction closure test, we can see that the effect of the tracking procedure on the fragmentation function is at the level of 1-2%.

The real challenge in measurements using tracks is in obtaining the true tracking efficiency in data. In all of the tracking analysis so far, the efficiency is derived based on Monte Carlo. This is the traditional way of studying tracking because the main MC dependence is how well the tracker is simulated. Dependences on physics processes is less important, since, for example, a pion track looks the same no matter what physics process produced it. Nevertheless, detector readout effects related to the high occupancy in the heavy ion collisions can result in different tracking efficiency in data and MC. In pp data driven tracking efficiency can be estimated by tag-and-probe techniques using resonance decays. This technique is not yet available in heavy ion analysis. Nevertheless some indirect data driven analyses were performed to cross check the tracking performance in the heavy ion events. Fig. 4-32 shows a study where the fraction of the sum track $p_{\mathrm{T}}$ inside the jet cone out of the reconstructed jet energy is plotted as a function of centrality.

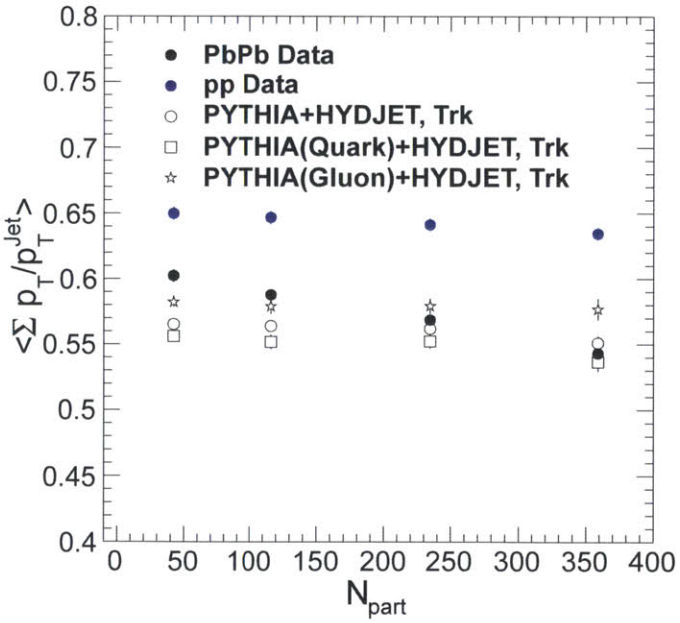


Figure 4-32: Sum of track $p_{\mathrm{T}}$ within jet cone divided by the jet energy for jets with $p_{\mathrm{T}} > 100$ GeV/c.

From Fig. 4-32 we see that the fractional total track $p_{\mathrm{T}}$ changes with centrality in PbPb data (black solid dots) even though the same jet $p_{\mathrm{T}} > 100$ GeV/c selection was used. This change is partially due to the increased jet energy fluctuations, as demonstrated by the corresponding pp total track $p_{\mathrm{T}}$ fraction (blue solid dots), where the centrality dependences comes from the artificial jet resolution smearing. However the variation due to the jet $p_{\mathrm{T}}$ smearing is only about 1-2%. High multiplicity effects in simulated heavy ion also show a small change in the total track $p_{\mathrm{T}}$ fraction (open black circles). However again, the size of the variation in MC cannot explain the size of the variation in data. One possible explanation is physics: since there is jet quenching in data, there may be a changing gluon jet to quark jet ratio. Gluon jets are expected to experience more energy loss than quark jets due to the ($\sim$ factor of 2) larger color factor. This hypothesis supports the direction of change as shown by the overlaid total track $p_{\mathrm{T}}$ fraction separately for quark (black open squares) and gluon (black open stars) jets in MC. We see that gluon jets have higher fractional energy in charged particle than quark jets. Thus if the central events in data have relatively less gluon jets, then the total track $p_{\mathrm{T}}$ fraction would decrease with increasing centrality. On the other hand it can also indicate a possible tracking inefficiency introduced by the high multiplicity that is present in data but not in MC. The effect in data is probably a combination of these sources, however because we are uncertain about the true causes, the full effect is quoted as the data driven tracking efficiency uncertainty. From Fig. 4-32 we see that for PbPb data (black solid dots) the variation in the total track $p_{\mathrm{T}}$ fraction changes roughly by 10%. Any tracking inefficiency directly changes the height of the fragmentation function. Thus an overall 10% data driven tracking efficiency uncertainty is quoted for the fragmentation function analysis.

### 4.8.4 Uncertainties from Underlying Event Subtraction

We have discussed in Analysis section 4.7.2 that the background subtraction in central events is not perfect, especially at low track $p_{\mathrm{T}}$ where the background tracks dominates over the jet fragmentation tracks. We saw that this was due to a bias background fluctuation underneath the jet cone. This bias was corrected in the bias corrections

applied. However this correction is MC based and there can be possible additional correlated background fluctuations in data that is not accounted for by MC. As a result we conservatively quote 50% of the generator level background subtraction non-closure (Fig. 4-15) as a contribution to the total systematic uncertainty (Fig. 4-33, Fig. 4-34).

To confirm these estimates, a data driven cross check is performed on the background subtraction. The fragmentation function analysis was repeated with an alternative background subtraction method that uses mixed event background. The mixed event method estimates the background distribution to the fragmentation function using minimum bias PbPb data. For each jet in a jet event, we take tracks from a separate minimum bias event which fall into a cone placed at the $\eta, \phi$ position of the jet from the jet event. Then we compute $\xi$ from the jet and the mixed event tracks and fill the background $\xi$ distribution. The difference between the two methods is quoted conservatively as the uncertainty of the fragmentation function due to data-driven background subtraction uncertainty (Fig. 4-33, Fig. 4-34).

### 4.8.5 Uncertainties from pp Reference

The final physics result in this analysis is the ratio or difference between the jet fragmentation function in PbPb and pp. We expect the systematic uncertainties due to reconstruction in PbPb and pp to work in the same direction and thus cancel partially in the ratio or difference comparison. The only main difference between the PbPb analysis and the pp analysis is the additional pp jet energy smearing. However, since we are quoting a systematic uncertainty of the PbPb result by repeating the analysis artificially smearing the jets with the quadrature difference of the PbPb and pp jet energy resolution (Sec. 4.8.2), this PbPb/pp relative resolution uncertainty is taken account already. We conservatively do not reduce the final systematic uncertainty on the fragmentation function ratio due to the canceling of the PbPb and pp systematic uncertainties.

### 4.8.6 Uncertainties from MC Dependence of Analysis Corrections

One more major contributions to systematic uncertainties come from the error in analysis corrections as a result of the difference in jet physics between data and MC. To estimate the size of this uncertainty we repeat the analysis using two limiting types of signal jets (gluon, quark) embedded into the simulated heavy ion background (See Analysis Cross checks Sec. 4.9). A systematic uncertainty proportional to the deviation from the generator truth in the two cross check analyses is quoted as the uncertainty introduced by the MC based analysis corrections. These are shown in Fig. 4-33, Fig. 4-34.

### 4.8.7 Summary of Systematic Uncertainties in Fragmentation Function

Finally the individual systematic uncertainties are added in quadrature to form the final systematic uncertainty. This is summarized in Fig. 4-33 and Fig. 4-34. From these combined plot of systematic uncertainties, we see that the total systematic uncertainty is indeed dominated by jet energy scale, tracking correction, and background subtraction as we alluded to earlier.

The numerical magnitudes of the systematic uncertainties are tabulated in Tab. 4.1.

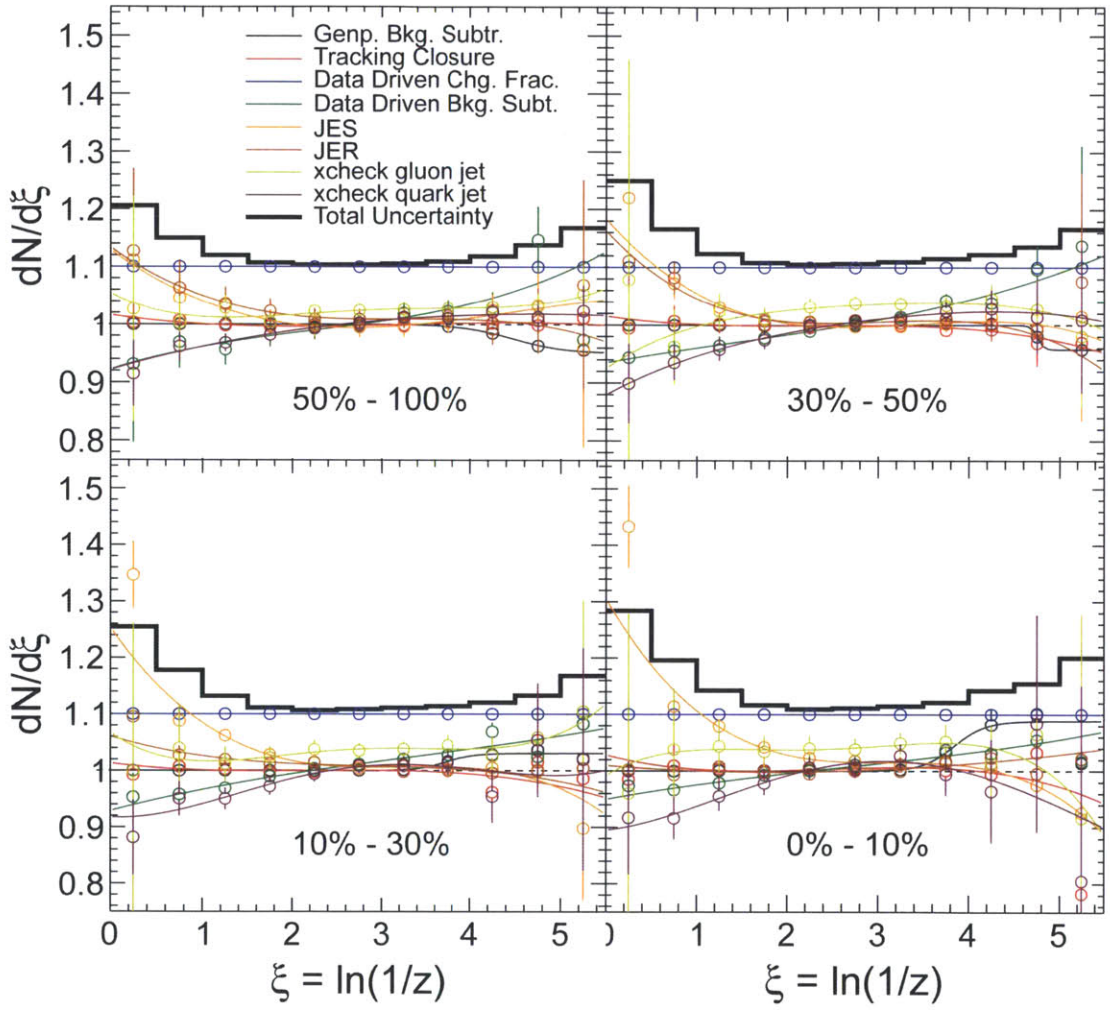


Figure 4-33: Variations of the final fragmentation function ratio in $\xi$ due to uncertainties in the analysis inputs.

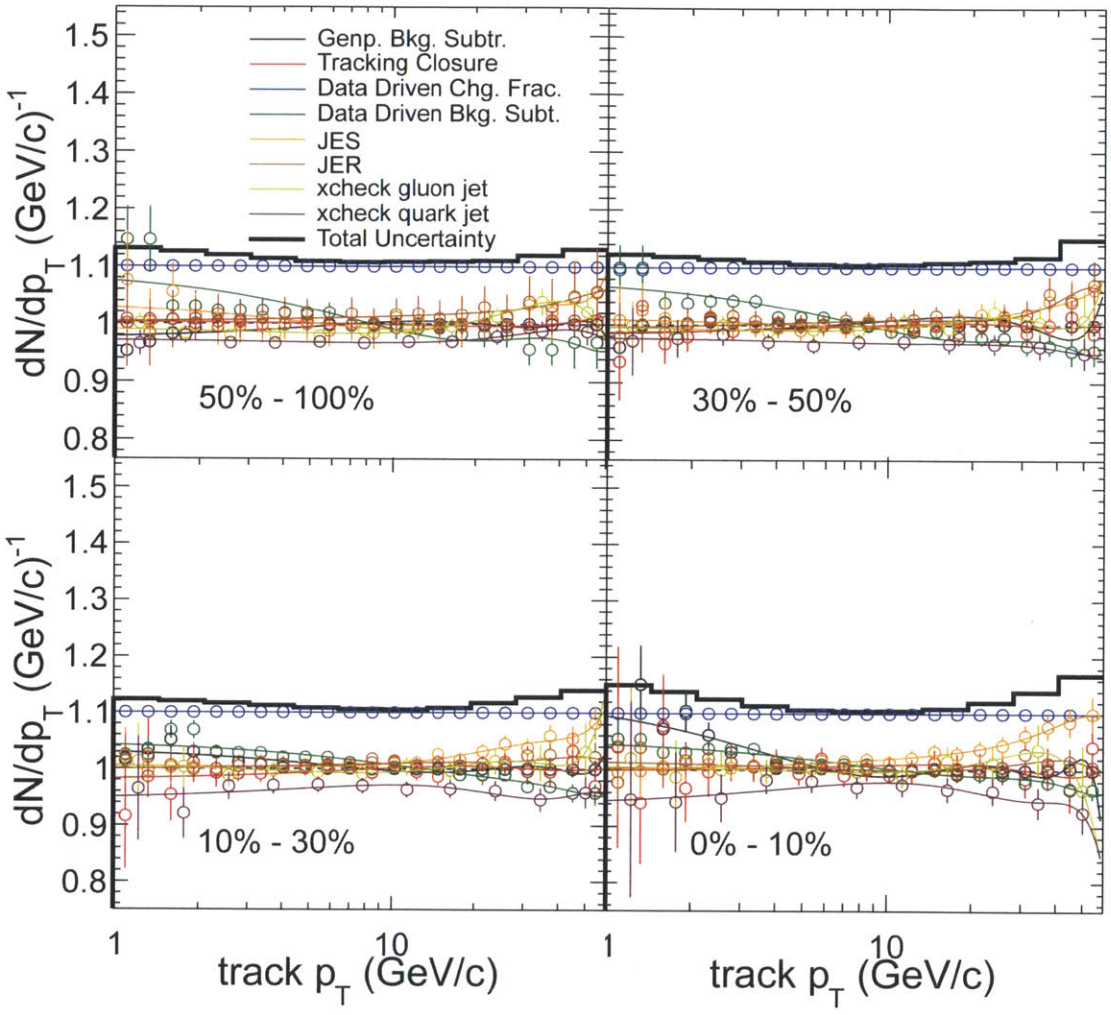


Figure 4-34: Variations of the final fragmentation function difference in track $p_{\mathrm{T}}$ due to uncertainties in the analysis inputs.

Table 4.1: Summary of systematic uncertainties in jet fragmentation function analysis in bins of $\xi$. The values indicate the typical values of the systematic uncertainties and the intervals indicate the range of systematic uncertainties in various centralities.

| Item | Input / Variation | $\xi < 1.5$ | $1.5 < \xi < 4$ | $4 < \xi < 5.5$ |
|---|---|---|---|---|
| Jet Energy Resolution | 10-20% smearing | 5–11% | 2% | 5% |
| Jet Energy Scale | 5% shift | 10–25% | 5% | 5–9% |
| Tracking Efficiency | non-closure | 3% | 2% | 5% |
| Tracking Efficiency | centrality variation | 10% | 10% | 10% |
| Background Subtraction | 50% Bias Correction | 0% | 0% | 4–9% |
| Data driven Bkg. Sub. | Difference between methods | 7% | 2% | 8% |
| Gluon Jet Cross Check | non-closure | 5–7% | 3% | 5–6% |
| Quark Jet Cross Check | non-closure | 10% | 3% | 5–8% |
| Total | | 20–30% | 12% | 17–21% |

## 4.9 Analysis Cross-checks

The analysis and its estimated uncertainties have been presented. The next question is how can we gain some intuition if our estimated uncertainties are covering the true uncertainty intervals given that the data signal is not described by MC. To answer this question we conduct a few cross check analyses.

### 4.9.1 Cross-check on Background Fluctuation bias

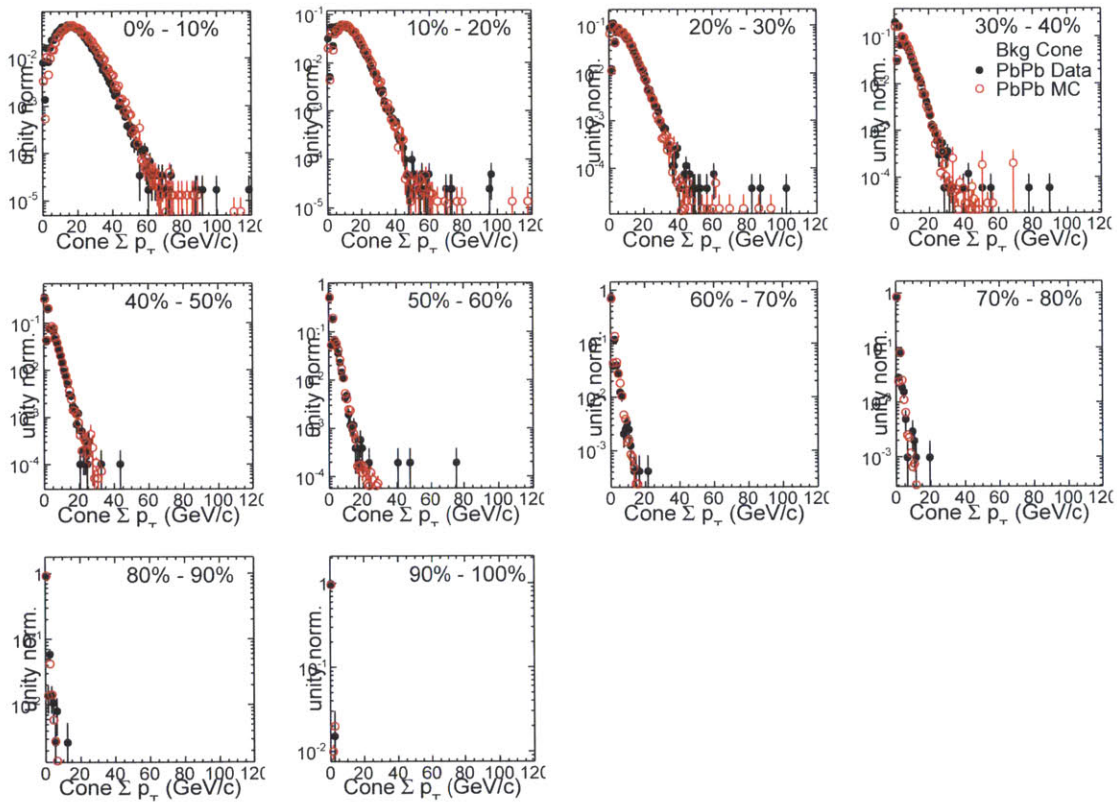


Figure 4-35: Track $p_{\mathrm{T}}$ sum in background cones (after efficiency correction), comparing data and MC (PYTHIA+HYDJET).

We have seen from Sec. 4.8 that at lower track $p_{\mathrm{T}}$, one main systematic uncertainty is due to the background subtraction. Since the background fluctuation bias (Sec. 4.7.2) was mainly derived based on the PYTHIA+HYDJET MC one question is whether the background multiplicity and fluctuation in MC is similar to data such

that we can used the MC derived correction to the background contribution to the jet fragmentation function. To this end we sum the track $p_{\mathrm{T}}$ in the background cones and compare the amount of total energy in the background cones in the PbPb data vs MC, as shown in Fig. 4-35. The average and standard deviations of this sum track $p_{\mathrm{T}}$ in the background cone is extracted from the raw distributions and are shown in Fig. 4-36.

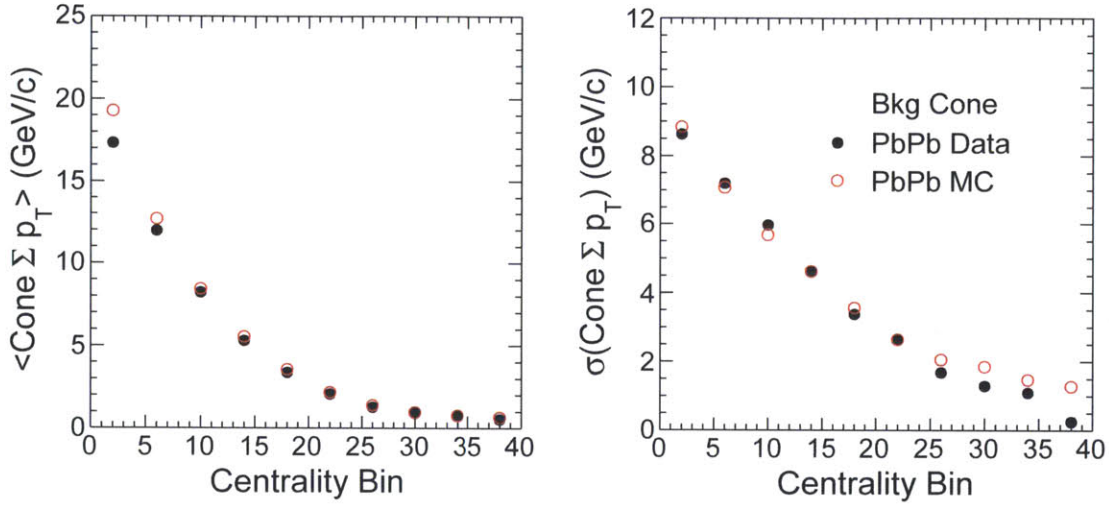


Figure 4-36: Quantify track $p_{\mathrm{T}}$ sum averages and standard deviations in background cones (after efficiency correction), comparing data and MC (PYTHIA+HYDJET).

From the comparison of the background cone track $p_{\mathrm{T}}$ sum and fluctuation we see that data is indeed consistent with MC. This is not too surprising as the heavy ion generator HYDJET was tuned to match the multiplicity in data. However what if there is still some unknown correlations in the background that causes additional unforeseen fluctuations bias to the jet fragmentation function? We can perform one more check where the amount of underlying event fluctuation is artificially increased by approximately 20% in the most central analysis centrality bin and repeat the fragmentation function analysis. This is shown in Fig. 4-37.

From Fig. 4-37, we see that even in the catastrophic case that we underestimated the background fluctuation by 20% then the MC analysis is still approximately correct.

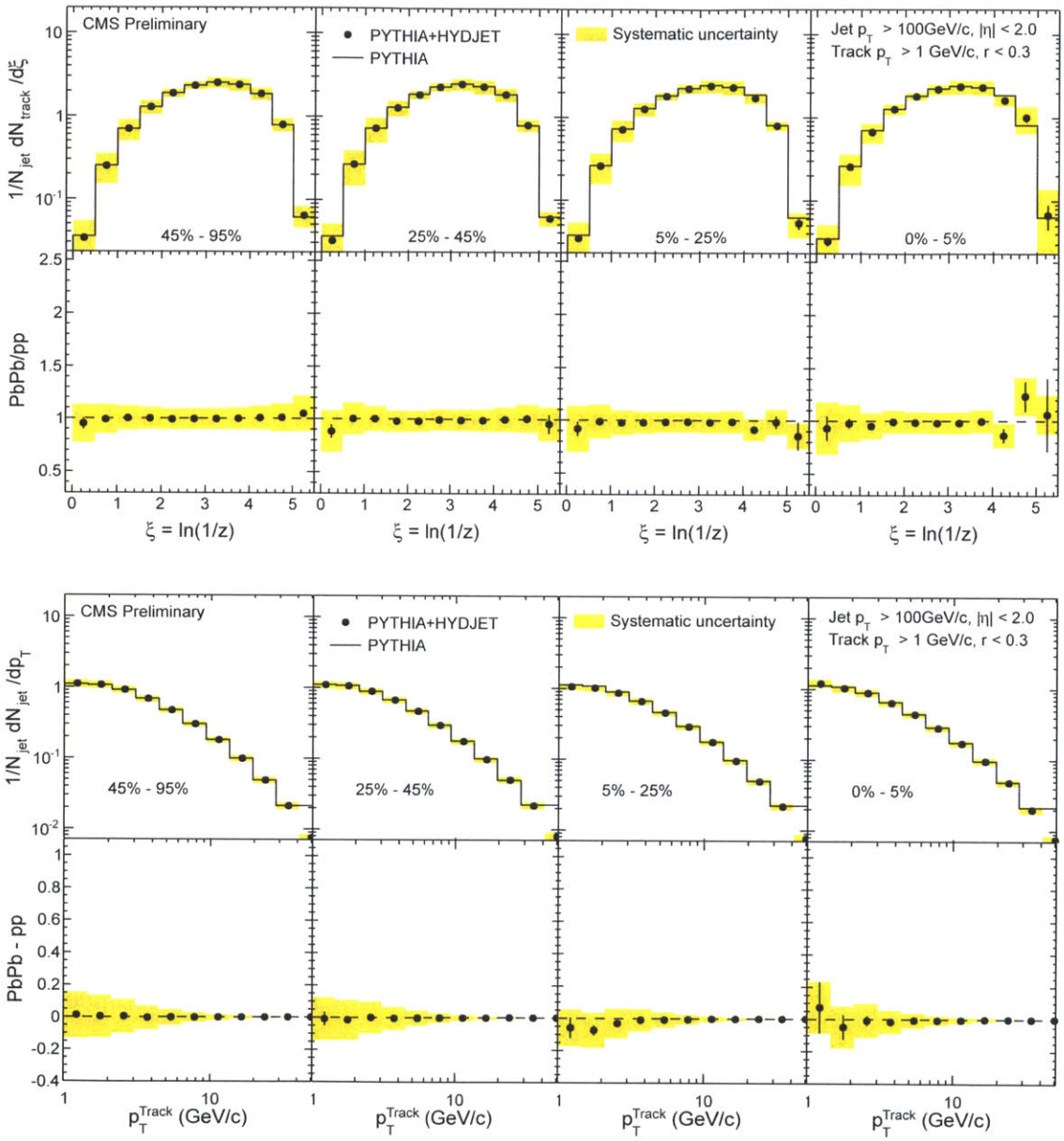


Figure 4-37: Repeat analysis after artificially increasing the underlying event fluctuation by approximately 20%.

### 4.9.2 Cross-check on Modified Signal Jets

Since we know that jets in data do not look like PYTHIA jets (because of jet quenching in data), one may suspect that the corrections derived based on the standard analysis MC (PYTHIA+HYDJET) cannot be well applied to data. Based on the estimated systematic uncertainties we understand that whatever differences in the signal jet in data and MC causes only higher order effects to the derived correction factors. However the question arise: how can we justify this if we do not know how much different are the jets in data than the jets in MC. For these concerns it is a good cross-check to repeat the analysis on different input MC samples with a range of different fragmentation functions in the embedded jet. When the analysis is repeated on these samples, the same corrections based on PYTHIA+HYDJET are used. We can thus build some intuition on the limit of the analysis correction and to what range of different input fragmentation function can the quoted systematic uncertainties cover.

#### Cross check analysis on embedded Gluon Jet sample

First, since we expect the jets in data to be quenched, it is not unreasonable to take a limit of soft fragmentation jets to see the response of our analysis. To this end we embed PYTHIA gluon jets into the simulated heavy ion background. Gluons jets are known to have both softer and wider fragmentation than the average QCD jet. The full reconstruction is performed and the fragmentation analysis was repeated treating embedded gluon PYTHIA jets as data and plain PYTHIA as the pp reference. The result is shown in Fig. 4-38. In the figure the systematic uncertainty band is applied treating the embedded gluon PYTHIA jets as if it were data.

As expected we see that indeed the gluon jets have much softer fragmentation function. Thus from Fig. 4-38 we see that the analysis can reconstruct the correct physics message. We can now ask to what extent is the analysis correct and how much does the estimated systematic uncertainty cover the error? To answer this question we repeat the cross check analysis now using all generator level information: i.e. generator level signal jets and signal generator particles (thus without needing

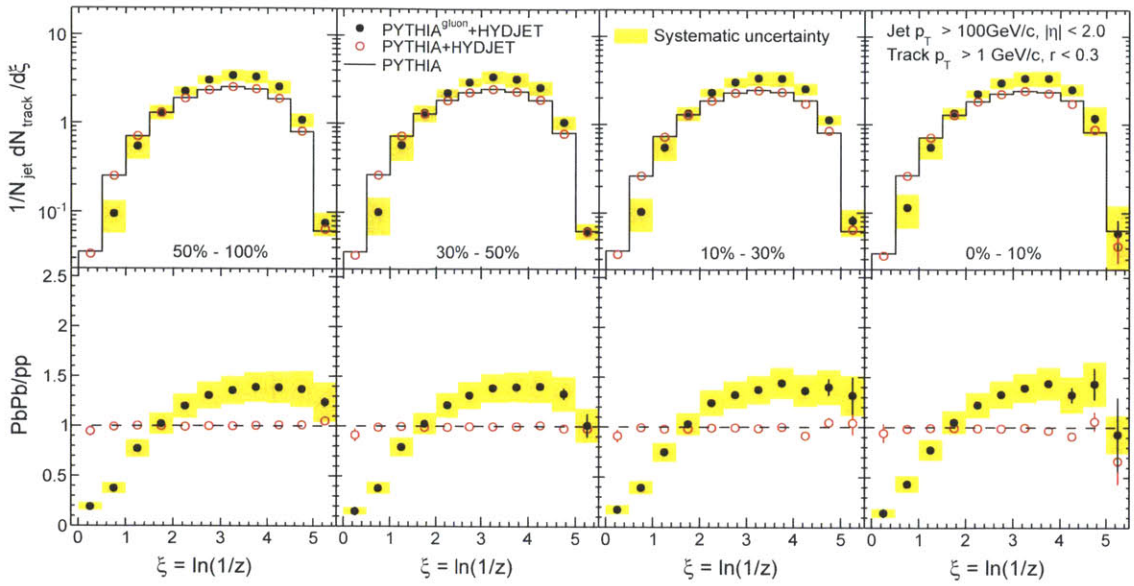


Figure 4-38: Measured fragmentation function of reconstructed PYTHIA gluon jet + HYDJET events.

background subtraction). This full generator truth fragmentation function is shown in Fig. 4-39.

We see that qualitatively the truth fragmentation function is similar to what we reconstructed. To make a precise statement on the coverage of our systematic error band, we overlay the reconstruction fragmentation function ratio with the generator truth fragmentation function ratio, and take their ratio for a direct comparison. This is shown in Fig. 4-40.

From the explicit comparison of the reconstructed vs truth final fragmentation function ratio, we see that while the analysis is not perfect, the estimated systematic uncertainties covered the errors to within one sigma.

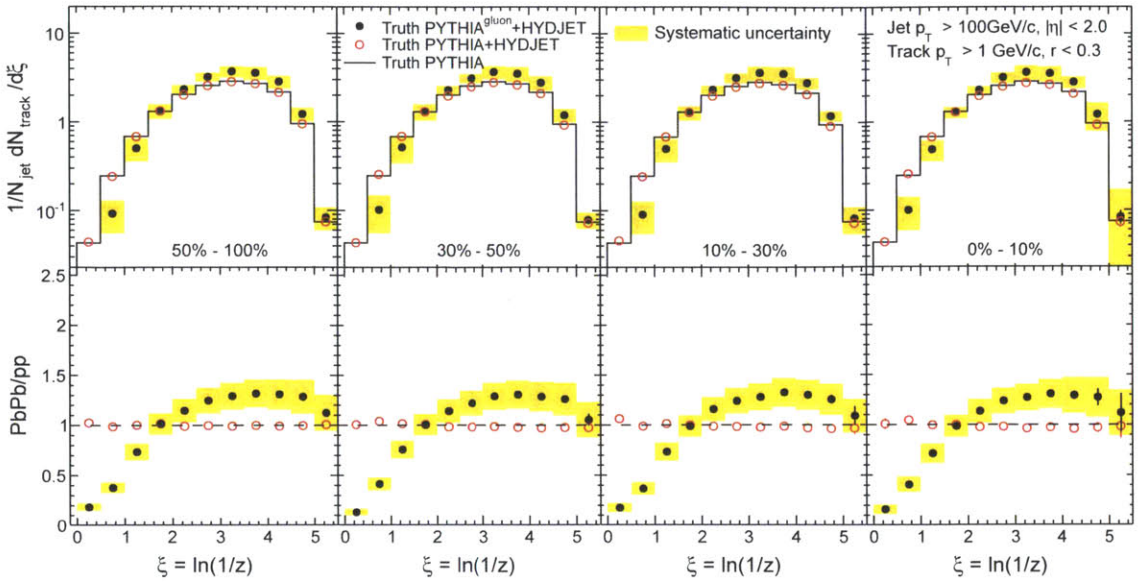


Figure 4-39: Measured fragmentation function of generated truth PYTHIA gluon jet.

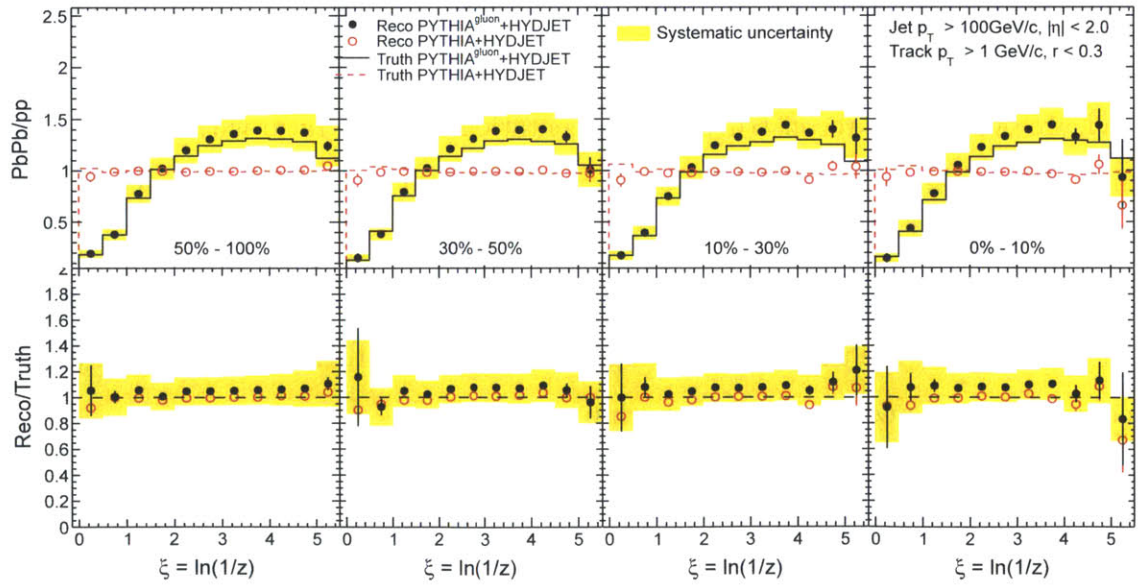


Figure 4-40: Measured fragmentation function of final reconstructed PbPb/pp ratio to the generated truth PbPb/pp ratio for PYTHIA gluon jet + HYDJET events.

### Cross check analysis on embedded Quark Jet sample

Next, we can take the opposite limit to see what is the effect when the jets in data are harder than the PYTHIA jets. This can happen for example in the scenario where all gluon jets are quenched, and only quark jets survive. We embed PYTHIA quark jets into the simulated heavy ion background. Quark jets are known to have harder fragmentation than the average QCD jet. The full reconstruction is performed and the fragmentation analysis was repeated treating embedded quark PYTHIA jets as data and plain PYTHIA as the pp reference. The result is shown in Fig. 4-41. In the figure the systematic uncertainty band is applied treating the embedded quark PYTHIA jets as if it were data.

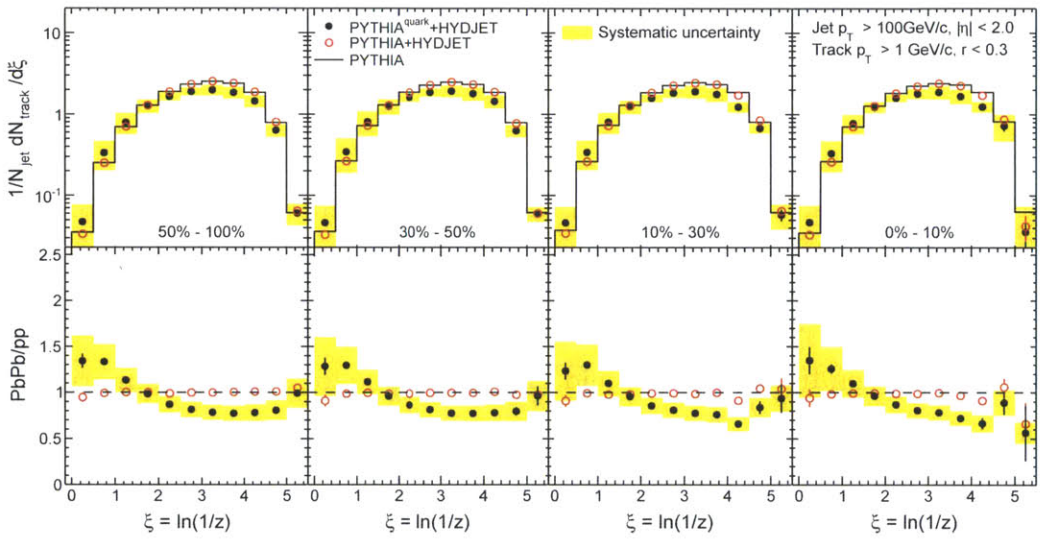


Figure 4-41: Measured fragmentation function of reconstructed PYTHIA quark jet + HYDJET events.

As expected the quark jets have much harder fragmentation function. Fig. 4-41 shows that the analysis can reconstruct the correct physics effect. Similar to the gluon jet cross check, we can now ask to what extent is the analysis correct and how large is the systematic error? To answer this question we again repeat the cross check analysis using all generator level information: i.e. generator level signal jets and signal generator particles. This full generator truth fragmentation function is

shown in Fig. 4-42.

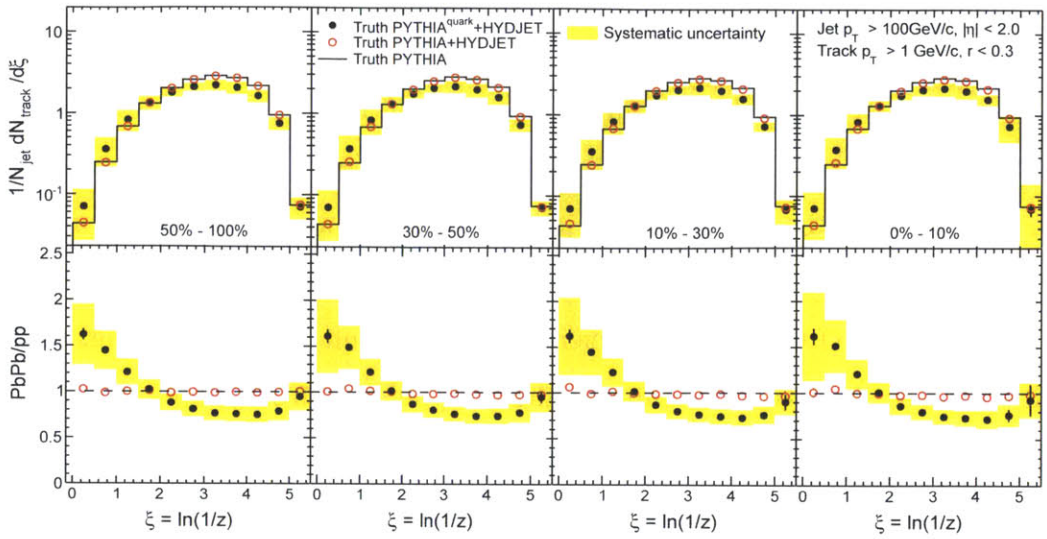


Figure 4-42: Measured fragmentation function of generated truth PYTHIA quark jet.

We see that qualitatively the truth fragmentation function is similar to what we reconstructed. To make a precise statement on the coverage of our systematic error band, we overlay the reconstruction fragmentation function ratio with the generator truth fragmentation function ratio, and take their ratio for a direct comparison. This is shown in Fig. 4-43.

From the explicit comparison of the reconstructed vs truth final fragmentation function ratio, we see here that for the quark jet case, the analysis performance is worse than the gluon jet case. The deviation becomes large at $\xi \sim 0$. This $\xi$ bin is a very challenging part of the analysis because here one or two tracks take up the full jet energy. We see that the reconstructed jet fragmentation function is softer than the truth fragmentation function especially at the low $\xi$ region. This can be explained by the fact that the jet energy gets overestimated for these hard fragmentation at $\xi \sim 0$, thus the reconstructed fragmentation function appears to be softer. From this cross check we see that this effect appears to be larger for quark jets. We are reaching the limit of the analysis in this cross check, yet the error is still within 1 sigma of the estimated systematic error band. One last note is that this effect is

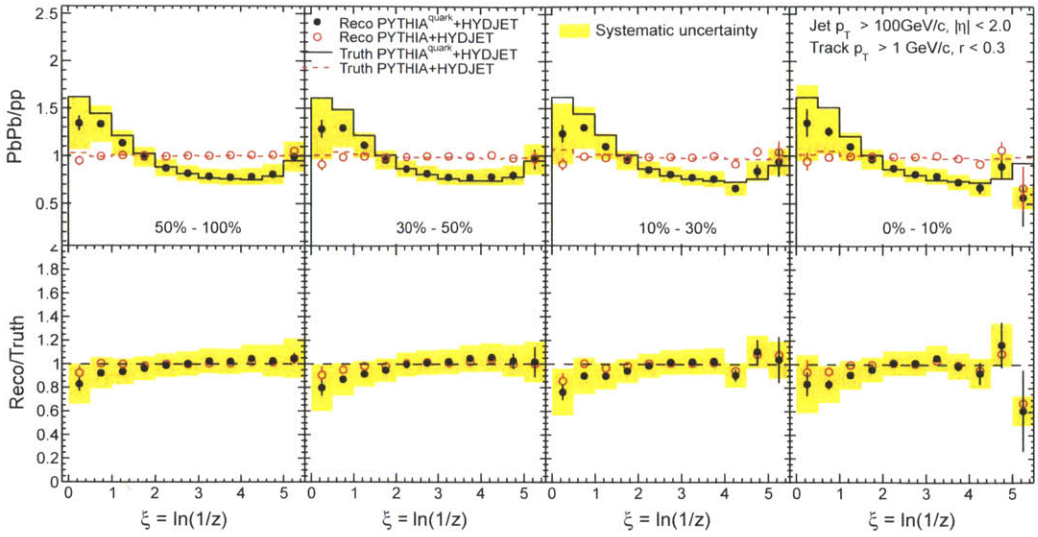


Figure 4-43: Measured fragmentation function of final reconstructed PbPb/pp ratio to the generated truth PbPb/pp ratio for PYTHIA quark jet + HYDJET events.

not an effect of occupancy but due to the intrinsic jet energy scale dependence on (here an extreme case) fragmentation pattern. Thus the effect shows no centrality dependence: it is sizable at peripheral events just as much as central events. This helps to build further confidence to our data analysis where a centrality dependent modification of the fragmentation function is observed.

### Cross check analysis on embedded quenched Jet sample

Finally, we can perform a realistic cross check by using PYQUEN quenched jets based that simulate the quenched jet in data. PYQUEN is a MC generator that models quenched jet as part of the HYDJET generator package. We will use a particular tune of the quenching in PYQUEN called PYQUEN "wide". It is a tune that tries to match the dijet asymmetry measurement in the first LHC data. The model assumes radiative energy loss (but no collisional energy loss). PYQUEN jets are embedded into the simulated heavy ion background. Normally the simulated quenching is a function of centrality. But for this cross check analysis, we embed the most quenched jets, i.e. b=0 case into the HYDJET minimum bias heavy ion events. Again, the full reconstruction is performed and the fragmentation analysis was repeated treating embedded PYQUEN jets as data and plain PYTHIA as the pp reference. The result is shown in Fig. 4-44. In the figure the systematic uncertainty band is applied treating the embedded PYQUEN jets as if it were data.

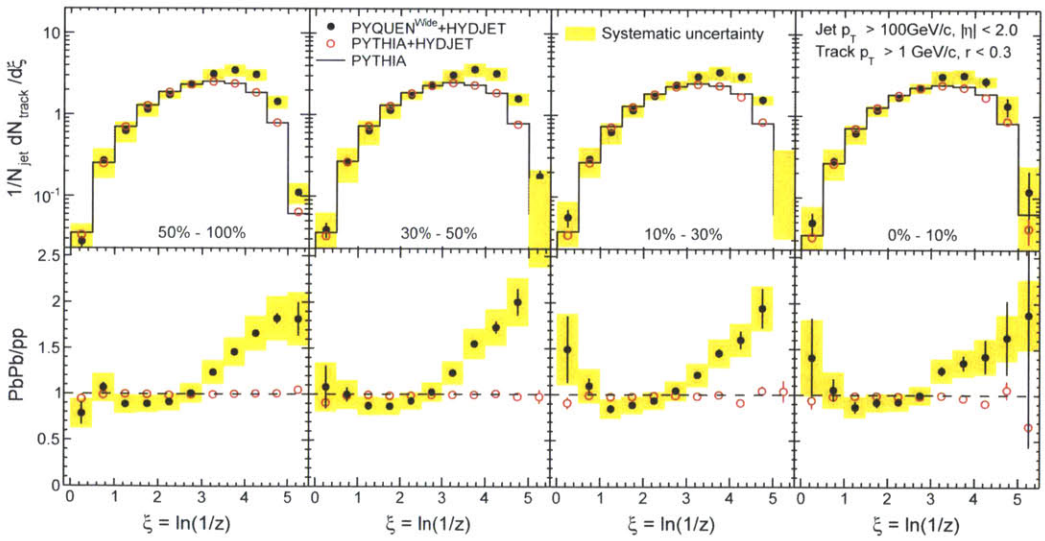


Figure 4-44: Measured fragmentation function of reconstructed quenched PYQUEN + HYDJET events.

We see that the quenched jets are softer, indicating jet quenching physics that was in the embedded signal (b=0 quenching in all centralities). This cross check has

limited statistics due to the need of special Monte Carlo simulations. We repeat the cross check analysis now using all generator level information: i.e. generator level signal jets and signal generator particles. This full generator truth fragmentation function is shown in Fig. 4-45.

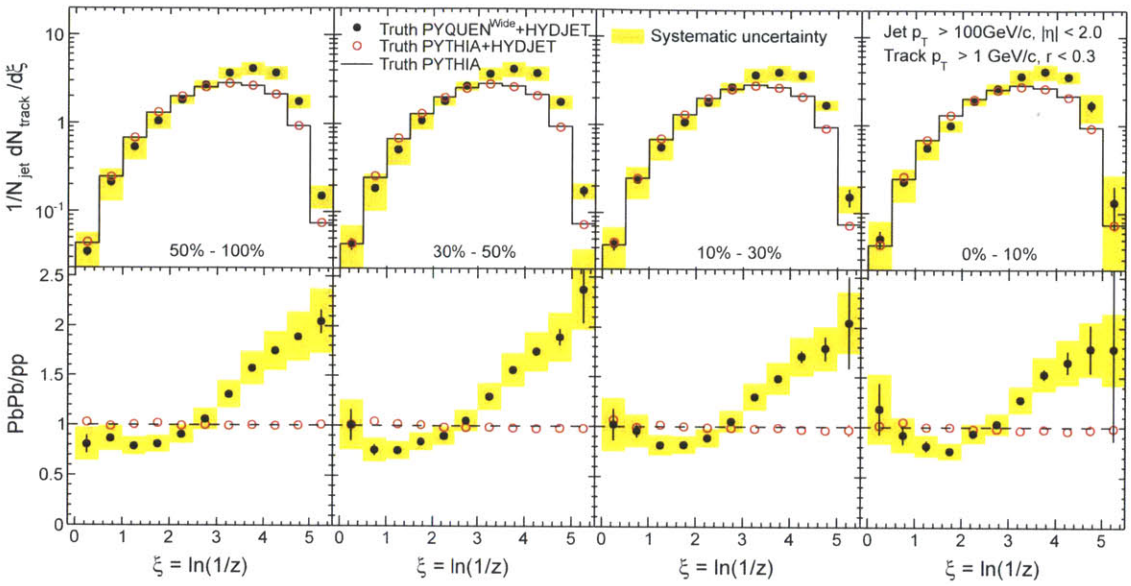


Figure 4-45: Measured fragmentation function of generated truth quenched PYQUEN jets.

We see that qualitatively the truth fragmentation function is similar to what we reconstructed. To make a precise statement on the coverage of our systematic error band, we once more overlay the reconstruction fragmentation function ratio with the generator truth fragmentation function ratio, and take their ratio for a direct comparison. This is shown in Fig. 4-46.

From the explicit comparison of the reconstructed vs truth final fragmentation function ratio, we see that in the simulated jet quenching case, the analysis is indeed not perfect, and the ratio is not perfectly reproduced. Once more the deviations are covered by the estimated systematic uncertainty band. And note once again that we see no sign of centrality dependence to the deviations contrary to what was observed in data.

In summary, these analysis cross checks help to build confidence that we are mea-

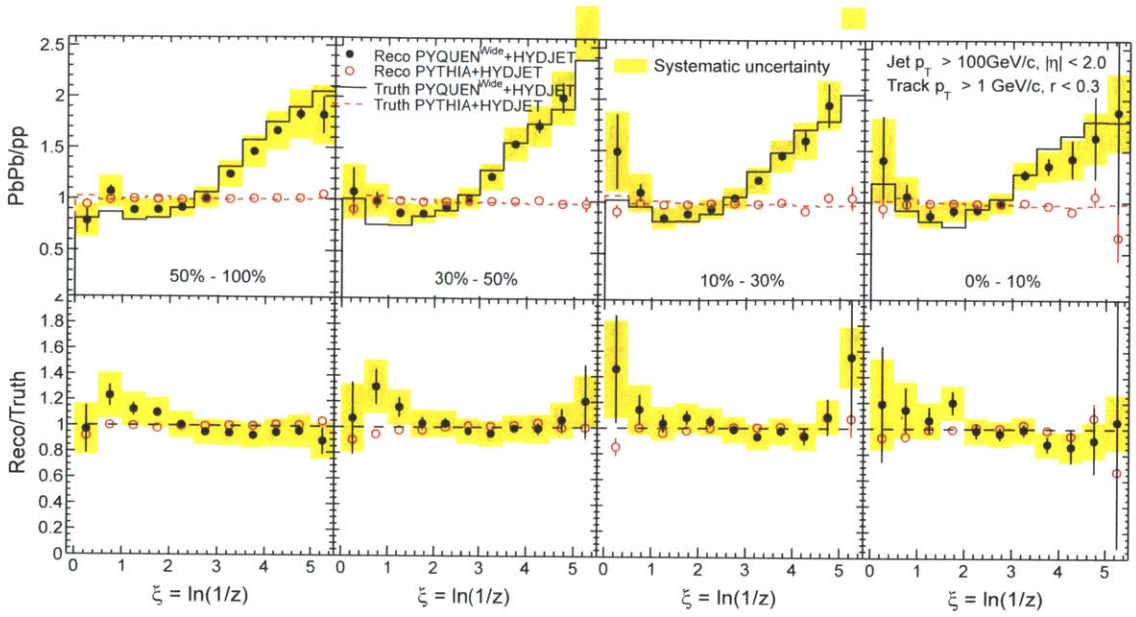


Figure 4-46: Measured fragmentation function of final reconstructed PbPb/pp ratio to the generated truth PbPb/pp ratio for quenched PYQUEN events.

suring the correct physics message in data, that there is indeed centrality dependent fragmentation modification. Also they help us to gain confidence that we are measuring the size of the modification within the estimated systematic uncertainties.

# Chapter 5

# Results and Discussion

In the previous chapter, the full analysis has been presented, the systematic uncertainties were estimated and cross checked. Jet fragmentation function measured in PbPb and pp data will now be presented and discussed. After presenting the data, comparisons to some theoretical models will be discussed.

## 5.1 Jet Fragmentation Function in Vacuum

Jet fragmentation function of charge particles for inclusive jet with $p_{\mathrm{T}} > 100$ GeV/c in pp collisions at $\sqrt{s} = 2.76$ TeV is presented in Fig. 5-1. CMS data is shown as black solid dots. The charged particles were selected with $p_{\mathrm{T}} > 1$ GeV/c and the jets were selected with $0.3 < |\eta| < 2$. The data is plotted as function of the natural logarithm of the jet momentum to the projected particle momentum ratio, $\xi = \ln(1/z)$, as defined in Sec. 4.2. The characteristic hump-back shape of the jet fragmentation function as expected by pQCD (Theory, Sec. 2.2.3) can be seen. Furthermore the approximately gaussian like distribution in the $\xi$ variable as predicted by pQCD (Theory, "MLLA", Sec.2.2.3) is seen in the mid $\xi$ region ($1 \lesssim \xi \lesssim 4$), as shown by the gaussian fit of the CMS data drawn as a black dashed line. The consistency with pQCD predictions shows another verification of pQCD description of parton evolution at the highest energy hadron collider.

Since the jet fragmentation can be seen as a factorized process as the initial hard

scattering, the fragmentation of the same energy jet at different $\sqrt{s}$ hadron collisions should be consistent at leading orders. Also shown in the Fig. 5-1 is jet fragmentation function of charged particles measured at the previous hadron ($p\bar{p}$) collider, Tevatron, at $\sqrt{s} = 1.8$ TeV, by the CDF experiment (2003, [54]).

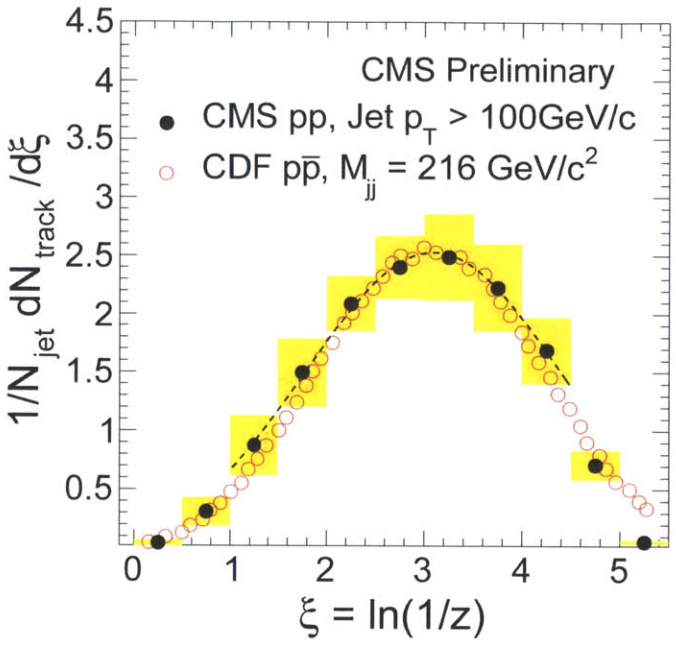


Figure 5-1: Fragmentation function of charged particles measured in CMS $\sqrt{s} = 2.76$ TeV pp data (black solid dot). The distribution is normalized by the number of selected jets, $N_{jet}$. The dash line shows a gaussian fit to the CMS data, as expected by pQCD (Theory, "MLLA", Sec.2.2.3). The yellow band shows the systematic uncertainty band taken from 50-100% PbPb data. Overlaid in red open circles is the CDF $\sqrt{s} = 1.8$ TeV $p\bar{p}$ data [54], after adjusting for difference in jet definition. Note that in CDF analysis the particles were taken from a cone of $\Delta R = 0.28$ around the jet as opposed to a cone of $\Delta R = 0.3$ for CMS. Note also that CDF selected jets in dijet mass, $M_{jj}$, while CMS selected jets with jet $p_{\mathrm{T}}$ threshold.

In order to make the comparison to the CDF data, the jet energy of the CDF data had to be rescaled to account for the fact that CDF were using a jet algorithm with cone radius of 0.7 while the CMS jet algorithm had R parameter of 0.3. Also CDF were correcting the jet energy to the parton level, while CMS corrected to the particle jet level. A rescaling factor of 0.75 was assigned to the CDF data based on the CDF jet shape measurement [55]. Given the jet energy scale uncertainty in CMS

to be a few percent, the scaling factor adjustment is only a rough estimate. We see in Fig. 5-1 that the results between the two experiment compare well, even though the two experiments were at different $\sqrt{s}$ collision energy, used different jet algorithm (CMS used Anti-$k_T$ particle flow jet, while CDF used iterative cone calorimeter jet), had slightly different definition of $z$ (in the CDF paper, $z = p_{\text{track}}/E_{\text{jet}}$), and used different analysis methods. This shows that the jet fragmentation function observable is not sensitively dependent on the mode of jet production or experimental methods of jet reconstruction.

## 5.2 Jet Fragmentation Function in PbPb vs pp

Figure 5-2 shows fragmentation functions reconstructed in pp and PbPb data for tracks with $p_{\mathrm{T}}$ above 1 GeV/c within a radius of 0.3 relative to the corresponding jet axis. For the PbPb fragmentation function, the contribution from the underlying event is subtracted using the $\eta$ reflection method. For the pp reference, the corresponding jet distribution is first smeared with the additional PbPb jet resolution due to the underlying event, and then re-weighted to match the jet distribution in PbPb data.

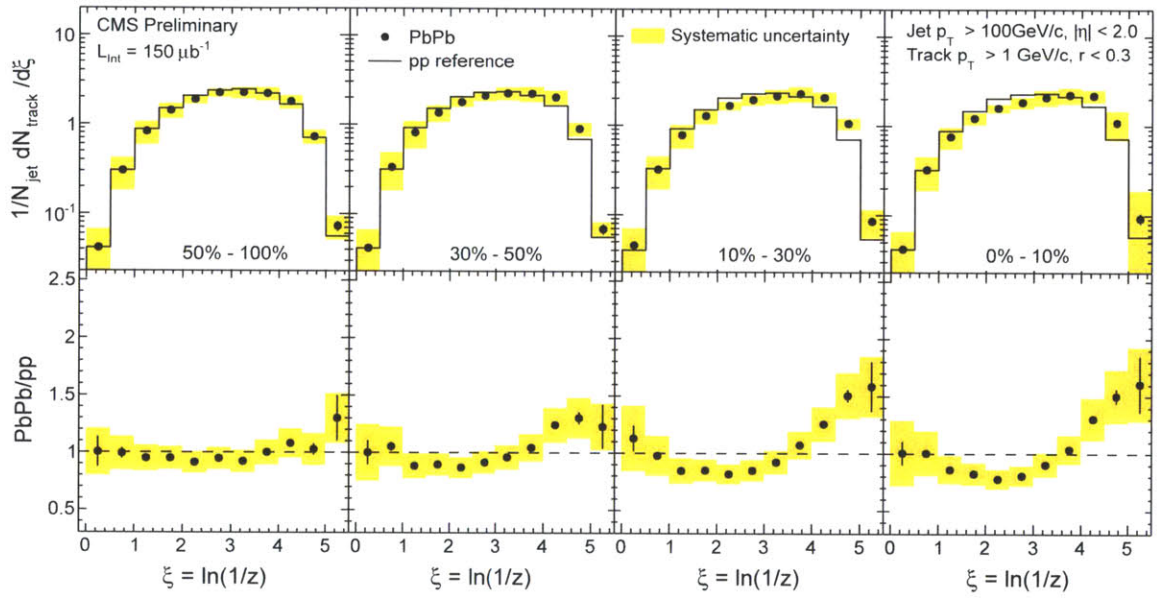


Figure 5-2: Top row shows fragmentation function in PbPb in bins of increasing centrality overlaid with pp. Jets have $p_{\mathrm{T}}$ above 100 GeV/c, and tracks have $p_{\mathrm{T}}$ above 1 GeV/c. The PbPb data is shown in the top row in four increasing centrality bins from left to right. The bottom row shows the ratio of each PbPb fragmentation function to its pp reference. Error bars are statistical, and yellow boxes are the systematic uncertainty.

Figure 5-2 shows that the modification of the fragmentation function of jets in PbPb compared to those in pp increases with the collision centrality. In the 50-100% bin, the ratio of PbPb/pp is approximately flat at unity which means no modification. However, at higher centralities three main regions in $\xi$ can be identified that show

different behavior as a function of centrality. First, at high $\xi$ (corresponding to low $p_{\mathrm{T}}$ particles) region, an excess is observed with increasing centrality. In the most central 0–10% collisions and for the lowest charged particle momenta studied, the PbPb/pp fragmentation function ratio rises to $1.6 \pm 0.2(\mathrm{stat.}) \pm 0.3(\mathrm{syst.})$. This implies that for central collisions the spectrum of particles in a jet has an enhanced contribution of soft particles compared to that from pp collisions. Second, at mid $\xi$ a deficit is observed with increasing centrality. This indicates that energies of the particles from jet fragmentation have been transported to lower $p_{\mathrm{T}}$ as a result of interaction with medium. Third, at low $\xi$ essentially no modification is observed with increasing centrality within the estimated systematic uncertainty. This means the fragmentation pattern is the same at the core and highest $p_{\mathrm{T}}$ regions of the jet fragmentation.

One can further investigate in which track $p_{\mathrm{T}}$ ranges the fragmentation functions exhibit modification by plotting the track $p_{\mathrm{T}}$ spectra in the jet cone.

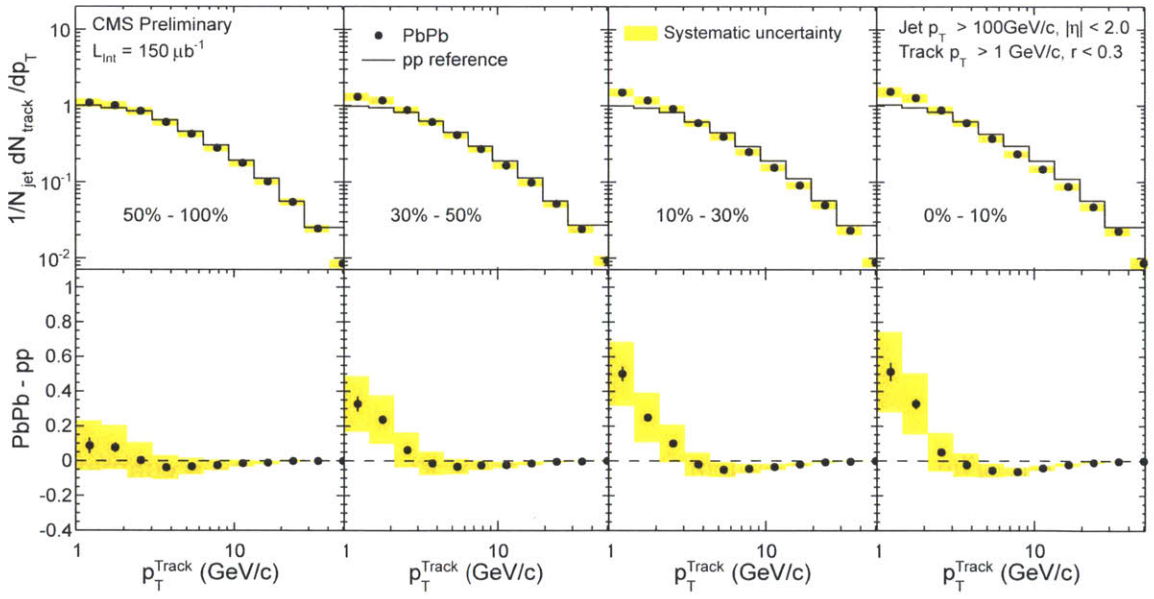


Figure 5-3: The spectrum of tracks inside the jet cone, as a function of track $p_{\mathrm{T}}$, for PbPb and pp. Both the PbPb and pp results are background subtracted, in the same manner as the fragmentation functions. Bottom panel shows the difference of PbPb and pp spectra, which shows that there is an excess of low-$p_{\mathrm{T}}$ tracks in the PbPb events.

Figure 5-3 shows the spectra of tracks in the jet cone. These distributions are ob-

tained with the same background subtraction as described above and are compared to the pp-based reference. The bottom panels show the difference of the two distributions, pp subtracted from PbPb, in order to quantify the excess of tracks at a given $p_{\mathrm{T}}$. The excess that is observed at the high-$\xi$ region of the fragmentation functions is seen to be localized at low-$p_{\mathrm{T}}$ tracks below $\sim 3$ GeV/c in all centralities.

## 5.3 Comparison to Previous Results

To check consistency with the previous published result we overlay the new fragmentation function ratio between PbPb and pp to the published result on the 2010 data [15]. This comparison is shown in Fig. 5-4.

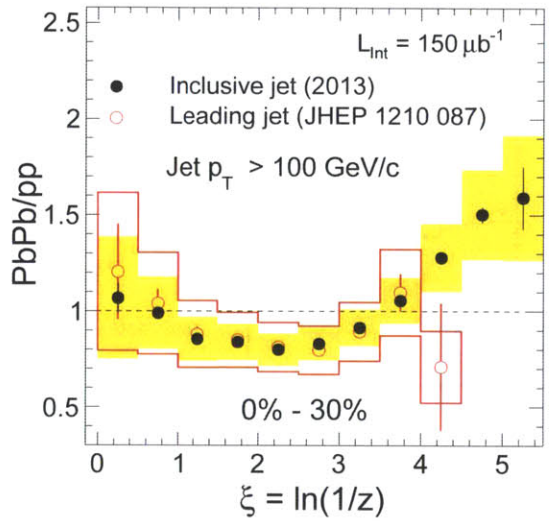


Figure 5-4: The ratio of fragmentation function of PbPb and pp was compared to that measured with 2010 data [15]. The 2010 data is the fragmentation function for leading jets with the di-jet selection of leading jet $p_T > 100$ GeV/c, subleading jet $p_T > 40$ GeV/c, and $\Delta\phi_{1,2} > \frac{2\pi}{3}$.

In the previous measurement, leading and subleading jets were measured separately. Also there was a track $p_{\mathrm{T}}$ cut-off at $p_{\mathrm{T}} > 4$ GeV/c. Nevertheless, an approximate comparison can still be made because for jets with $p_{\mathrm{T}} > 100$ GeV/c, the inclusive jet spectrum is dominated by leading jets due to the steeply falling jet spectrum. The fragmentation function can be compared at higher track $p_{\mathrm{T}}$, lower $\xi$,

where the two analyses overlap. The direct comparison shows that the two results are consistent. The apparent inconsistency of the the physics message between the two measurement can also be understood from the comparison plot. In the 2011 paper [15], the physics message was that the PbPb fragmentation function is consistent within systematic uncertainties with the vacuum jet fragmentation for high $p_{\mathrm{T}}$ tracks. In the new analysis, a centrality dependent modification to the fragmentation function is observed as a result of lowering the minimum track $p_{\mathrm{T}}$ and having a smaller systematic uncertainty.

## 5.4 Comparison to Jet Quenching Models

This section will now compare the measured fragmentation function with the model predictions. Fig. 5-5 shows the PbPb to pp fragmentation ratio for the 0-10% central PbPb collisions from Fig. 5-2.

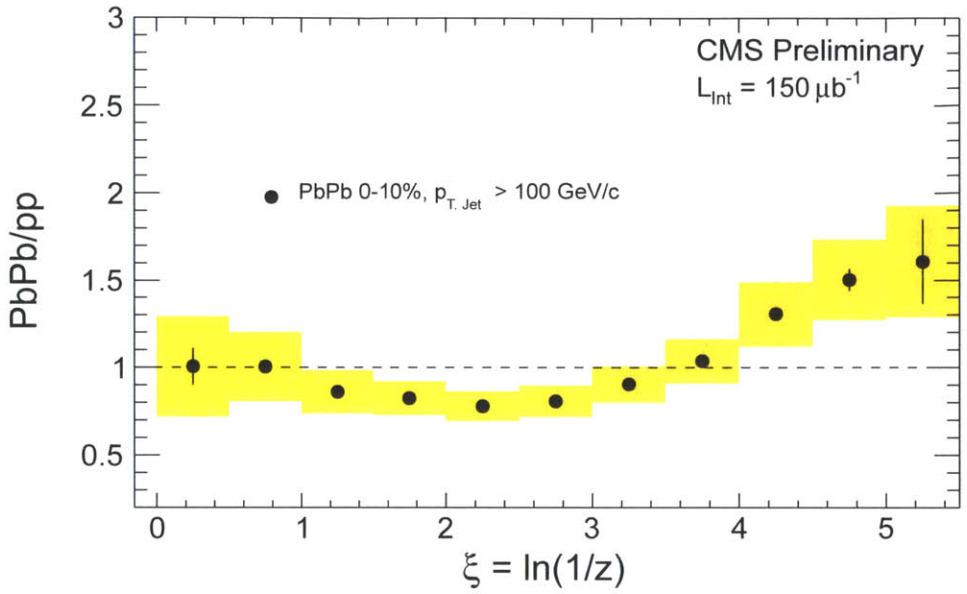


Figure 5-5: The ratio of fragmentation function of PbPb and pp in 0-10% central events.

Recall from Sec. 2.3.3 that the simplest fragmentation modification model is the energy rescaling model. It assumes the partons lose some energy due to medium interactions then fragments outside the medium as if it was in vacuum. We saw that this simple model can well explain the observed factor of five deficit of high $p_{\mathrm{T}}$ tracks at RHIC. In the thesis analysis, the jets are explicitly reconstructed and their fragmentation functions are directly measured. If the energy rescaling model is correct, this would give an unmodified fragmentation (at least at mid to high $p_{\mathrm{T}}$) – since we are comparing the reconstructed fragmentation function to the pp reference with the same jet $p_{\mathrm{T}}$. However we see in Fig. 5-5 that this is not the case. There is clear modification of the fragmentation function in the most central events. At $\xi \lesssim 3$ where the soft particles from the medium no longer contribute, there is a deficit of

tracks in mid $p_{\mathrm{T}}$.

It appears from Fig. 5-5 that the energy rescaling model is wrong. However this is not completely conclusive because there is still one degree of freedom remaining: the jet can be be either a quark jet or a gluon jet. Recall from Eq. 2.4 that the probability for emitting a parton is proportional to the color factors (for quark jets $C_F = 4/3$ and for gluons jets $C_A = 3$). Thus we expect gluon jets to lose more energy in the QCD medium than quark jets. The picture of the energy rescaling model can still be correct given a changed fraction of gluon and quark jets in central events. To answer this question, we can allow the fraction of gluon and quark jets to be a fitting parameter to the measured fragmentation function:

$$\frac{dN}{d\xi} = a\frac{dN}{d\xi}^{gluon} + (1-a)\frac{dN}{d\xi}^{quark}, \tag{5.1}$$

Where $a$ is the fraction of gluon jets that we allow to float in the fit, and $1-a$ is then the fraction of quark jets. To perform the fit, we would need unmodified fragmentation functions separately for gluon jets and quark jets. This can be done (and had been done) in pp data using b-tagged jets, $\gamma$-jet events, or tagged three jet events. For simplicity in this thesis we assume the quark and gluon fragmentation functions from PYTHIA. The result of the component fit is shown in Fig. 5-6 – Fig. 5-9 for different centrality classes.

Note that the fit range is over $0 < \xi < 3$ which corresponds to roughly tracks with $p_{\mathrm{T}} > 5$ GeV/c. We fit only the high $p_{\mathrm{T}}$ part of the fragmentation function because even if the jets fragments as in vacuum, there can still an excess of low $p_{\mathrm{T}}$ particles due to heating up the medium (e.g. in the AdS/CFT correspondence description [56, 57, 58]). When these soft particles fall within the jet cone they manifest themselves as excess at high $\xi$ of the fragmentation function.

In Fig. 5-6, the left is PbPb data peripheral events and right is reconstructed PYTHIA+HYDJET. For the reconstructed MC we see that the superposed gluon and quark fragmentation function fits the total well, as expected. There is approximately little more than 1/3 gluon jets in PYTHIA. In the peripheral PbPb data, we see that

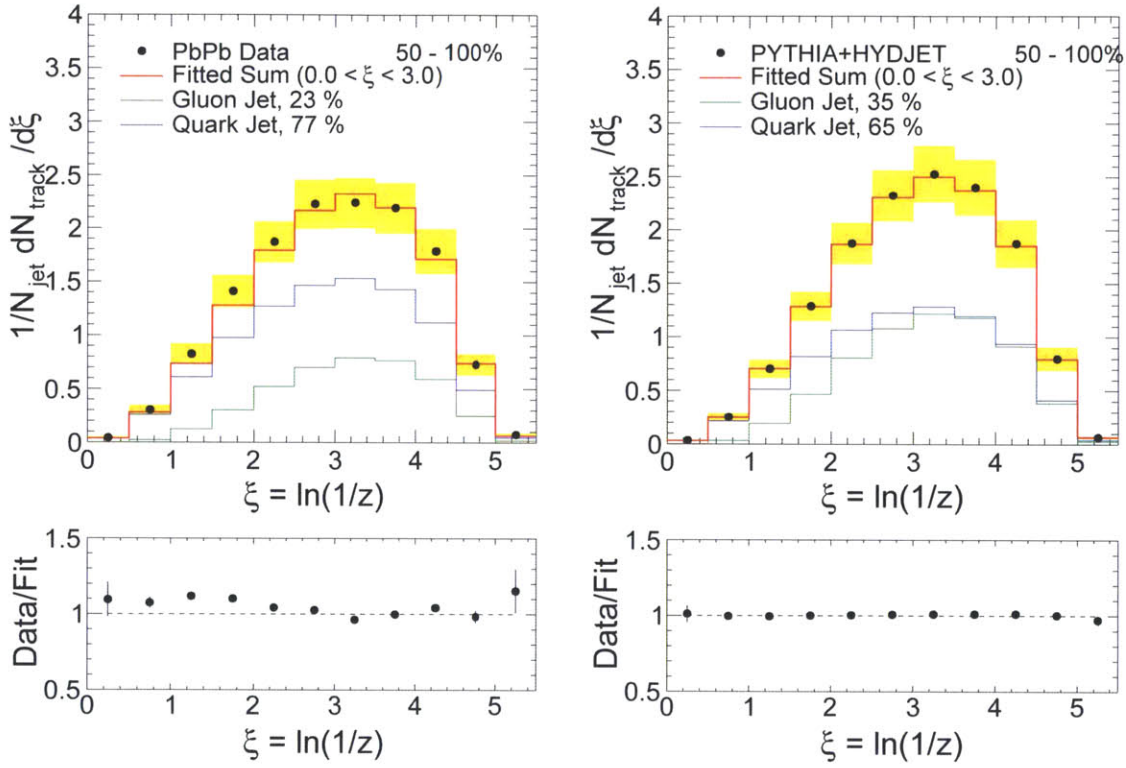


Figure 5-6: The ratio of fragmentation function of PbPb and pp in 50-100% central events overlaid with (MC) gluon + quark jet fragmentation function fits.

the fit does not work perfectly. Now recall from Fig. 5-2 that the peripheral PbPb data is very close to pp jet fragmentation function. Thus in principle we should expect an agreement between the data and the fitted fragmentation function. However the deviation of PYTHIA from pp data is in some sense expected since PYTHIA is only a leading order MC generator, so we expect there will be high order contributions missing. Nevertheless we see that there is agreement within 10% between the peripheral PbPb data and the fitted MC gluon and quark fragmentation function templates. The fit also shows that peripheral PbPb looks more like quark jets than PYTHIA jets. This goes in the right direction of what we expect from jet quenching.

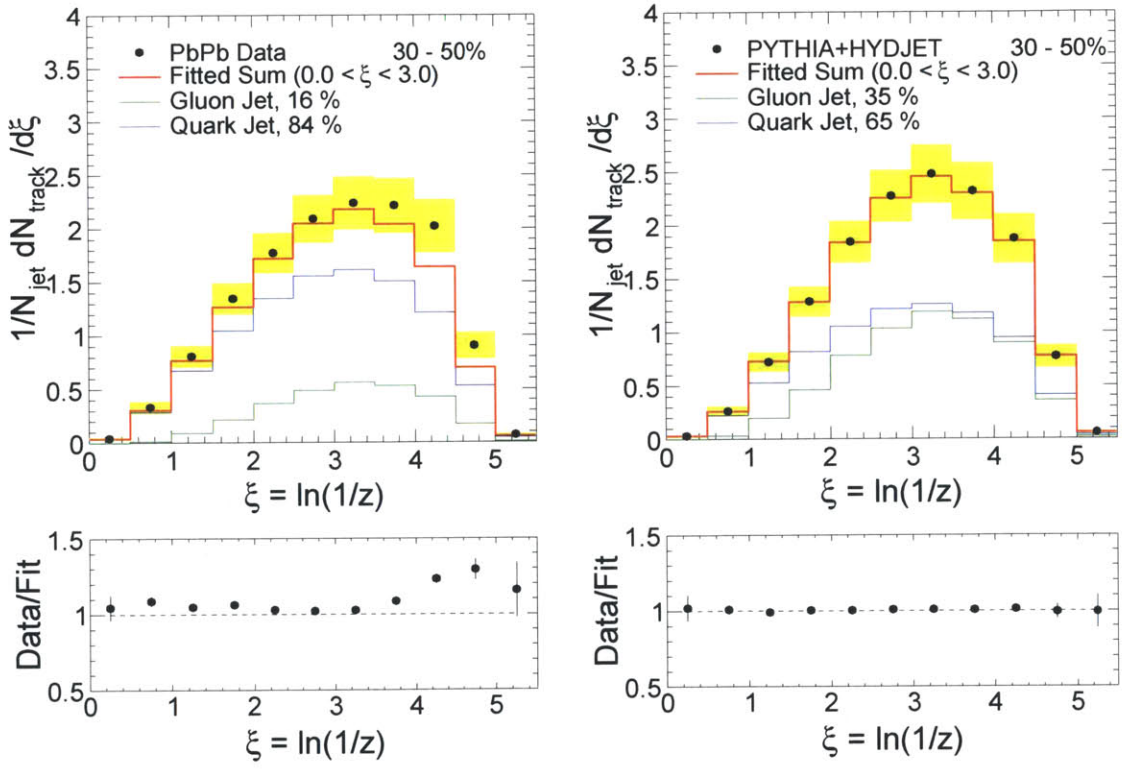


Figure 5-7: The ratio of fragmentation function of PbPb and pp in 30-50% central events overlaid with (MC) gluon + quark jet fragmentation function fits.

The next three figures shows the same gluon and quark fraction fits in PbPb data and MC for increasing higher centralities. Note that in MC the fragmentation function slightly changes going from peripheral to central events. This is due to the reconstruction bias mentioned in Sec. 4.7.2. We expect a bigger bias towards harder

fragmentation functions in the central MC events due to the worsened jet energy resolution. The bias is corrected in the PbPb/pp ratio in the final results, but here we see its effects in the PbPb fragmentation function itself

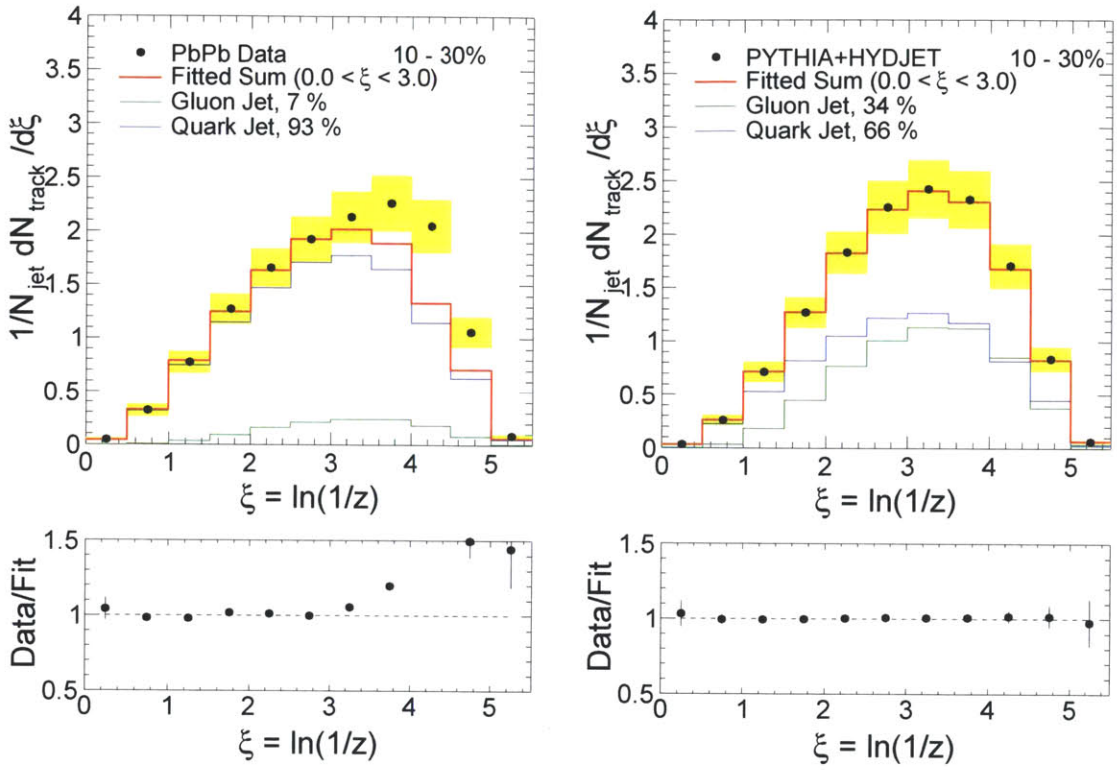


Figure 5-8: The ratio of fragmentation function of PbPb and pp in 10-30% central events overlaid with (MC) gluon + quark jet fragmentation function fits.

Interestingly as go from peripheral to central events in PbPb data the gluon and quark fraction fits gives less and less gluon jet contribution. For the most central events in Fig. 5-9, we see that in fact the data prefers a quark fraction of almost one. The other interesting observation is that the goodness-of-fit actually improves at higher centrality over the range that the fit is performed, $0 < \xi < 3$. It suggests that in the central events the jets are dominated by quark jets and fragments as if in vacuum for mid to high $p_T$ part of the fragmentation function. Note however that this is only a crude study since the quark and gluon templates are taken from Monte Carlo which do not describe the pp data well. Nevertheless it provides evidence that the energy rescaling model is consistent with the reconstructed fragmentation function.

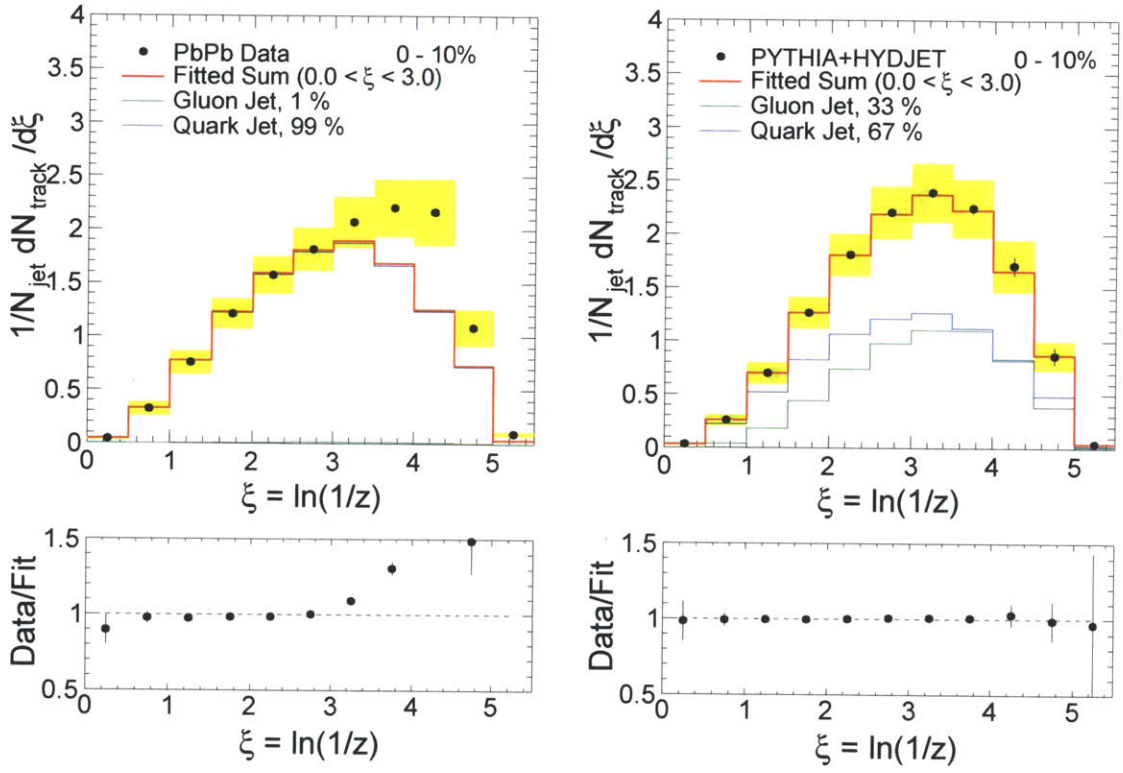


Figure 5-9: The ratio of fragmentation function of PbPb and pp in 0-10% central events overlaid with (MC) gluon + quark jet fragmentation function fits.

We have gained some interesting findings in the hard part of the jet fragmentation function in PbPb data. However there is still more information in the soft part of the fragmentation function where the energy rescaling model cannot explain. To understand the soft part of the fragmentation function, more advanced models are needed that take into account of medium induced modification of the parton evolution as discussed in Sec. 2.3.3. In Fig. 5-10, the fragmentation function ratio is compared to the result from Borghini and Wiedemann [25].

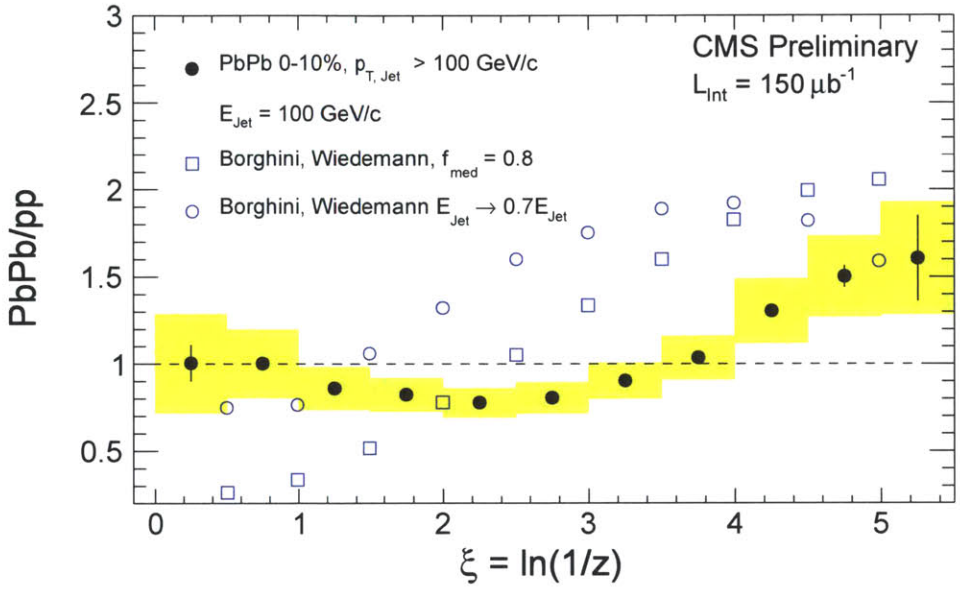


Figure 5-10: The ratio of fragmentation function of PbPb and pp in 0-10% central events compared to model results from Borghini and Wiedemann [25].

We see that in Borghini and Wiedeman's calculation, the effect of the jet energy loss is dramatic both in the low $p_T$ and high $p_T$ region. This is not reflected in data. The large modification at high $p_T$ or low $\xi$ is largely due to the fact that in Fig. 2-17 they were using the original jet energy as the denominator in $z$ instead of the rescaled jet energy due to energy loss. The data on the other can measures the final state jet, which has already this energy loss. Based on the CMS photon jet paper, we know that the amount of energy the jet as lost is at least around 0.7 on average [10]. Thus perhaps a better comparison to the measured data is to first rescale the jet energy by 0.7 in Borghini and Wiedeman's calculation for PbPb and then divide by their pp

reference. This rescaled ratio is shown as blue circles in Fig. 5-10. After rescaling, the modification at low $\xi$ is indeed smaller, however the modification at higher $\xi$ is even more different than data from before the rescale. Apart from the size the effect, the shape of the modification is different in the calculation compared to data.

Fig. 5-11 summarizes the comparisons by overlaying all models with the data at the same time.

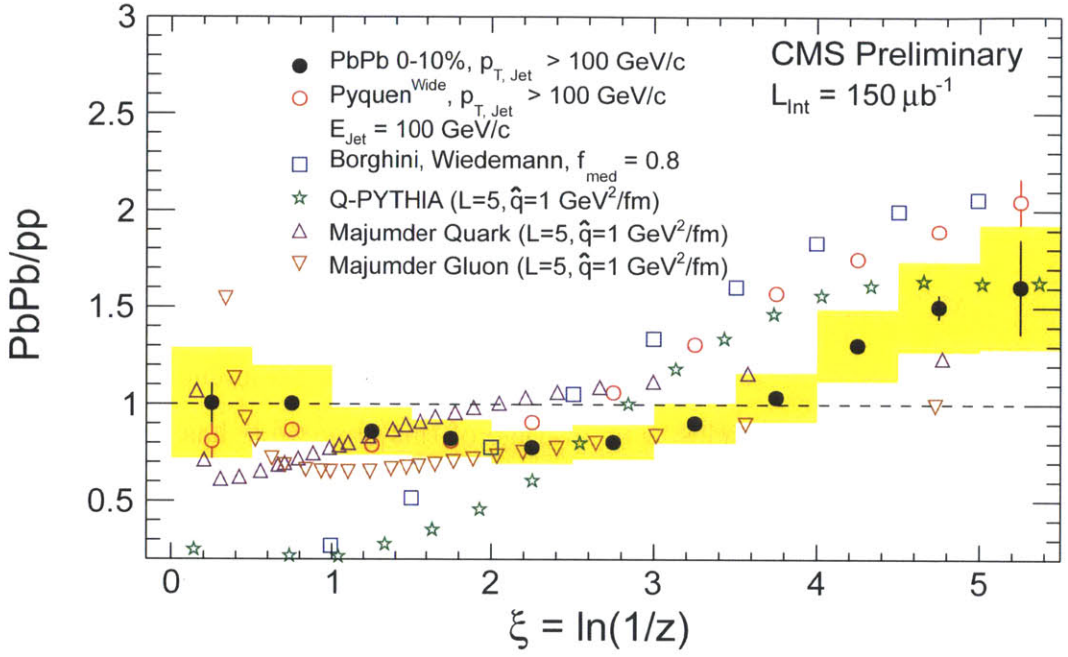


Figure 5-11: The ratio of fragmentation function of PbPb and pp was compared to jet quenching model results.

In conclusion, the best model we found in describing the modified fragmentation function in PbPb data is still the simple energy rescaling model, given a much large quark jet fraction. This is consistent with the picture that the medium induced modification to the fragmentation function is stronger for gluon jets than quark jets, as a result of the larger color factor of gluon jets. Thus the selected jets with $p_{\mathrm{T}} > 100$ GeV/c are dominated by quark jets as a result of the steeply falling jet $p_{\mathrm{T}}$ spectrum. In the energy rescale model, these quark jets then fragments as if in vacuum. The excess of low $p_{\mathrm{T}}$ particles in the jet compared to the pp reference is then a result of soft particle production in the medium related to the parton heating up the colored

QCD medium as the parton traverses through it.

### New Questions Raised and New Frontiers of Research

Based on the result discussed in this thesis, a few new questions are raised.

1. Can we confirm this simple picture of jet quenching, i.e. that the parton loses energy in the medium depending on its color factor then fragments outside of the medium? A few new studies can be proposed.

   (a) Instead of fitting the quark vs gluon jet fraction using the fragmentation function, a better observable may be the track multiplicity of a jet. The track multiplicities for quark and gluon jets are better described by the MC than fragmentation functions.

   (b) Another interesting study is the fraction of the jet momentum carried by the charged particles. The average of this observable has been checked in the cross check analysis, Fig. 4-32. There we saw a decrease of the charged momentum fraction with centrality. This is collaborating evidence of the template fit result that jets in central events are dominated by quark jets. The width of the distribution is also an interesting observable since gluon jets have higher multiplicity and hence smaller relative fluctuation in the charged momentum fraction than quark jets, as discussed in [59].

   (c) Jet shape is another discriminating observable, since we expect a wider jet shape for gluon jets than quark jets.

   (d) Finally a very interesting class of observables are the jet fragmentation function moments [60]. These moments have simple correspondences in QCD calculations, and they carry physical meanings that are different for quark and gluon jets.

2. Direct experimental measurement of quark jet fragmentation function vs gluon jet fragmentation function. Quark jet fragmentation function can be measured from b-tagged jets, or from photon-jet events where the jet on the opposite side

of the photon is dominated by quark jets. Gluon jet fragmentation function can be measured from $b\bar{b}g$ three jet events with b anti-tagging, eg in [61].

3. What does the excess in low momentum particles say about the transport properties of the QCD medium? If the vacuum fragmentation picture is confirmed then the low momentum excess particles that comes from medium dissipative processes can be isolated by subtracting the fragmentation particles from the jet. We can then map out where and in what energy range are these soft medium heat dissipation and hence learn about medium transport properties.

# Chapter 6

# Summary and Conclusion

## 6.1 What have we learned?

In this paper, the fragmentation functions of inclusive jets in PbPb collisions at $\sqrt{s_{NN}} = 2.76$ TeV have been measured. Jets were reconstructed using the anti-$k_T$ algorithm with a resolution parameter of 0.3. The jet reconstruction was based on particle flow objects, which combine information from charged particle tracking and calorimetry.

For the analysis, inclusive jets with $p_{\mathrm{T},jet} > 100\,\mathrm{GeV}/c$ and $0.3 < |\eta_{jet}| < 2$ and charged particles with $p_{\mathrm{T}} > 1$ GeV/$c$ and $|\eta| < 2.4$ were selected. Jet fragmentation functions in a cone of $R = 0.3$ were obtained as a function of collision centrality for four centrality selections, 50-100%, 30-50%, 10-30% and 0-10%. The uncorrelated contribution of the underlying event to the charged particle distribution in the cone was subtracted using an event-by-event "$\eta$-reflected cone" method. Fragmentation function in PbPb collisions were compared to measurements with the same selection in pp collisions at the same collision energy. For this comparison, a jet momentum smearing and reweighting procedure was applied to obtain a proper pp-based reference.

For the 50–100% most peripheral collisions, the fragmentation functions agree in PbPb collisions and the pp reference. For more central collisions, a significant modification of the fragmentation function in PbPb compared to pp in the intermediate

and high $\xi$-region develops. For $\xi$ between 2 and 3, i.e. in the intermediate $p_{\mathrm{T}}$ range of fragmentation products, evidence for a small depletion in the ratio of PbPb to pp is seen, which is accompanied by a rise in the same ratio for $3.5 < \xi < 5.5$, corresponding to charged particles in the region of 1-3 GeV/$c$. In the most central 0–10% collisions and for the lowest charged particle momenta studied, the PbPb/pp fragmentation function ratio rises to $1.6 \pm 0.2(\mathrm{stat.}) \pm 0.3(\mathrm{syst.})$.

Comparing to theory models, the mid to high $p_{\mathrm{T}}$ part of the fragmentation function is best described by a energy rescaling model, assuming the jets in PbPb central events are dominated by quark jets. The mid to high $p_{\mathrm{T}}$ part of the fragmentation function of these jets in the central PbPb events are consistent with fragmentation function of quark jets in vacuum.

## 6.2 Large Picture

By measuring charged particles to low $p_{\mathrm{T}}$, a clear centrality dependent modification of the inclusive jet fragmentation function in PbPb collisions is now revealed.

1. At the very least this is an independent evidence of the creation of the colored QCD medium in PbPb collisions.

2. Evidence for the energy rescaling model implies there may be a simple picture to describe the in-medium modification of jets.

3. The crude gluon vs quark jet fit provides evidence for more gluons jet energy-loss than quark jet energy-loss in PbPb central events. This implies that in-medium energy loss is significant, which in turn provides evidence that the QCD medium is strongly coupled.

The interplay between the modification at high $p_{\mathrm{T}}$ and low $p_{\mathrm{T}}$ part of the fragmentation function gives us interesting constraints on the medium induced energy loss models, and opens up new windows to understand the transport properties of QGP.

# Appendix A

# Bibliography


[1] J. Bjorken, "Energy Loss of Energetic Partons in Quark - Gluon Plasma: Possible Extinction of High p(t) Jets in Hadron - Hadron Collisions," 1982.

[2] J. Adams *et al.*, "Experimental and theoretical challenges in the search for the quark gluon plasma: The STAR collaboration's critical assessment of the evidence from RHIC collisions," *Nucl. Phys. A*, vol. 757, p. 102, 2005.

[3] K. Adcox *et al.*, "Formation of dense partonic matter in relativistic nucleus nucleus collisions at RHIC: Experimental evaluation by the PHENIX collaboration," *Nucl. Phys. A*, vol. 757, p. 184, 2005.

[4] I. Arsene *et al.*, "Quark-gluon plasma and color glass condensate at RHIC? The perspective from the BRAHMS experiment," *Nucl. Phys. A*, vol. 757, p. 1, 2005.

[5] B. B. Back *et al.*, "The PHOBOS perspective on discoveries at RHIC," *Nucl. Phys. A*, vol. 757, p. 28, 2005.

[6] K. Aamodt *et al.*, "Suppression of charged particle production at large transverse momentum in central Pb–Pb collisions at $\sqrt{s_{NN}}$ = 2.76 TeV," *Phys. Lett. B*, vol. 696, p. 30, 2011.

[7] S. Chatrchyan *et al.*, "Study of high-$p_T$ charged particle suppression in PbPb compared to pp collisions at $\sqrt{s_{NN}}$ = 2.76 TeV," *Eur. Phys. J. C*, vol. 72, p. 1945, 2012.

[8] ATLAS Collaboration, "Observation of a Centrality-Dependent Dijet Asymmetry in Lead-Lead Collisions at $\sqrt{s_{NN}}$= 2.76 TeV with the ATLAS Detector at the LHC," *Phys. Rev. Lett.*, vol. 105, p. 252303, 2010.

[9] S. Chatrchyan *et al.*, "Observation and studies of jet quenching in PbPb collisions at $\sqrt{s_{NN}}$=2.76 TeV," *Phys. Rev. C*, vol. 84, p. 024906, 2011.

[10] S. Chatrchyan *et al.*, "Studies of jet quenching using isolated-photon+jet correlations in PbPb and pp collisions at $\sqrt{s_{NN}}$ = 2.76 TeV," 2012.

[11] S. Chatrchyan *et al.*, "Jet momentum dependence of jet quenching in PbPb collisions at $\sqrt{s_{NN}}$=2.76 TeV," 2012.

[12] M. Gyulassy, I. Vitev, X.-N. Wang, and B.-W. Zhang, "Jet quenching and radiative energy loss in dense nuclear matter," 2003.

[13] M. Gyulassy and M. Plumer, "JET QUENCHING IN DENSE MATTER," *Phys.Lett.*, vol. B243, pp. 432–438, 1990.

[14] X.-N. Wang and M. Gyulassy, "Gluon shadowing and jet quenching in relativistic heavy ion collisions," *Nucl.Phys.*, vol. A544, pp. 559–564, 1992.

[15] S. Chatrchyan *et al.*, "Measurement of jet fragmentation into charged particles in *pp* and PbPb collisions at $\sqrt{s_{NN}} = 2.76$ TeV," *JHEP*, vol. 1210, p. 087, 2012.

[16] Y. L. Dokshitzer, "Perturbative qcd for beginners," 1996.

[17] S. Borsanyi, G. Endrodi, Z. Fodor, A. Jakovac, S. D. Katz, *et al.*, "The QCD equation of state with dynamical quarks," *JHEP*, vol. 1011, p. 077, 2010.

[18] P. Kolb, P. Huovinen, U. W. Heinz, and H. Heiselberg, "Elliptic flow at SPS and RHIC: From kinetic transport to hydrodynamics," *Phys.Lett.*, vol. B500, pp. 232–240, 2001.

[19] M. Gyulassy, M. Plmer, M. Thoma, and X. Wang, "High {PT} probes of nuclear collisions," *Nuclear Physics A*, vol. 538, no. 0, pp. 37 – 49, 1992.

[20] M. Gyulassy and X.-n. Wang, "Multiple collisions and induced gluon Bremsstrahlung in QCD," *Nucl.Phys.*, vol. B420, pp. 583–614, 1994.

[21] X.-N. Wang, M. Gyulassy, and M. Plumer, "The LPM effect in QCD and radiative energy loss in a quark gluon plasma," *Phys.Rev.*, vol. D51, pp. 3436–3446, 1995.

[22] F. Arleo, "(Medium-modified) Fragmentation Functions," *Eur.Phys.J.*, vol. C61, pp. 603–627, 2009.

[23] E. Iancu, "QCD in heavy ion collisions," 2012.

[24] U. A. Wiedemann, "Jet Quenching in Heavy Ion Collisions," 2009.

[25] N. Borghini and U. A. Wiedemann, "Distorting the hump-backed plateau of jets with dense QCD matter," 2005.

[26] N. Armesto, L. Cunqueiro, and C. A. Salgado, "Q-PYTHIA: A Medium-modified implementation of final state radiation," *Eur.Phys.J.*, vol. C63, pp. 679–690, 2009.

[27] A. Majumder, "Incorporating Space-Time Within Medium-Modified Jet Event Generators," 2013.

[28] e. a. Khachatryan, "Cms tracking performance results from early lhc operation," *The European Physical Journal C*, vol. 70, no. 4, pp. 1165–1192, 2010.

[29] CMS Collaboration, "Alignment of the CMS silicon tracker during commissioning with cosmic rays," *Journal of Instrumentation*, vol. 5, p. 3009, Mar. 2010.

[30] "The cms experiment at the cern lhc," *JINST*, vol. 3, p. S08004, 2008.

[31] CMS Collaboration, "Identification and filtering of uncharacteristic noise in the CMS hadron calorimeter," *Journal of Instrumentation*, vol. 5, p. 3014, Mar. 2010.

[32] CMS Collaboration, "Centrality dependence of dijet energy balance distributions in pbpb collisions at 2.76 tev," CMS Analysis Note CMS-AN-10-399, CMS, 2011.

[33] CMS Collaboration, "Transverse-momentum and pseudorapidity distributions of charged hadrons in pp collisions at $\sqrt{s} = 7$ TeV," *Phys. Rev. Lett.*, vol. 105, p. 022002, 2010.

[34] M. L. Miller, K. Reygers, S. J. Sanders, and P. Steinberg, "Glauber modeling in high energy nuclear collisions," *Ann. Rev. Nucl. Part. Sci.*, vol. 57, p. 205, 2007.

[35] T. Sjöstrand, S. Mrenna, and P. Skands, "PYTHIA 6.4 Physics and Manual," *JHEP*, vol. 05, p. 026, 2006.

[36] S. Agostinelli *et al.*, "Geant 4 – a simulation toolkit," *Nucl. Inst. Meth.*, vol. A506, p. 250, 2003.

[37] I. P. Lokhtin and A. M. Snigirev, "A model of jet quenching in ultrarelativistic heavy ion collisions and high-$p_T$ hadron spectra at RHIC," *Eur. Phys. J. C*, vol. 45, p. 211, 2006.

[38] CMS Collaboration, "Particle–flow event reconstruction in CMS and performance for jets, taus, and $E_{\mathrm{T}}^{\mathrm{miss}}$," CMS Physics Analysis Summary CMS-PAS-PFT-09-001, 2009.

[39] G. P. Salam, "Towards Jetography," *Eur.Phys.J.*, vol. C67, pp. 637–686, 2010.

[40] D. Y. Grigoriev, E. Jankowski, and F. Tkachov, "Towards a standard jet definition," *Phys.Rev.Lett.*, vol. 91, p. 061801, 2003.

[41] M. Cacciari, G. Salam, and G. Soyez, "The anti-$k_t$ jet clustering algorithm," *JHEP*, vol. 04, p. 063, 2008.

[42] M. Cacciari, G. P. Salam, and G. Soyez, "Fastjet user manual." 2011.

[43] M. Nguyen, "Jet Reconstruction with Particle Flow in Heavy-Ion Collisions with CMS," *J.Phys.G*, vol. G38, p. 124151, 2011.

[44] S. Chatrchyan *et al.*, "Observation and studies of jet quenching in PbPb collisions at nucleon-nucleon center-of-mass energy = 2.76 TeV," *Phys. Rev. C*, vol. 84, p. 024906, 2011.

[45] O. Kodolova, I. Vardanian, A. Nikitenko, and A. Oulianov, "The performance of the jet identification and reconstruction in heavy ions collisions with CMS detector," *Eur. Phys. J. C*, vol. 50, p. 117, 2007.

[46] "Plans for jet energy corrections at cms," *CMS Physics Analysis Summary*, vol. PAS JME-07-002, 2007.

[47] "Measurement of the relative jet energy scale in cms with pp collisions at sqrt(s) = 7 tev," *CMS Analysis Note*, vol. AN2010-139, 2010.

[48] CMS Collaboration, "Determination of jet energy calibration and transverse momentum resolution in cms," *JINST*, vol. 6, p. P11002, 2011.

[49] "Heavy ion tracking," *HeavyIonTracking*, 2010.

[50] "Minimum bias tracking," *MBTracking*, 2010.

[51] "Tracking and vertexing results from first collisions," *CMS Physics Analysis Summary*, vol. CMS-PAS-TRK-10-001, 2010.

[52] F. Abe *et al.*, "Jet-fragmentation properties in $p\bar{p}$ collisions at $\sqrt{s} = 1.8$ tev," *Phys. Rev. Lett.*, vol. 65, p. 968, 1990.

[53] S. Chatrchyan *et al.*, "Azimuthal anisotropy of charged particles at high transverse momenta in PbPb collisions at $\sqrt{s_{NN}} = 2.76$ TeV," *Phys.Rev.Lett.*, vol. 109, p. 022301, 2012.

[54] D. A. et al., "Momentum distribution of charged particles in jets in dijet events in $p\bar{p}$ collisions at $\sqrt{s} = 1.8$TeV and comparisons to perturbative qcd predictions," *Phys. Rev. D*, vol. 68, p. 012003, Jul 2003.

[55] D. Acosta *et al.*, "Study of jet shapes in inclusive jet production in $p\bar{p}$ collisions at $\sqrt{s} = 1.96$ TeV," *Phys.Rev.*, vol. D71, p. 112002, 2005.

[56] E. Iancu, "Partons and jets in a strongly-coupled plasma from AdS/CFT," *Acta Phys.Polon.*, vol. B39, pp. 3213–3280, 2008.

[57] S. S. Gubser and A. Karch, "From gauge-string duality to strong interactions: A Pedestrian's Guide," *Ann.Rev.Nucl.Part.Sci.*, vol. 59, pp. 145–168, 2009.

[58] J. Casalderrey-Solana, H. Liu, D. Mateos, K. Rajagopal, and U. A. Wiedemann, "Gauge/String Duality, Hot QCD and Heavy Ion Collisions," 2011.

[59] H.-M. Chang, M. Procura, J. Thaler, and W. J. Waalewijn, "Calculating Track-Based Observables for the LHC," 2013.

[60] M. Cacciari, P. Quiroga-Arias, G. P. Salam, and G. Soyez, "Jet Fragmentation Function Moments in Heavy Ion Collisions," *Eur.Phys.J.*, vol. C73, p. 2319, 2013.

[61] T. A. Collaboration, "Quark and gluon jet properties in symmetric three-jet events," *Phys. Lett. B*, vol. 384, pp. 353–364. 13 p, Dec 1995.